Kathmandu University

School of Engineering

Department of Mechanical Engineering

DISSERTATION ON

DEVELOPMENT OF SEDIMENT FRIENDLY CROSSFLOW HYDRO TURBINE.

In Partial Fulfillment of the Requirements for the

Doctorate Degree in Mechanical Engineering

Oblique Shrestha

December 2021

SUMMARY

Micro-hydropower plants (MHP) provides the best solution to the power needs of rural and small communities which serve as a decentralized power source to meet the local population requirement. Energy requirements for lighting, cooking, heating, drying, agro-processing and other small scale industrial activities can be met through these MHPs most reliably in the rural areas of the country like Nepal. Crossflow turbines are used widely in such MHPs due to their simple design, easier maintenance, low initial investment and modest efficiency. Also, because of their suitability under the low head, their efficient operation under a wide range of flow variations and ease of fabrication, crossflow turbines (CFT) have been extensively employed.

In the context of Nepal, MHP alone has effectively generated about 28,000 kW of electricity with a total of 2900 Microhydro powerplants of different sizes and capacities by mid of July 2012. Thus, supplying electricity to well above 350,000 households in remote areas of Nepal. However, there is not much traceable knowledge about CFT design, and Nepalese manufacturers follow the design of foreign institutions. In addition, due to a lack of knowledge of material technology, the use of materials is limited to mild steel for the production of critical components such as runners and guide vanes. In addition, the design of most researchers worldwide focus only on optimizing turbine efficiency and does not take into account the impact of sediment erosion on the CFT, which is a local operational problem. As a result, erosion can occur on the runner and guide vane and thereby reduce service life and efficiency.

This research work intends to focus on developing sediment resistive CFT. It includes design, numerical simulation and testing of the turbine to address the local sediment problem. The simulation works consist of locating erosion on turbine blades, modifying the blade profiles and efficiency measurement of modified CFT.

Numerical analysis has been performed in a full CFT turbine through a computational fluid dynamics (CFD) Analysis simulation tool ANSYS CFX. Five different blade angles at various guide vane openings have been studied in an attempt to reduce the effect of sediment on the blades of a runner without compromising the efficiency of the

turbine. Sediment erosion rate density, as well as efficiency hill diagram for the runner, are considered for each design to determine the best-optimized design. A lower inlet blade angle significantly reduces the effect of sediment and also improve the efficiency of the turbine.

Two types of erosion testers are designed and developed to observe the effect of sediment on blade specimens and the efficiency of the optimized turbine. At the initial stage of this research work, rotating disc apparatus (RDA) was manufactured and experiments were done to investigate the wear pattern and estimate the erosion resistive behavior through the weight loss method on different materials with and without coating tungsten carbide. The high erosion resistance of the material is found to be the dependence of erosion rate on the hardness value, ductility, and tensile stress. The tungsten carbide coatings on the different materials have enhanced the erosion resistance properties.

Another erosion tester, Non- Re-circulating (NRC) type was developed and the experiment was conducted in a closed loop at Turbine Testing Laboratory, Kathmandu University. This setup is one of its kind for its ability to conduct sediment erosion tests on model turbines by simulating the operating conditions that exist in actual micro hydropower plants. CFT with 30 blades and an inlet blade angle of 16^0 was selected to perform the tests. The four sections of the Optimized model runner with detachable blades was 3D printed with the provision of four slots for blades insertion. The sediment was injected into the tester to observe wear patterns and amount of weight loss in the test specimens. Test specimens were dried thoroughly to remove the water to avoid chances of error in weight measurement. For the performance measurement, calibrated instruments Electro-magnetic flow meter, pressure transducer and pressure transmitter are used to measure the flow, torque and pressure respectively. The turbine is coupled with an induction motor through a torque transducer, which is driven by a VFD to stabilize the RPM of the rig and dumping of generated power. Data logging is carried out using LabVIEW software.

Wear pattern and performance curves of the optimized runner at different RPM are obtained and compared with the CFD results. The regions with maximum efficiency

obtained through CFD is very similar to the results obtained from the experimental analysis. The locations of the erosion from the experiment results are similar when compared with the CFD simulation results and with the eroded runner of Daram Khola Micro Hydro Project which was operated where water is loaded with sediment.

Five different runner designs, with different inlet blade angles, were analyzed numerically. For each design, nine numbers of guide opening from the full opening are named 0^0, 2^0, 4^0, 5^0, 6^0, 8^0, 10^0, 12^0 and 14^0. Sediment erosion rate density, together with the effective hill plots for the runners are graphed to determine the best design. In the first stage, all five designs have a similar velocity distribution at the same flow rate and rotational speed. In the second stage, however, among all the designs, the velocity for the 16^0 inlet blade angle is way less than all other designs. Further, it is observed that the velocity for all the designs is higher on the suction side of the blade in the second stage. After the close study of the velocity distribution of all the designs, a design with an inlet blade angle of 16^0 is found to be the best design that will have less sediment erosion. Moreover, it is observed that among these designs efficiency for the 16^0 is higher which may be due to a better stagnation angle in the first stage. Therefore, an inlet blade angle of 16^0 is the best design with higher efficiency and low sediment erosion.

BIOGRAPHICAL SKETCH

The author of this thesis, Oblique Shrestha is a PhD candidate at the Department of Mechanical Engineering, a researcher, a professional in the Hydro Power sector and a 'Nepal Bidya Bhusan Kha' awardee. He has over 14 years of extensive experience in the field of Hydro and Electro-Mechanical components. He led numerous Mechanical works of Hydro Power Projects and is competent in the design, procurement, fabrication, installation and commissioning of Hydro and Electro-Mechanical components. He currently serves as a Research Fellow at Turbine Testing Lab (TTL) and is involved in several projects undertaken by TTL. He has a special interest to design and developing the IEC standard test rigs at KU-TTL for performance and sediment erosion testing of hydro turbines. He has attained knowledge of laboratory and field testing of various types of water-driven turbines which incorporates Francis, Pelton, Cross Flow and Turgo Turbine.

His current research is based on the design and analysis of micro class Crossflow turbines to better handle sediment-laden water.

ACKNOWLEDGEMENTS

This research work has been performed at Turbine Testing Lab (TTL), Department of Mechanical Engineering, KU. Part of this work was carried out at PIVLAB, Korea Maritime & Ocean University(KMOU)

This thesis has been carried out under the direct supervision of Prof. Dr Bhola Thapa. Prof. Dr Young-Ho Lee and Prof. Dr Hari Prasad Neopane. I am extremely grateful for their constructive advice, suggestions, valuable time and support throughout this work. The enthusiasm and patience shown for this research from my supervisors have guided me to accomplish the objective of this research work is greatly commendable and is very much appreciated.

Colleagues, students and staff of Turbine Testing Laboratory and PIVLAB have contributed a lot to bring my research to this productive stage. Discussion and interaction have been very fruitful. I am thankful to Assistant Professor Dr Biraj Singh Thapa, Former Faculty Incharge of Turbine Testing Lab for initiating and providing the computer with the computational capability to perform the simulation work. I want to share the acknowledgement to Aman Kapali and Dr Sailesh Chitrakar for continuous encouragement, assistance in the design, fabrication & installation of the test rig, logistic support to perform the experiment and critically reviewing the monograph. The discussion and exhortation with Atamaram Kayastha related to ICEM CFD meshing and post-processing deserve a very special mention. I am much obliged to Mr Dadiram Dahal, Mr Amul Ghimire, Mr Prajwol Sapkota, Mr Nischal Pokharel and Mr Saroj Gautam for the thought-provoking discussions, intelligent comments and inspiration. My sincere thanks go to Mr Ram Lama for speedily making sand available at TTL premises and providing manpower to sieve the sand of the required size. I am grateful to Mr Bhuwan Bhattarai for his technical assistance in the installation and operation of the erosion tester within the TTL premises.

I am extremely thankful to Korea Institute of Energy Technology Evaluation & Planning (KETEP), Republic of Korea and University Grant Commission (UGC), Nepal for the fund to pursue and conclude this research work.

I wish to express my sincere gratitude to KU staff members for their kind co-operation and encouragement for the successful completion of this work.

I would like to thank my parents, not only for the moral support and continual motivation but supporting me financially in a tough time. In addition, I would like to thank My father Shiva Shanker Shrestha for his valuable guidance in the design phase of both the test rigs and fabrication of components of the turbine. I wish to thank my wife, Punam Shrestha who has stood by me through all my struggles, my absences, my temper and impatience. She supported the family during much of my doctorate studies in my absence. Along with her, I want to acknowledge my son, Sulek Shrestha for jogging my memory and inspiring me for the completion of the work.

Dedicated to my beloved family.

TABLE OF CONTENT

LIST OF FIGURES

LIST OF TABLES

LIST OF ABBREVIATIONS

ARB	Anti-recirculation block
3D	Three Dimensions
BYS	Balaju Yantra Shala P Ltd.
CAD	computer-aided design
CFD	Computational fluid dynamics
CFT	Cross Flow Turbine
CPU	Central processing unit
DNS	Direct Numerical Simulation
ERT	CFT erosion test rig
GCI	General Grid Interface
HPP	Hydro Power Plant
HVOF	High Velocity Oxy Fuel
ID	Internal Deflectors
IEC	International Electro technical Commission
KETEP	Korea Institute of Energy Technology Evaluation and Planning
KMOU	Korea Maritime and Ocean University
KU	Kathmandu University
kW	Kilo Watts
LabVIEW	Laboratory Virtual Instrument Engineering Workbench
LES	Large Eddies Simulations
MH	Micro Hydro
MHPs	Micro hydro plants
MIT	mesh independence tests
MW	Mega Watts
NMHDA	Nepal Micro Hydropower Development Association
NRC	Non- Re-circulating
N-S	Navier-Stokes
NTNU	Norwegian University of Science and Technology
PPM	Parts per Million

PSD	Particle Size Distribution
RC	Re-circulating
RDA	Rotating Disc Apparatus
RNS	Reynolds Averaged Navier-Stokes
RPM	Revolutions per Minute
RSS	Residual Sum of Squares
SEE	Sum of squared errors
SERD	Sediment erosion rate density hill
SST	Shear Stress Transport
TTL	Turbine Testing Laboratory
UGC	University Grants Commission
VFD	Variable Frequency Drive
WC	Tungsten Carbide coating

LIST OF SYMBOLS

Symbol	Description	Unit
g	Acceleration due to gravity	[m/s^2]
β	Angle between tangent of the blade and runner	[o]
ω	Angular velocity	[rad/s]
e_i	Cumulative erosion	[mg/gm]
ρ	Density of liquid	[m^3/kg]
η	Efficiency	[%]
Q	Flow rate	[l/s]
H	Head	[m]
P	Power	[W]
P_m	Power of motor	[hp]
H	Pressure head	[m]
R	Radius of any point from axis of rotation	[m]
N	Rotational speed	[rpm]
ρ	Specific water density	[kg/m3]
Ø	Speed ratio	[-]
τ	Torque	[Nm]
α	Angle of atack	[o]
θ_s	Admission angle	[o]
N_b	number of blades	[o]

CHAPTER 1:INTRODUCTION

The sediment erosion problem in Nepal is inevitable which causes major operational as well as maintenance challenges in lots of hydropower whether it's a micro, small or large hydropower. That's the reason lots of research are inclined to minimize the effect of sediment erosion problem by applying different approaches which can be categorized into three different ways: a) control sediment from entering the turbine (settling the sediment at desanding basin), b) surface coating of the turbine components which comes in contact with water and c) change in design by varying different parameters. This thesis studies the dynamics of fluid flow through crossflow along with sediment particles by using different designs and coming up with a new design that has less sediment erosion effect.

1.1. Background

In pursuit of renewable energy sources, many developing countries are relying on micro hydro systems as it is simple to construct and can be achieved with limited tools, techniques and resources. Due to such benefits, micro hydro systems are popular in Nepal, where small streams of water are almost available in each and every nook and corner of the country. Among the different types of hydro turbines, Crossflow turbine (CFT) has been extensively used in the field of micro hydro because of its characteristic feature of operating at low head under a wide range of flow.

A Crossflow turbine is normally considered as an impulse turbine with two major parts, the runner and the rectangular-shaped nozzle having its width equal to the length of the blade in the runner. The runner consists of several blades fitted in circular pattern in between two rotating discs. The shape of the blade is curved and it is a certain portion of a circular pipe with a required diameter. A Crossflow turbine is uniquely differentiated from other turbines as it produces power in two stages which is its characteristic feature. That is, the nozzle flow entering the runner makes an impact at two stages in the turbine. The first stage is the outer part of the runner close to the rectangular nozzle where the flow enters the outer periphery and is directed toward the

center of the runner. Then the flow enters the hollow region of the turbine and makes an impact in the second stage. From the second stage, the flow is again directed towards the periphery of the runner and exits the runner. Thus, the total power generated from the turbine is divided into these two stages.

Generally, these Micro hydro plants (MHPs) operate in isolated mode distributing the electricity in the local rural communities where the population is very minor and thinly scattered. Without any doubt, the rural population in Nepal relies on Mini/Micro/pico-Hydro Plant for electricity. Such plants have been installed up to 41,883 kW until 2014 [1]. Micro Hydro power plants alone have successfully generated approximately 28,000 kW of electricity establishing 2900 MH plants of different sizes and capacities by mid of July 2012 [2] [3]. Thus supplying electricity to well above 350,000 households in remote areas of Nepal [2] [3].

1.2. Motivation for the Study

The private sector owned Micro hydro (MH) manufacturing companies of Nepal has been providing its product and services inside and outside the country that has matured technical competence as well as substantially over the past 40 years [3]. In this period, several kinds of research and designs works successfully developed Cross flow turbines (CFT) from the T-1 model to the most advance and reliable T-15 model [4]. Subsequentially, these manufacturers developed capacity and competence in almost all the sectors of development of crossflow turbine-based micro hydro from feasibility study, survey, design, manufacturing, installation, commissioning, repair and maintenance required. However, in recent years' micro hydro systems are either replaced by national grid systems or become obsolete due to lack of maintenance as well as proper supervision. This decline in popularity of the micro hydro system, although these systems are simple and do not need a dam or other superstructures that may have an ecological impact, may be due to the improper study and development of the turbines that are used in micro hydro like crossflow. A survey conducted by the Nepal Micro Hydropower Development Association (NMHDA) and other official bodies of the Nepal Government reveal the turbines harshly affected by sediment erosion require

intensive research and development of these turbines in regard to sediment erosion minimizations.

The main reason for the constant breakdown of turbines in Nepalese hydropower is that the effect of sand particles was not considered in the design of either micro or large hydro turbines. Obviously, a lack of knowledge on sediment erosion will eventually hit the power output of turbines as the hydraulics of the turbine is affected after turbine components are eroded badly by a higher concentration of sand particles.

Due to the lack of proper study, adequate data regarding the sediment erosion effect on CFT is hard to find. However, there are numerous cases of failure of CFT runners due to the sediment erosion effect. For instance, Daran Khola MHP is one of the severely affect micro hydro with the CFT. In this project, two turbines are mechanically synchronized to the single generator with a gross head of 13 meters, flow 550 l/s.

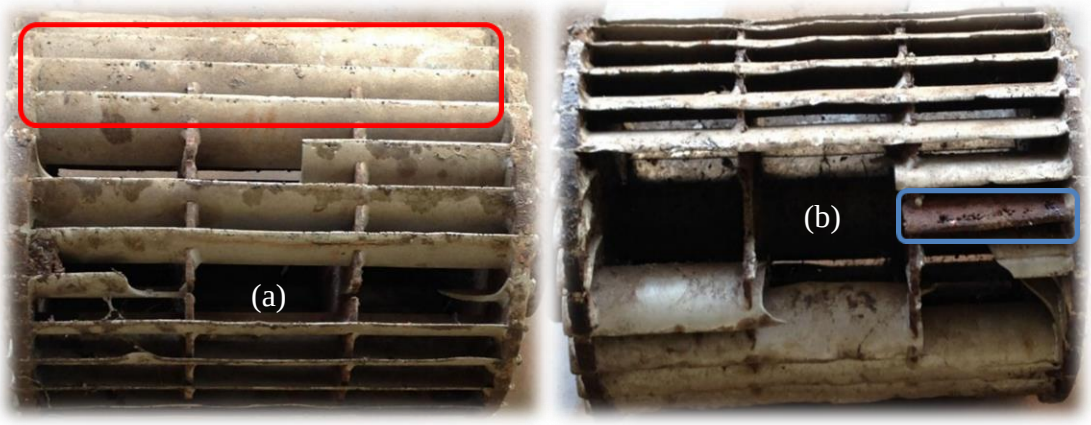

Figure 1-1: Damaged CFT (a) runner 1 and (b) runner 2 of Daran Khola MHP due to sediment erosion

It is observed from Figure 1-1, pitting erosion at the outlet section especially the suction side of the blade is severe which eventually breakdown the turbines making it hard to operate at an acceptable efficiency. This is the case of most of the micro hydro with CFT installed all over Nepal which either forced to shut down the powerhouse or replacement of the complete turbine. In both the case lots of remote villages relying on the power supply from such micro hydro are deprived of electricity for months.

Moreover, it is also found that turbines manufactured in Nepal do not adopt actual flow behaviour, but are based on empirical relationships and past experience. Thus, more rigorous research is needed to address these problems which have motivated the author to work towards the design and development works of sediment friendly CFT.

Nevertheless, attempts have been made with the start of research within the country so as to address the problem of sediment erosion and obtain a design that has negligible erosion. Shrestha et al [5] studied the effect of sediment on cross-flow turbines through simulation using ANSYS CFX. In his studies, a series of simulations were conducted in order to compare the sediment erosion in the turbine operating at a low head regime of 15 m head with the rotational speed of 529 rpm at various guide vane opening ranging from 20 % to 100 % by changing the opening by 20 % considering several characteristics of sediment such as size, shape, type, hardness, concentration. During the study, significant erosion on turbine components was noted, which urges that sediment erosion in CFT is also crucial which is mostly affected by turbine flow condition and sediment size. Looking at these conditions, it is clear that not much work has been done towards a modification of the design of CFT taking sediment erosion as one of the parameters during the design phase. For ensuring the sustainable development of not only micro hydro but also the whole hydropower sector within Nepal, further research and development, primarily towards the solution of sediment problem and technical improvement is very essential. This thesis seeks to contribute towards the design of sediment friendly CFT without compromising efficiency.

1.3. Research Questions

The main goal of this study is to come up with a design of CFT which have minimum sediment erosion effects without a significant decrease in efficiency. The erosion on CFT is assumed to be affected by concentration and shape of sediment, inlet blade angle and angle of admission.

For a sediment resistant CFT with high efficiency, this research seeks the answer to the following research questions:

a) How do different inlet blade angles affect both the erosion behaviour and efficiency at a different rotational speed of the runner and flow conditions?

Hypothesis: Change in inlet blade angle affects the erosion severity, as it does in other types (Francis) of the turbines.

b) What are the key dynamics characters that set the performance of the runner operating at sediment laden water?

Hypothesis: Performance of the runner is affected by sediment, flow and geometrical parameters in the case of CFT, the extent of which needs to be investigated.

c) Is it possible to conduct sediment erosion testing at a laboratory with a CFT runner?

Hypothesis: Sediment erosion can be tested in laboratory conditions by using a Non-Recirculating type of rig so that the results match with actual conditions.

1.4. Objective

The objectives of this study are

1 To minimize sediment erosion in CFT without affecting the efficiency of the turbine by changing the blade design
2 To develop a Non-Recirculating (NRC) sediment erosion rig for testing CFT blades
3 To correlate erosion in CFT with affecting parameters using the NRC sediment erosion rig

1.5. Methodology

This research is based on both numerical and experimental works. It can be divided broadly into three sections: Rotating Disc Apparatus (Numerical and experimental analysis), Numerical Studies on KMOU design and Experimental works to validate it. In the first part of this study, a close study of the previous research and development on RDA was carried out in order to develop an RDA for conduction experiment regarding the sediment erosion on the crossflow blade of different designs. A robust RDA was

designed and a series of experiments on T-15 blades using RDA was performed at KU and with optimized T-15 CFT blades at KMOU to investigate the sediment erosion effect. The KMOU design was optimized and the experiment was conducted on five different test cases with different materials and tungsten carbide coating. So, the same design is adopted for numerical studies in this research work. However, the KMOU design had not studied the effect of beta angle distribution on sediment effect behaviour which is a vital parameter for the design of sediment friendly CFT.

Hence, the optimized design proposed by KMOU was adopted for this research. The second part of this study focuses on numerical studies in order to look at the sediment effect on KMOU design by varying the β-angle distribution. It has been seen how β-angle distribution makes an impact on sediment erosion behaviour on Francis turbine. So, a hypothesis was made that by changing the β-angle distribution of crossflow blades, the sediment erosion effect can be minimized without significant loss in efficiency. Five different cases of different β-angle distribution were formulated and a numerical study was carried out. The next challenge was to validate the numerical results experimentally which is made possible by developing a sediment erosion test rig where full turbine at design condition can be tested.

Finally, the experiment was conducted to study the performance of the turbine along with the sediment erosion patterns on blades which can be compared with the numerical analysis results in order to validate them.

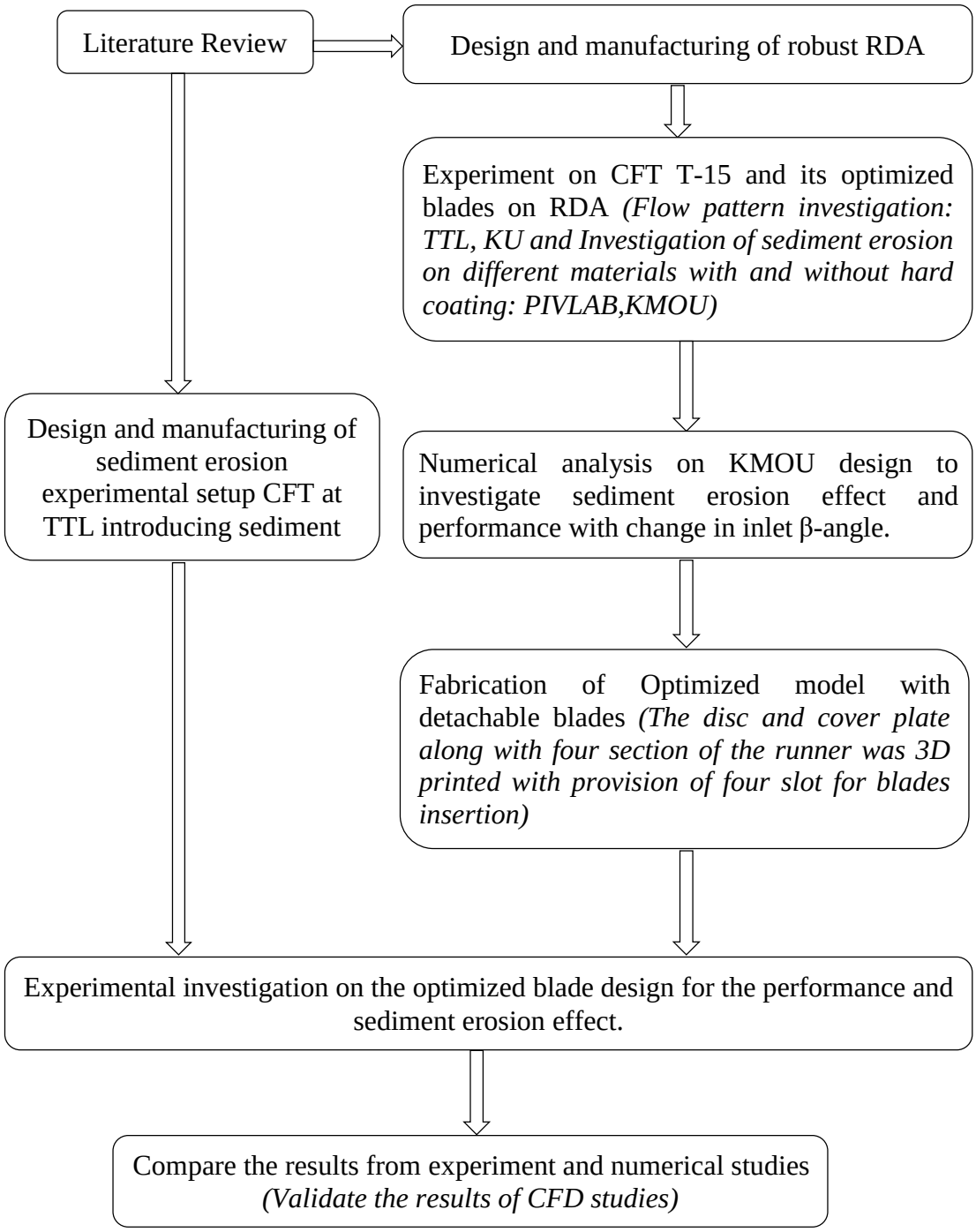

Figure 1-2: Methodology

1.6. Scope and Limitations

This research includes experimental investigation of T-15 blades using RDA so as to optimize the design of T-15 which is carried out both at TTL-KU and KMOU. The numerical investigation on KMOU design was carried by varying only the blade inlet angle as it has a significant effect on sediment erosion behaviour. The experiment was carried out on the same CFT with a decrease in the width of the runner by 249 mm. All of the experiments were carried out on an erosion testing rig at TTL.

The project does not include numerical analysis, design and testing of any other components besides runner blades.

1.7. Outline of thesis

This thesis is divided into 6 chapters. This chapter presents the background of the proposed topic, along with its significance and outline of the report. This chapter briefly explains why this research topic is selected through the explanation of the background and its essence in future of characterizing sediment erosion. It also mentions its upshot for the benefit of micro hydropower plants where sediment erosion is a major problem.

Chapter 2 introduces the working principle of the crossflow turbine. It also contains previous research and development works done on CFT and RDA. It highlights previous studies completed to date including the mechanism of wear due to sediment flowing along with water into the turbine. It also mentions several erosion models in order to calculate the erosion effect on the surface due to abrasive particles.

Chapter 3 contains the design and development of RDA along with the discussion of the procedures and results of the experiment that are obtained from the study of different designs of blades.

Chapter 4 deals with the investigation of the effect of different inlet blade angles on sediment erosion effect on CFT with the help of CFD. For that, five different cases have been considered by taking five blade inlet angles and varying flow, RPM as well as a number of blades for these five different kinds of blades. The procedures for CFD studies along with the results have been discussed in detail in this chapter.

Chapter 5 includes the design and development of the erosion testing rig in addition to the procedure of the experiment. The findings of the experiment and its comparison with the CFD results have been discussed in this chapter. Finally all the conclusions and the recommendation have been discussed in chapter 6 which is followed by reference and appendix section.

CHAPTER 2:LITERATURE REVIEW

2.1. Introduction of Crossflow Turbine (CFT)

Weir or small dam is built to divert flowing river water into the waterway. The water is directed to the crossflow turbine (CFT) to harness the water energy into mechanical power. The major components of a crossflow turbine are nozzle, guide vane and runner as indicated in Figure 2-1.

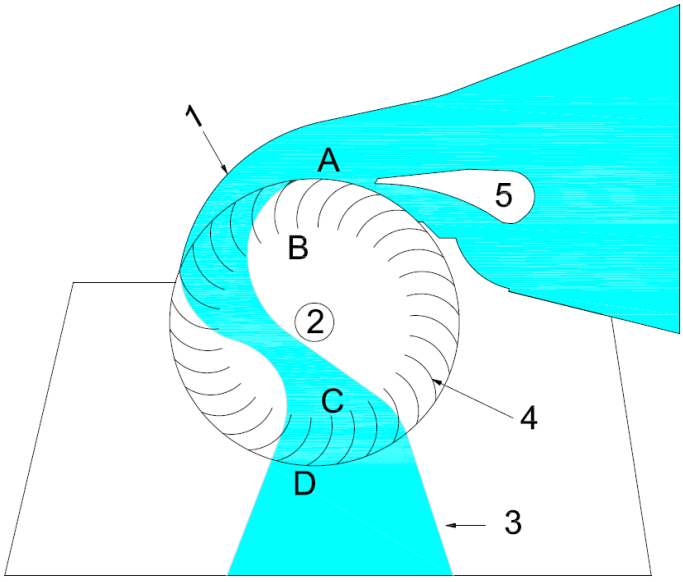

Figure 2-1: Schematic diagram of section of crossflow turbine

A nozzle controls the water flow entering the blades of a runner. The kinetic energy of the water that enters and leaves the runner at atmospheric pressure creates a change in angular momentum. It enables the runner to extract the power. The water flow inside the runner is complex. The water enters the runner with a substantial circumferential velocity, travels almost diametrically and dramatically through the center airspace, and then exits the runner with reference to the rotation axis. The flow passes through the first stage blades before departing the runner at atmospheric pressure, then traverses the center portion of the runner and flows through the second stage revolving blades.

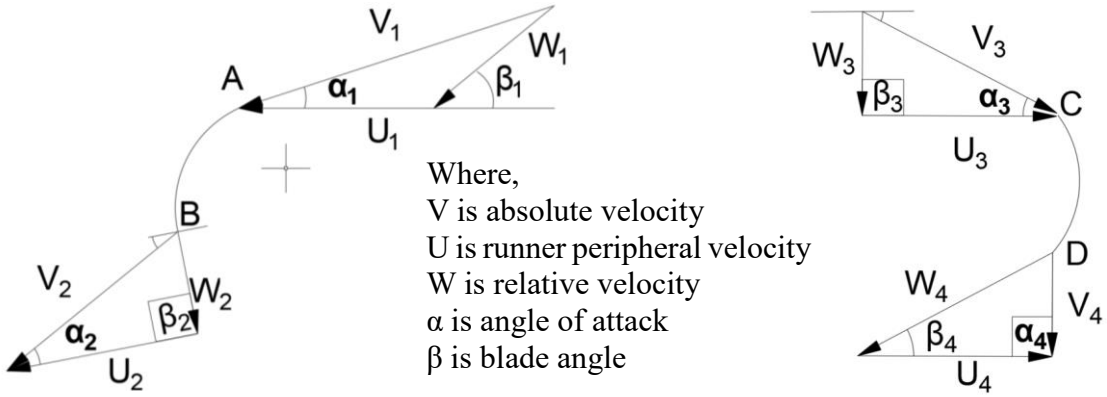

Figure 2-2: Velocity diagram at a different stage

Cross flow turbines are classified as impulsive radial turbines [6] because of their unique flow characteristics and ability to operate at atmospheric pressure. A guiding vane in the nozzle of the crossflow turbine aids in maintaining high velocity at an appropriate flow angle during part-flow operations.

In turbomachine, a velocity triangle/diagram is a key design parameter. It represents various components of velocities of the water flowing at the inlet and outlet sections of a turbomachine. The triangles indicate the magnitude and direction of the velocity of the water. **Error! Reference source not found.** is a schematic illustration of a velocity diagram without a flow control device i.e., guide vane.

2.2. Research and developmental status in design modification of CFT

The original design and patent of the crossflow turbine were owned by the Australian engineer, A.G.M Mitchell in 1903. Later, Donat Banki further carried out a study on CFT and received a patent for his Banki-Turbine. This turbine applied the crossflow principle, where a free jet transversed a cylindrical runner vertical to the turbine shaft. His work evolved a theory of operation and achieved an efficiency of 87.7 % [7]. The crossflow turbine T-series Development was found to be initiated by the Swiss technical co-operation agency Helvetas with an establishment of the first workshop named BYS (Balaju Yantra Shala P Ltd.) in Nepal in 1960 with an objective to create a minimal industrial infrastructure needed for repair and maintenance of the equipment used in the MHPs [8].

Table 2.1: History of Crossflow turbine T-series

Year	Series	Design	Remarks
1976	T1	Design re-improvement to optimize production	Used for mill operation and village electrification
1980-1982	T3	Design based on laboratory test in the hydraulic laboratory of HTL Brugg, Switzerland	Used for small scale mill operation
1985	T7	Designed to obtain larger output	
1987-1993	T8	Improved version of T7 series	Used for village electrification in Indonesia
1995	T12	Empirical design improvements based on testing at the hydraulic laboratory of University of Stuttgart	Implemented for complete SHP projects
1996	T13	Optimized design after series of different hydraulic configurations testing and from field testing	Implemented for complete SHP projects
1996	T14	Empirical design improvements based on testing at the hydraulic laboratory of University of Stuttgart	Implemented for complete SHP projects

The development of CFT T-series from T-1 to T-14 with continual design improvements are enumerated in Table 2.1. T-15 turbine was designed by consortium of GTZ, ENTEC AG and the Institute fuer Stroemungsmechanik und Hydraulische Maschinen, University of Stuttgart and further development was done in Switzerland [9]. The test turbine of 29 kW with a runner diameter of 300 mm was tested at laboratory of the Institute for Hydraulic Machines of Stuttgart University. A good part load efficiency of over 50 % was obtained with only 20 % of the rated flow [9].

2.3. Studies on Crossflow Turbine

Many researchers have studied the flow and performance characteristics, the influence of design parameters on the efficiency of CFT experimentally, theoretically and numerically.

2.3.1. Theoretical studies

There have been numerous theoretical studies relating to the effects of design parameters on the efficiency of the CFT. Table 2.2 shows the results of theoretical studies achieved to show the power output i.e. efficiency achieved during operation to shaft power.

Table 2.2: Theoretical efficiencies of CFT

Study	Study year	Efficiency (%)
Mockmore and Merryfield [7]	1949	87.8
Heimerl [10]	1960	82
Durali [11]	1976	60

Mockmore and Merry Field [7] presented the descriptive analytical design of a crossflow turbine and demonstrated that at various gate openings, maximum efficiency can be achieved at constant head and speed making it suitable for efficient operation. They suggested that setting the angle of attack α equals to16 ° can be a good compromise to obtain maximum hydraulic and structural efficiency. Hamierl [10] measured the efficiency of the turbine and investigated the effect of design parameters on the performance of the turbine. He calculated the speed of the turbine as 41 rpm, assuming a hydraulic efficiency of 82 %. Durali [11] reported the design of a crossflow turbine and presented the theoretical characteristics curve at constant flow rate and speed.

2.3.2. Experimental studies

Following the works of Mockmore and Merry Field [7], several experiments were carried out to investigate the influence of geometrical parameters on turbine performance [11] [12] [13] [14] However, most of the studies had not emphasized the

need of the study of underlying flow physics and flow characteristics that govern the design of the crossflow turbine.

Most of the experiments conducted studied the influence of the angle of attack α on the efficiency of the turbine. Fay and Durgin [15]and Khsorowpanah et al. [13] conducted a series of experiments and found the maximum efficiency of 61 % and 80 % respectively for α= 16°. Fiuzat et al. [16] and Aziz and Desai [17] found the maximum efficiency of 89 % and 85 % respectively for α= 24°. The research by Aziz and Desai [17] concluded that the turbine efficiency decreases with an increase of the angle of attack at the first stage from 22^o to 32^o. Likewise, Totapaly and Aziz [18] reported the maximum efficiency of 92 % at α= 22°. The value of peak efficiency observed in these experiments is inconsistent, ranging from 68 % [7] to a high value of 92 % [18]. The reason behind the inconsistency lies due to the assumption of the lower nozzle wall at the impeller inlet as α. Table 2.3 shows the list of experiments conducted by the previous researchers for different design parameters used.

Likewise, Fiuzat and Akerkar [16] performed experiments to identify the contribution of the two stages of power generation to the shaft power with and without the use of a flow diverter. Experiments were conducted with five nozzles configurations for the same throat width ratio of 0.41. Flow patterns were recorded and analyzed by plotting them on a square grid. The study reported that the higher efficiencies in both stages of the turbine occur at 90 ° nozzle arc entry angle θ_s which is in good agreement with the study conducted by Nakase et al [19] and Khosrowpanah [20] . The study stated that the contribution of the second stage to the total power is at least 45 % for a nozzle entry arc of 90^0 and 41 % for the 120◦ nozzles. The study further proposed that the performance of both stages can be upgraded by increasing the cross-flow inside the runner. Similarly, Durgin and Fay [21] conducted an experimental study to study the flow pattern inside the runner using high-intensity stroboscope and photographic techniques. The visual port is provided at one end of the runner casing. They placed a flow deflector inside the runner to determine the efficiency contributions of each stage. Results showed that the first stage contributed about 83 % to the total output power.

However, this study is limited to part flow conditions due to complex flow interactions that occurred at a design flow rate.

Table 2.3 List of experiments by various researchers based on empirical values of design parameters

Researchers	Head	Flow rate	Speed	D_2/D_1	N_b	α	θ_s	η %
Mockmore &Merryfield [7]	2.7-5.5	62.9	270	0.66	20	16	38	68
Durgin & Fay [15]	10			0.68	18	16	63	61
Khwosrowpanah [13]	0.33-2.6	20.4-44.2	87-356	0.68	15	16	90	80
Fiuzat &Akerkar [22]				0.66		24	90	79
Aziz & Desai [17]	0.34	25.6		0.68	25	24	90	85
Totapally &Aziz [18]				0.68	35	22	90	92
Joshi et al. [23]	2-9			0.66	24	16	36	65
Costa Pereira & Borges [24]	0.89-5.2			0.66	25	15	80	74
Reddy [25]	3-9	90	30	0.66	24	16	36	67
Olgan [26] [27]	4-30	14-15	400-1300	0.67	24	16	46	72
	4-30	14-15	969-1107	0.54	24	16	46	70
Walseth [28]			350	0.69	12	12	120	66

Where, Head = (m); flow rate= l/s; speed = RPM; Diameter ratio =(D_2/D_1); Number of blades = (N_b); Angle of attack = (α); Admission angle = (θ_s) degree; Efficiency = (η %)

The effect of the number of blades N_b on turbine efficiency has been investigated by experimental studies [12] [20] [18] [17]. Fukutomi [12] reported the difference in efficiency between 22 and 34 number of blades to be 3 %, observing the maximum efficiency at N_b = 30. Khosrowpanah [13] observed an increase in efficiency when the number of blades increased from 10, 15 and 20, and reported maximum efficiency of about 80 % for the runner with 15 number of blades.

Totapally and Aziz [18] also conducted an extensive series of experiments to investigate the influence of a number of blades and reported the maximum efficiency of 88 % and 90 % respectively for increasing the blade's number from 30 to 35. Likewise, Aziz and Desai [17] conducted experiments with the number of blades increased from 15-25 and observed an improvement in the turbine efficiency. The increment in the blade number showed an increment in the turbine efficiency due to a consistent velocity profile that exists in the spaces between the blades. However, increasing the number of blades also increases the weight of the runner making it susceptible to vibration and frictional losses. Also, the flow characteristics changes due to change in the spaces of the flow passages between the blades i.e. the blade passage can be choked or obstructed.

In another study by Aziz and Desai [17] and Joshi et al. [23], the ratio of the inner to the outer diameter of the turbine has an influence on the efficiency of the turbine. The optimal diameter ratio D_2/D_1 is found to be 0.68 from the literature as mentioned in Table 2.3. This ratio is responsible for the energy extraction from the first and second stages as the size of the air spacing inside the impeller varies with it. This results in a change in flow characteristics inside the impeller. However, the study of turbine performance and flow field inside the runner due to change in diameter ratio is not conducted yet.

Costa Pereira et al. [24] performed an experimental study of the nozzle flow in a cross–flow turbine. He investigated the effect of two different nozzle configurations on static pressure distribution on the inner walls of the nozzle, subjected to runner and without runner. The results revealed that the pressure distribution was effected by the presence of a runner and the pressure distribution varied significantly with the non–dimensional volume flow rate. In a comparison between two nozzles configurations with and without guide vanes, a test revealed that the one with the guide vane showed better flow distribution giving a higher efficiency.

Blade exit angle is also an important parameter to study the influence on the performance and the flow conditions of a crossflow turbine. The study by Fukutomi [12] reported the effects of the blade exit angle and found that exit angle $\beta_2 = 90°$ gives

the optimum turbine performance. Similarly, Desai [17] and Totapally et al [18] found that β_2= 90° and β_2= 55° gave the maximum efficiency respectively. It is suggested here to keep the exit blade angle at optimum because a large value causes a separation of flow at the leading surface of the first stage exit part due to a larger turning angle.

2.3.3. Numerical studies

Apart from experimental analysis, various numerical simulations were conducted to visualize the flow field in the runner and provide a basis for designing highly efficient turbines. Several attempts have been made to optimize the turbine performance by altering nozzle designs and runner geometric parameters. These factors have considerable effects on the flow characteristics of the turbine which further influence the performance. Despite several experimental data that have been used for the improvement of the design, the study on the flow characterization in the turbine is not studied in detail. Recent computational studies [29] [30] [31] have used 3D steady state RANS simulation for predicting the turbine performance and validation.

Choi et al. [29] performed an entire 2D CFD steady state simulation by considering both water and water-air flow conditions. The study has used *k-ω SST* model and *k-ε* model for single-phase flow and two-phase flow calculations as turbulence models. He reported that the performance and internal flow characteristics of the turbine are highly influenced by the shape of the nozzle, runner blade angle and blade number. Further, the study concluded that admission of air layer through air suction pipe in the runner passage has improved the efficiency by reducing the collision losses between the flow passage and the shaft. Moreover, Chen and Choi [32] conducted a CFD analysis of the crossflow turbine to investigate the performance and internal flow characteristics of the turbine in detail. They concluded the efficiency of the turbine increases approximately proportional to increasing air layer area in the turbine chamber along the runner casing's side wall.

Croquer et al. [33] performed a transient regime, a 2D numerical model of CFT using Eulerian-eulerian homogenous model and SST turbulence model. Based on the CFD

results without the use of Internal Deflectors (ID), Superior Blade Position and Internal Deflector Length were defined for six different versions of ID.

Table 2.4 the recent computational studies carried out on the crossflow turbine

Researchers	**Head**	**Flow rate**	**Speed**	**D_2/D_1**	**N_b**	**α**	**θ_s**	**η %**
Choi [29]	29				15,26, 30	25,30, 35	120	65.7
Kokubu et al. [34]					30	30	87	62.9
Croquer et al. [33]				0.62	24	16		72
De Andrade [30]	35	135	1000	0.68	24	16	70	75
Sammartano [31]	14.2	60	757	0.64	35	22	90	85.6
Chen and Choi [32]	20	465	530		30			81.3
Acharya [35]	10	100	642		22			80.7
Adhikari [36]	3-10	56-105	200-700	0.66	20	16		69.9
Chichkhede et al. [37]	5		350		24	12,15, 18	90	70.7

Where, Head = (m); flow rate= l/s; speed = RPM; Diameter ratio =(D_2/D_1); Number of blades = (N_b); Angle of attack = (α); Admission angle = (θ_s) degree; Efficiency = (η %)

This study attempted to investigate the effect of ID on CFT performance. The results reported that the efficiency of the turbine increases with use the use of ID, however, care must be taken to optimize the length of ID in order to avoid frictional losses, especially at ID trailing edges.

Kokubu et al. [34] conducted a numerical simulation on the cross flow that has an anti-recirculation block (ARB) inside the runner. He investigated the influence of ARB on the fluid-flow characteristics and the turbine performance. It was observed that collision loss due to the interaction between runner flow passage and shaft is reduced significantly. At the same time, the re-circulation flow regime is reduced, resulting in a better crossflow pattern inside the runner. He further suggested that the performance of the CFT can be increased by increasing the width of the nozzle and flow rate that further aids in reducing frictional losses.

Andrade et al. [30] conducted the numerical analysis of the internal flow using 3-D steady RANS (Reynolds Average Navier Stokes) computations with a water-air homogenous free surface model and k-ε turbulence model. The study compared experimental efficiency with numerical hydraulic efficiency for different runner speeds. The results showed that 68.5 % of the energy transferred occurred in the 1st stage, and the remaining 31.5 %is transferred in the 2nd stage. It can be concluded that the water flow inside the impeller contains appreciable energy that is translated during the second stage, which then contributes to the overall efficiency of the turbine. Also, the velocity and pressure fields of the crossflow within the runner were analyzed for the runner speeds of 400, 600,8 00 and 1200 rpm. Fluid dynamic phenomena as shocks with the runner shaft, recirculation flow zones between the flow passages and non-cross-flow were the insights from the simulation results.

Similarly, Sammartano et al. [31] have proposed a two-step design procedure of cross flow runner. The first step is the design of the outer diameter of the impeller D_1 and the blade attack angle β_1, for given water discharge Q and hydraulic head H, as well as of the nozzle profile. The second step comprised of optimizing the inner diameter D_2 for different values of diameter ratio D_2/D_1, inner blade radius, angle of attack, the number of blades and their profiles by following a computational approach. The study recorded the number of blades and diameter ratio has a negligible effect on the peak efficiency, however, the study presented that the presence of shaft does not affect the characteristic curve. On the contrary, it influences efficiency by a significant value.

Acharya et al. [35] conducted numerical simulations for a two-phase (Air-Water) steady state using the SST turbulence model in ANSYS CFX 13.0. A study was carried out to analyze fluid-flow characteristics in the turbine by modifying the nozzle shape, altering the guide vane angle and changing the number of blades. The efficiency of the turbine is increased from 63 % to 76 % for modified guide vane opening angle of 7° and 22 numbers of blades. The study investigated the velocity profiles and pressure distribution as well as the internal flow pattern. It was observed that the energy loss due to the re-

circulating flow region inside the runner is reduced. However, the extraction of the power in the two different stages is not studied.

Adhikari et al. [36] carried out the cavitation study in a crossflow turbine using 3D RANS computations with SST k-ω turbulence models and a homogenous, free surface two-phase flow model. The study observed cavitation on the suction side near the inner edges of the blades in the second stage of the turbine and, at higher impeller speed for constant flow rate and head. The study emphasized the cavitation phenomenon that occurs in the crossflow turbines. However, this study is limited to the study of the size and strength of cavitation bubbles and, its impact on turbine performance.

Chichkhede et al. [37] investigated the influence of nozzle opening angles and water inlet angle on the performance of the CFT through 3D flow simulation. Numerical tests were carried out for 40 %, 60 %, 80 % and 100 % of nozzle opening and, for varying water inlet angles of 12^0, 15^0, and 18^0 as well as for inlet blade angle from 24^0 to 30^0. The results revealed the efficiency of the turbine is dependent on blade angle at different nozzle openings.

2.4. Wear

The loss of material as a result of mechanical impact on the surface of the flow passage of the components is termed wear.

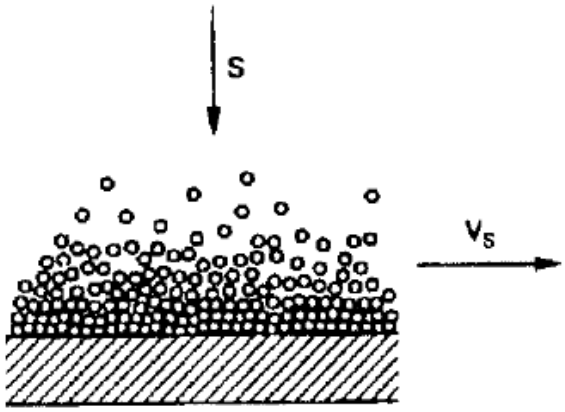

Figure 2-3 Sliding Abrasion [38]

Wear can be categorised into different types, however, for hydraulic machinery abrasive and erosive wear are taken as the major ones. Abrasive erosion is the removal of the materials as a result of bed particles sliding over the surface with a velocity vector parallel to the surface which is a purely cutting removal process.

When particles collide with the surface of materials with a velocity and angle, erosion wear can be observed. Material deformation, sliding, fatigue cracking or a combination of all of these are the result of the continuous impact of harder particles sliding or colliding on the surface. Damaged surface gradually changes its shapes from a small pitting to a fish scale or wave shaped groves and an ultimately small amount of materials tear away [39].

Abrasion and Erosion rate depends upon velocity, material hardness, grain size and concentration of solid which can be observed from the following relations

$$wear \propto (velocity)^n \tag{2.1}$$

Sediment erosion first declines the efficiency and slowly reduces the time between successive repair and maintenance works. According to Bak and Bergeron [40] [41].

$$\text{life } \propto = \frac{1}{(total\ head)^{\frac{3}{2}}} \quad i.e \quad \propto \frac{1}{wear\ rates} \tag{2.2}$$

Where the index n depends on materials and other factors and is generally taken as 3 [42].

Similarly, Bak argues that other factors are there that affects wear and tear and formulated the following formula.

$$\text{T(life in hours)} = \text{A}\frac{KQ^n}{H^{\frac{3}{2}}W_sX} \tag{2.3}$$

Where,

A= constant factor, Q^n= Concentration of solid in mixture (%),

K = Impeller shape factor (1.0 for multi-bladed impellers, 1.4 for channel impeller), H = total head/stage, $W =$ coefficient of abrasive wear for impeller material and

$X =$ Coefficient of abrasiveness of solids

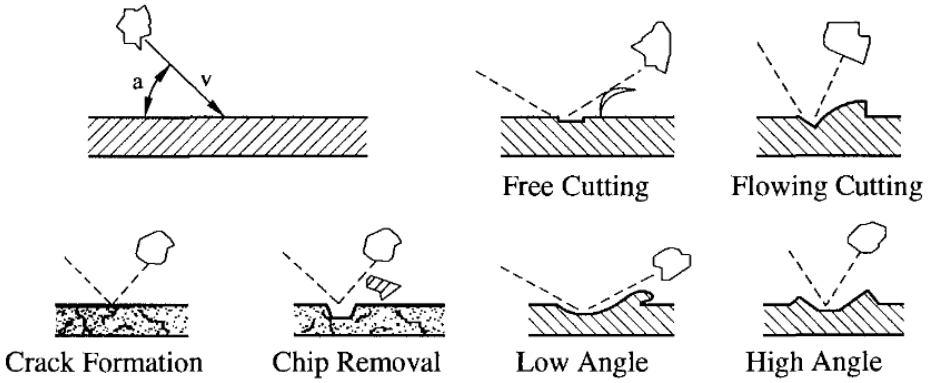

Figure 2-4:Impact Erosion

Similarly, Bain et al. [42] [43] developed correlations to predict the erosion rate

$$W = KV^{\beta} d^{\gamma} C^{\emptyset} \quad (2.4)$$

Where W= erosion rate,

V= the velocity of a particle,

d= particle size,

C= solid concentration and

K, β, γ and Φ are constants that depend on the properties of the erodent as well as the target material.

Sediment erosion for different materials can be predicted by the equation as suggested by Naidu [44]

$$W = S_1 S_2 S_3 S_4 M_r V^x \quad (2.5)$$

Where,

$S_1 =$ the coefficient of silt concentration

$S_2 =$ the coefficient of silt hardness

$S_3 =$ the coefficient of silt particle size

$S_4 =$ the coefficient of silt particle shape

$M_r =$ coefficient of wear resistance of base material and

$v =$ the relative velocity of the water.

2.5. Computational fluid dynamics

For analyzing and solving complex fluid dynamics problems computational fluid dynamics (CFD) has been widely used in the past two decades. It is a mathematical modelling tool that incorporates Reynolds-average Navier Stokes (RANS) for the solution of fundamental equations of the fluid flow using different turbulence models.

2.5.1. Turbulence Modelling

Turbulence is almost universal in all real-world problems. The Navier-Stokes equations attempt to solve the problems involved in turbulent flows which are based on both laminar and turbulent flow but do not account for the additional eddies which are always there in any realistic problems. That is the reason why the inability of Navier–Stokes equation has resulted in a search for several models to account for turbulent fluctuations. Hence, turbulence models have modified transport equations with the addition of average and fluctuating components and for predictions of such turbulences inflows, ANSYS CFX provides a large number of turbulence models. However, these models in fact cannot predict and solve all the thinnest eddies formed in any problems which need large computational power and time and only be solved by Direct Numerical Solutions (DNS). A more robust model for solving these eddies is Large Eddies Simulations (LES) in which the thinnest scale eddies are modeled and the rest are resolved which again takes a lot of time and computational power. So, two-equation turbulence models are quite popular while solving the problems using CFD which provides a good compromise between computational power, time and accuracy. There are several

combinations of such equations to get suitable models such as k-ε, k-ω, SST models and so on.

2.5.1.1.k-ε Turbulence model

This model is more accurate for free stream regions but fails in vicious sub-layer like flows over a curved surface and rotating fluids. In this model '**k**'s is introduced as the turbulent kinetic energy and '**ε**' as the turbulence eddy dissipation. The continuity equation is

$$\frac{\partial \rho}{\delta t} + \nabla(\rho U) = 0 \qquad (2.6)$$

The momentum equation is changed and is given as:

$$\frac{\partial \rho U}{\partial t} + \nabla(\rho U \otimes U) = -\nabla p' + \nabla\{\mu_{eff}(\nabla U + (\nabla U)^T)\} + S_M \qquad (2.7)$$

Here,

S_M = the sum of body forces,

μ_{eff} = effective viscosity

p = the modified pressure.

The effective viscosity is given as:

$$\mu_{eff} = \mu + \mu_t \qquad (2.8)$$

Where μ_t is referred to as turbulence viscosity linked to the turbulence kinetic energy dissipation by the equation:

$$\mu_t = C_\mu \rho \frac{k^2}{\epsilon} \qquad (2.9)$$

Where C_μ is a constant.

The values for k and ε come from the differential transport equations for the turbulence kinetic energy and the turbulence dissipation rate.

The turbulence kinetic energy equation is given as equation:

$$\frac{\partial(\rho k)}{\partial t} + \nabla(\rho U k) = \nabla\left[\left(\mu + \frac{\mu_t}{\sigma_k}\right)\nabla k\right] + P_k + P_{kb} - \rho\epsilon \quad (2.10)$$

The turbulence dissipation rate is given by the equation

$$\frac{\partial(\rho\epsilon)}{\partial t} + \nabla(\rho U \epsilon) = \nabla\left[\left(\mu + \frac{\mu_t}{\sigma_\epsilon}\right)\nabla\epsilon\right] + \frac{\epsilon}{k}(C_{\epsilon 1}(P_k + P_{\epsilon b}) - C_{\epsilon 2}\rho\epsilon) \quad (2.11)$$

Where, $C_{\epsilon 1}$, $C_{\epsilon 2}$, σ_k, σ_ϵ are constants.

2.5.1.2. k-ω turbulence model:

It provides robust as well as accurate results for viscous sub-layer but is highly sensitive with the free stream region solutions. It also requires more memory and is difficult to convergence with highly sensitive while initial guessing at the solution. In this model, turbulence kinetic energy is referred to as 'k's and turbulent frequency as 'ω' which is given by the equation:

$$\mu_t = \rho\frac{k}{\omega} \quad (2.12)$$

The transport equation for 'k' is given by the equation:

$$\frac{\partial(\rho k)}{\partial t} + \nabla(\rho U k) = \nabla\left[\left(\mu + \frac{\mu_t}{\sigma_k}\right)\nabla k\right] + P_k + P_{kb} - \beta'\rho k\omega \quad (2.13)$$

And the transport equation for 'ω' is given by:

$$\frac{\partial(\rho\omega)}{\delta t} + \nabla(\rho U \omega) = \nabla\left[\left(\mu + \frac{\mu_t}{\mu_\omega}\right)\nabla\omega\right] + \alpha\frac{\omega}{k}P_k + P_{wb} - \beta\rho\omega^2 \quad (2.14)$$

Where, β', β, σ_k, σ_w, α are constants.

2.5.1.3. SST turbulence model:

This model is a widely used model in ANSYS CFX for solving problems of turbo machinery as it is the combination of both k-ε and k-ω models. It tends to acts as a k- ε model far from the walls and a k-ω model close to walls. For some problems, the convergence time of the SST model is large, so it is often followed by a couple of solutions using k-ε and k-ω models in order to get the initial conditions.

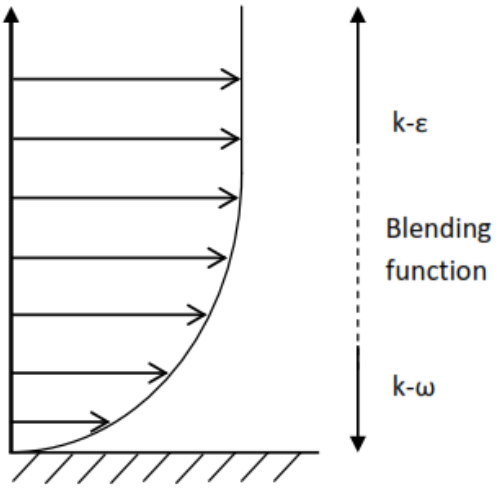

Figure 2-5: Schematic representation of transition SST model [45]

The transport equations for Shear Stress Transport is expressed as

$$\frac{\partial k}{\partial t} + \nabla(uk) = P_k - \beta^* k\omega + \nabla[v + \sigma_k v_T]\nabla k \qquad (2.15)$$

Where

turbulent kinetic energy ‘k's and

the turbulent frequency or dissipation per unit kinetic energy ‘ω’ are computed by using

P_k = the production limiter.

For Specific Dissipation rates,

$$\frac{\partial \omega}{\partial t} + \nabla(u\omega) = \alpha S^2 - \beta\omega^2 + \nabla[(v + \sigma_\omega v_T)\nabla\omega]2(1 - F_1)\sigma_{\omega 2}\frac{1}{\omega}\nabla k\nabla\omega \qquad (2.16)$$

The first blending function F_1 is calculated from

$$F_1 = \tanh\left\{\left\{min\left[max\left(\frac{\sqrt{k}}{\beta^*\omega y};\frac{500v}{y^2\omega}\right)\frac{4\rho\sigma_{\omega 2}k}{CD_{k\omega}y^2}\right]\right\}^4\right\} \quad (2.17)$$

$$CD_{k\omega} = max\left(2\rho\sigma_{\omega 2}\frac{1}{\omega}\nabla k\nabla\omega 10^{-10}\right) \quad (2.18)$$

And, Kinematic eddy viscosity,

$$\mathrm{v_T} = \frac{\alpha_1 \mathrm{k}}{\max(\alpha_1\omega, \mathrm{SF}_{2)}} \quad (2.19)$$

Where S is the invariant measure of the strain rate and F_2 is the second blending function expressed as:

$$F_2 = \tanh\left[\left\{max\left(2\frac{\sqrt{k}}{\beta^*\omega y};\frac{500v}{y^2\omega}\right)\right\}^2\right] \quad (2.20)$$

Each of the constants is a blend of an error of an inner (1) and outer (2) constant, blended through

$$\emptyset = \emptyset F_1\emptyset_1 + (1 - F_1)\emptyset_2 \quad (2.21)$$

Where $\emptyset_1$ and $\emptyset_2$ are the coefficients of the k-ω and k- ε models respectively.

The turbulence viscosity is calculated by,

$$v_T = min\left(\frac{\rho k}{\omega}, \frac{a_1\rho k}{SF_2}\right) \quad (2.22)$$

Where, a_1, α_1, α_2, β_1, σ_{k1}, σ_{w1}, σ_{w2} are constants.

The $y^{+\text{ values}}$ for the SST model should be close to 1 so as to account for the physics of flow in viscous sublayer.

2.6. Methodology and Design of Erosion Testing Apparatus

Laboratory tests are conducted to study the basic wear mechanism and to investigate the effect of various erosion influencing factors on the erosion rate of different base materials, particularly caused by the impact of sediment particles. Generally, these tests are performed to rank the erosion resistivity of the test specimen materials and/or turbine

materials. Sediment erosion test procedures are basically categorized into two parts: pipe wear tests and laboratory tests [46]. Laboratory tests can further be divided into simulations tests and experimental tests. Though simulation tests are widely adopted for numerical prediction of erosion using available erosion models; and flexible and precise control of variables, validation of the obtained results in terms of nature and quantification is a challenging task. Thus, laboratory tests using test apparatus are preferred over field tests and scaled model tests as it requires less time to attain results and is relatively less risky than the prototype measurements due to the smaller-scale setup in a well-designed lab environment. Also, accelerated erosion tests are performed in precisely controlled laboratory conditions to shorten the test period for lower rates of erosion that takes place in the actual environment.

Complex interactions between various factors make it difficult to standardize the methodology and design of erosion testing apparatus. Numerous designs of erosion test rigs are in use to study the erosion phenomenon that occurs in industrial applications and hydropower plants. These can be classified upon the process of injecting erodent particles into the test chamber and expelling it out of the system after striking the test specimen. Further, these rigs are categorized into different types based on the motion of test specimens relative to the motion of fluid as shown in Figure 2-6: (a) Rotating type (b) Stationary type: (a) Rotary type test rigs, which further include Slurry pot, Rotating Disc Apparatus, Whirling arm and Coriolis type (b) Jet- type test rigs. Among these test rigs, the most commonly used test rig is jet type test rig with the rotating specimen and re-circulating slurry. And most of the experiments are conducted on small size rotating and stationary test specimens made up of different base materials.

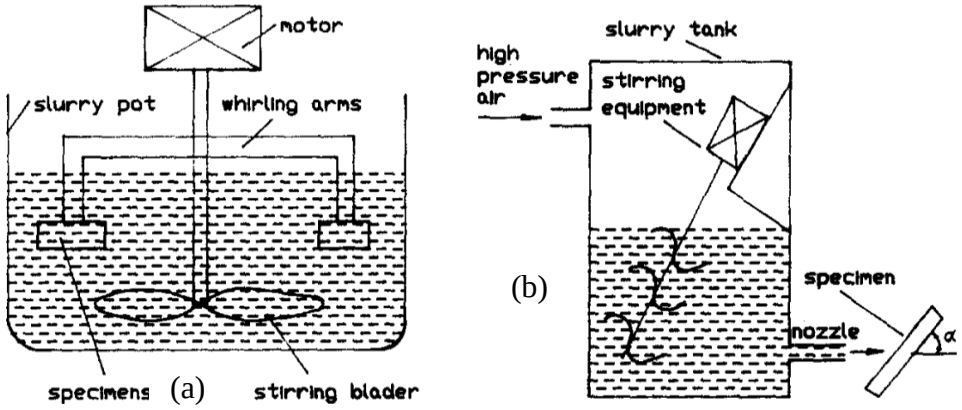

Figure 2-6: (a) Rotating type (b) Stationary type [47]

2.6.1. Jet type test rigs

These types have been commonly used for slurry erosion experiments [46] [48] [49] [50]. A number of studies could be found in the recent literature where jet-type test rigs have been used for experimentations, particularly for erosion studies of impulse type of turbines in recent years [51] [52]. Based on the jet velocity, erosion caused at velocities greater than 6-9 m/s and less than 6 m/s can be termed as high-velocity erosion test rig [53] [54] [55] [56] and lower velocity erosion test rig [46] respectively. Further, jet type test rigs can be classified into re-circulating type (RC) and non-recirculating type (NRC). In the former type, the same abrasives are circulated in a loop for a definite test duration whereas fresh abrasives are injected into the system at each cycle in the latter type. In RC types, the erosion rate is influenced over time due to the degradation of particle shape after striking the test specimen.

Jet type test rigs can provide better parameter variation and control. However, in the case of stationary specimen types, the slurry jet is locally concentrated on the specimen and the impingement angle of all abrasives particles may deviate during the test. Regular monitoring of the nozzle must be done to ensure no wear due to high impact velocity.

2.6.2. Slurry pot test rigs

This type has a very simple design and is generally used for ranking the erosion resistance for different materials [57] [58] as well as to evaluate the erosion behaviour

of materials [59]. This test setup facilitates the multiple tests of the samples at a time. However, the unstable flow of the slurry makes measurement and control of the velocity and impingement angle inaccurate. Also, the slurry degradation by fracturing and rounding of solid particles affects the erosion rate as the test progresses. Moreover, the uniform distribution of the slurry mixture is difficult to achieve throughout the vertical cross-section of the cylindrical pot. Further, complex flow conditions make it complicated to study the effect of erodent characteristics such as size, shape, and abrasiveness on erosion rate. A study by Gadhikar et al. [60] reported that the optimum speed of the stirrer is required for obtaining homogeneity of the mixture, which can be determined by visual inspection. The optimum stirrer speed was found at 850 rpm for the most uniform distribution of 300 μm sand particles over the vertical cross-section of the slurry of 10 % concentration in 20 l volume. And the use of downward pumping pitched turbine propeller is recommended to obtain a more uniform distribution of solids [61].

2.6.3. Whirling arm test rigs

This test rig developed by Lin and Shao [62] comprises mainly three units: a slurry unit, specimen rotation unit, and a vacuum unit. The test specimens, rotated by the electronically controlled motor are impinged by dropping slurry inside the vacuum chamber to eliminate the error caused by the airflow effect of the particles [63] Further, the impact velocity is measured by photoelectric velocity meter with an error < 2 % in the range of 10-70 m/s. This setup was used by Bukhaiti et al. [63] to investigate the influence of impingement angle on erosion mechanisms of 1017 steel and high-chromium white cast iron. He further characterized the erosion mechanism based on the range of impingement angle. This test rig can be used to simulate the erosion of a Pelton runner as the slurry jet strikes the rotating specimen. The test conditions such as the velocity of the jet and impingement angle can be measured and controlled accurately.

2.6.4. Coriolis test rigs

This type of test apparatus was developed by Tuzson [64], to investigate the slurry erosion interaction between the surfaces as in slurry pumps and stationary flow passages like pipelines. This device operates under the influence of centrifugal and Coriolis forces in a revolving rotor to pass slurry rapidly across a test surface, producing wear. The use of this device allows a comparison of erosion resistance of different materials tested for different concentrations by calculating the specific energy required for material removal when the wear volume is known [65]. These test rigs can be extensively used for solid impingement tests of materials impacting at a very low impingement angle. Such tests have been carried out to compare laboratory results with field results of components such as slurry pumps [66] [67].

Table 2.5 lists recent slurry erosion test rigs developed and modified version, and are categorized upon the arrangement of test specimens along with test conditions, abrasives injection, as well as rejection technique, employed.

Table 2.5: Review of slurry erosion test rigs

Author	SA	Rig Type	M	TC				I	RC/ NRC
				V	α	C	S		
Maan [68] [69]	R	NRC, RDA	13Cr4Ni, T410	75	0-90	1.5-10	135	Sand hopper	Drained out
	S	RC, Jet	SS, SMM, Ti alloy	18.2	60	2.5	225	Slurry chamber	NA
Wheeler [70]	S	RC, Jet	CS, NC, WC coatings	16, 28	30-90	2.1	135,235	Slurry chamber	NA
Dallaire [71]	S	RC, Jet	AS,MS,CS, Ni alloy, FS,DS, FSS	10	25,90	10	212-300	Slurry chamber	NA
Sugiyama [72] [73]	S	RC, Jet	SCS6 with coatings	10-40	15-90	1	40	Slurry chamber	NA
	S	RC, Jet	Al, Cu, CMSS, ASS, Cast steel	10	90	1	80	Slurry chamber	NA
Machio [74]	S	RC, Jet	WC coatings on SS	12.6	45,90	5	NA	Slurry chamber	NA
Shivamurthy [75] [76]	S	RC, Jet	LSA Coatings on 13Cr4Ni	8, 12, 16, 20	30	10	100	Slurry chamber	NA
	S	RC, Jet	LSA Coatings on 13Cr4Ni	12	30, 45, 60, 90	1	100,375	Slurry chamber	NA
Manisekaran [77]	S	RC, Jet	PPN and LH 13Cr4Ni	12	30,45, 60,90	1	<150, 150-300	Slurry chamber	NA
Santa [78] [79]	S	RC, Jet	Coatings on AISI 304	5.5		10	212-300	Slurry chamber	NA
	S	NRC, Jet	Coatings on CA6NM	75	15	0.4	212-300	Slurry chamber	NA
Yoganandh [80]	S	RC, Jet	Ni based high alloy white iron	25,30,35	30,60, 90	1,2,3	600	Sand hopper	NA

Nguyen [81]	S	ASTM-G73, RC, jet	SS SUS-304	10,15,20,25,30	90	0.5	150-180	Slurry chamber	NA
Burstein [82]	S	SRC, Jet	304 L SS	3.8	10-90	13.2	400-650	Suction at nozzle	Screen Filter
Lin [48] [83]	S	ASTM G73-93, NRC, Jet	TiNi SMA, SUS304 SS	74.2,82.9,90.8,99.5	15,30,45, 60,75,90	0.015-0.025	263-363	Suction at nozzle	Drained out
	S	ASTM G73-93, NRC, Jet	NiCrBSi Coating	82.9,90.8,99.5, 105,117.3	15,30,45, 60,75,90	0.015-0.025	263-363	Suction at nozzle	Drained out
Thapa [84]	S	NRC, Jet	16Cr5Ni SS	50	90	0.28	150,250, 250-500	Slurry Hopper	Discarded after test
Bajracharya [85]	R	NRC, Jet	Brass	NA	NA	Varying	NA	Sand feeding screw	De-silting basin
Padhy [86] [87]	R	RC, Jet	Brass	26.62,28.2, 29.75	NA	5,7.5,10	<90, 90-355	Slurry chamber	NA
	R	RC, Jet	Brass	26.62,29.7	NA	5-10	Up to 355	Slurry chamber	NA
Chauhan [50]	S	RC, Jet	13/4 MSS, 21-4-N NS	120	30.90	2.1	500-700	Slurry chamber	NA
Ahmed [60]	R	NRC, Whirling arm	Polymeric coating on Carbon Steel	15	30,45,60, 90	1	250-355	Slurry chamber	Discarded after test
Liu [88]	R	RC, Jet	X3CrNiMo 13-4 ZG230 450 42CrMo	120	NA	0.97-1.3	2.59-101.46	Slurry chamber	NA
Rajkarnikar [89]	R	RDA	Aluminum	<15	NA	85.9	125-200	Enclosed slurry chamber	NA

Grewal [90] [91] [92] [54]	S	RC, Jet	WC-Co-Cr Coatings on 13Cr4Ni, 16Cr5Ni	20,40,60	30,60, 90	5,10,15	58,155,252	Slurry chamber	NA
	S	Hybrid of RC and NRC, Jet	Aluminium, Cast Iron	25	10-90	0.1,0.25,0.5,0.75	25-500	Suction at nozzle	Filtration
	S	NRC, Jet	Ni-Al_2O_3 coating on CA6NM Steel	16	30,90	0.1	<300	Sand hopper	Filtration
	S	NRC, Jet	CA6NM	4,16	30,90	0.1,0.5	<300	Sand Hopper	Filtration
Khurarna [55]	R	RC,Jet	Brass	26.8,27.8,28.8	25	0.3,0.6, 0.9,1.2	50-390	Slurry chamber	NA
Rai [93]	R	RC, Jet	Bronze,16Cr5Ni, 16Cr4Ni,13Cr4Ni, 13Cr4Ni with Cr_2O_3 Coating,13Cr4Ni with WC-Co-Cr Coating	51.3,54.9,58.2,61.3	NA	0.5,1.5, 3	0-355	Slurry chamber	NA

Where,

SA- Specimen, **S-** Stationary , **R-** Rotatory, **M-** Specimen material, **TC-**technical parameters V-Velocity (m/s), **α-** Impingement angle (^{o}), **C-** sediment concentration (wt %), **S**-size of sediment(µm), **RC-** Recirculating type, **NRC-** Non Recirculating type, **CS**-Ni composites- Chromium Steel Nickel Composites, **WC**- Tungsten Carbide, **CS** -Chromium Steel, **ASS**-Austenitic Stainless Steel, **MS**-Martensitic Stainless Steel, **CS**- Chromium Steel, **Ni**- Nickel, **FS**-Ferritic steel, **DS**-Duplex Steel, **FSS**- Ferritic Stainless Steel **Al**-Aluminium, **Cu**-Copper, **CMSS**- Cast Martensitic Stainless Steel, **PPN**- Pulsed Plasma Nitrided, **LH**- Laser Hardened, **SMA**-Shape Memory Alloy, **NS**-Nitronic Steel

2.6.5. Rotating Disc apparatus

Initially, the experiment was conducted in RDA to investigate the factors influencing cavitation [94] [95]. Similarly, the use of RDA was carried out by Wood et. al [96] to study the cavitation's damage resistance of refractory metal alloys for the impellers operating at high suction specific speed as the flow field in RDA closely resembles the operating conditions of pumps. Later, the device was used for the study of erosion-resistant behavior of different materials [97] [98] [99]. Likewise, RDA has been used to study the combined effect of sand erosion and cavitation erosion components that are subjected to high velocity [100]. Several modifications to RDA were done to investigate the effect of particle sizes on erosion rate to study the wear pattern of the CFT blades [101], to select the optimum erosion-resistant profile of guide vane and blades of Francis turbine [89] [102], and also to analyze the erosion potential of different sized sediment particles collected from the Budhi-Gandaki-Trishuli river of Nepal [103].

CHAPTER 3: ROTATING DISC APPARATUS

This chapter consists of a study of the wear pattern and the erosion wear on CFT blades made up of different materials and coatings of the CFT blades. The specimen was painted to observe the wear pattern. The weight measurements of the specimen blades were carried out to estimate the rate of erosion. Additionally, the numerical study consists of Computational Fluid Dynamics (CFD) analysis conducted in the Rotating Disc Apparatus (RDA) under similar operating conditions. The simulated results were compared for hydraulics of flow in CFT and RDA.

3.1. Design of RDA

The RDA setup installed at Turbine Testing Lab (TTL) was designed by Prahlad Chaudhary [84] and, later re-developed by Rajkarnikar et. al [79]. In this study, RDA was designed based on the design parameters of CFT as tabulated in Table 3.1. An improvised version of RDA has been designed and developed at the Turbine Testing Lab (TTL), Kathmandu University and also in PIVLAB, Korea Maritime and Ocean University (KMOU) as shown in Figure 3.1. The manufacturing drawings are attached in Appendix B. The investigation of the pattern of wear on mild steel CFT runner blades was performed at TTL [85] whereas experiments were conducted on CFT runner blades with and without coatings at KMOU to quantify the sediment erosion by weight loss measurement method.

RDA consists of a rotor assembly with a disc, where multiple test specimens can be attached. The cylindrical housing of RDA is divided into the inner and outer chambers. The inner chamber provides a passage to cool the system via. circulating cold water while the outer chamber encloses the rotating disc attached to the shaft, the mounted test specimens and the sand-water mixture. The selection of motor capacity is done considering all the drag forces acting on the rotating components such as on the face of the disc, on the surfaces of the test specimens and the cylindrical surface of the disc. Similarly, the speed of the rotating disc is based on the relative velocity of water at the inlet of the runner blade and the location of the test specimen clamped on a disc.

Table 3.1: Design parameter of CFT

Description	Value	Unit
Net head	10	m
Designed flow rate	82	l/s
Runner diameter	200	mm
Width of runner	175	mm
Specific speed	38	-
Designed RPM	584	rpm
Relative velocity at the inlet of blade	7.77	m/s

The rotor speed of 720 rpm is achieved through type 'B' V belt with motor shaft pulley to disc shaft pulley ratio of 1:2. The rpm of the erosion tester is controlled using a variable frequency drive (VFD). The relative velocity of 12 m/s is calculated for the selected rpm of the disc. Assuming the mixture inside the housing to be stationary, the capacity of the motor to operate the RDA was determined by the total torque required to overcome the boundary layer drag force of the disc and test specimens. The total capacity of the motor was calculated as 1.5 kW considering hydraulic mechanical and electrical efficiency of 95 %, 75 % and 90 % respectively.

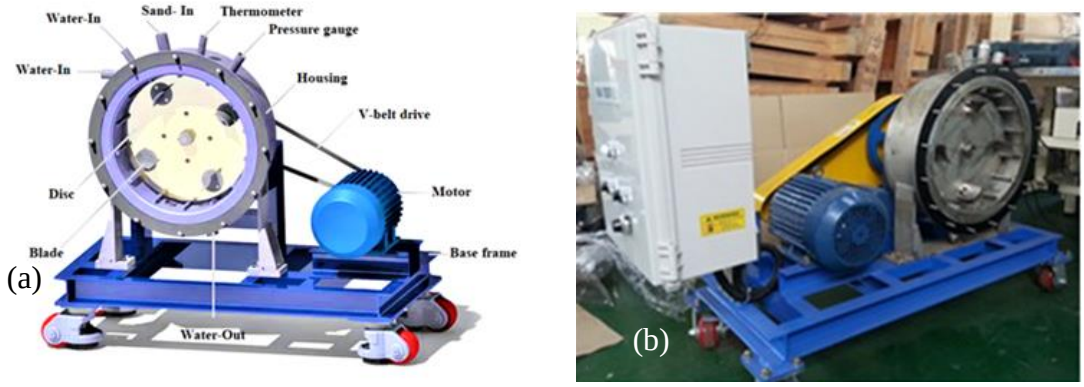

Figure 3-1: (a) 3D illustration of RDA and (b) RDA setup installed in KMOU

Thus, the capacity of the motor selected for the RDA was 5 kW. The detailed specifications of the RDA are tabulated in Table 3.2. Figure 3-2 shows the fabricated test setup installed at TTL.

Table 3.2: Specifications of the RDA

Description	Value	Unit
RPM of motor	1440	rpm
Speed of rotation of the disc	720	rpm
Relative velocity at the inlet of blade	12	m/s
Density of sediment	1072	Kg/m³
V-belt drive (Motor to the shaft)	2:1	-
The direction of rotation of the disc	Clockwise	-
The diameter of the disc	350	mm
The diameter of mounting of the specimen	320	mm
The Net volume of water in the casing	7.88	Liters
Number of the specimen used	4	No.
The power rating of the driving motor	5	kW

It consists of auxiliary units such as a chamber cooling system, power supply control panel equipped with temperature sensor and in-built rpm sensor. A temperature probe is inserted through the pipe to measure the temperature of the water during the test. A thermal cut-off switch is used to stop the RDA when the mixture temperature exceeds 70 °C.

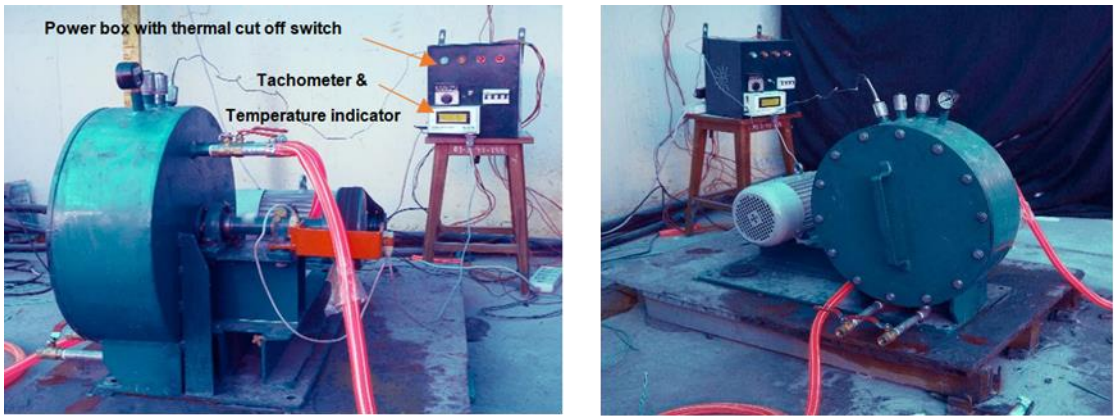

Figure 3-2 : RDA setup at TTL

3.2. Test specimen

3.2.1. Test specimen at TTL

CFT blades are used as test specimens to study erosion by the impact of sediment particles. The 2D and 3D modelling of the blades was performed using AutoCAD and CATIA V5.

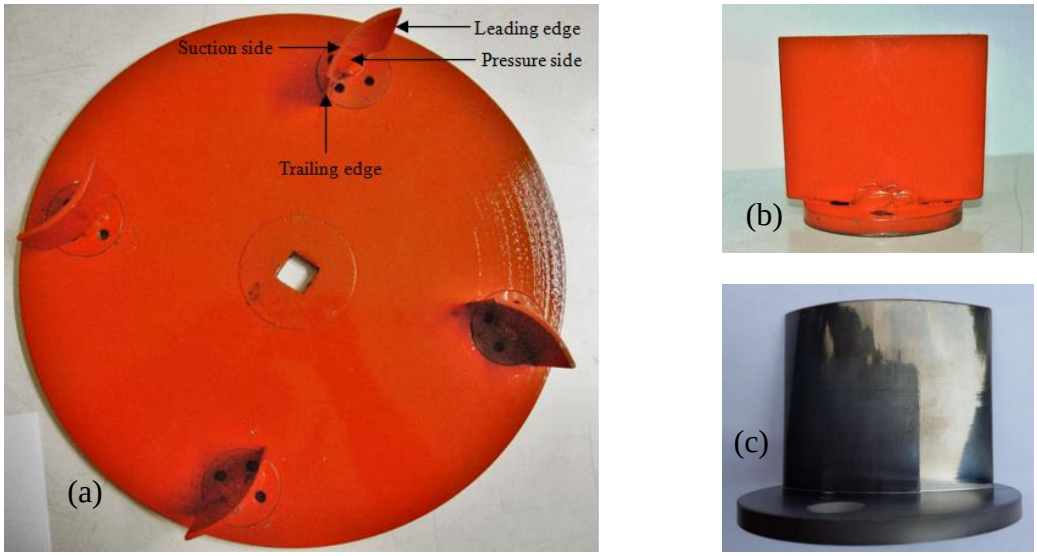

Figure 3-3: (a) Specimen blade arrangement on disc, (b) Painted test blade and (c) Tungsten carbide coated blade

Mild steel is used to fabricate the specimen blades. For erosion testing, the test specimens are labelled with numbers 1, 2, 3 and 4 and, are attached to the rotating disc as illustrated in Figure 3-3.

3.2.2. Test specimen at KMOU

Ten numbers of test specimens' blades of the optimized CFT-T15 model were selected for the erosion study. The pure metallic specimens used for the tests are tabulated in Table 3.3. High-Velocity Oxy-Fuel (HVOF) sprayed tungsten carbide (WC) coatings were applied to all the blade surfaces to achieve a surface hardness of HV 1,000 and above.

Table 3.3: Test specimen materials

Materials	**Materials with coatings**
SUS 304	WC Coatings
SUS440C	WC Coatings
SUS630	WC Coatings
SCM440	WC Coatings
STD11	WC Coatings

Table 3.4: Mechanical properties of test specimens

Material	Yield stress (N/mm^2)	Tensile stress (N/mm^2)	Hardness			Classification
			HBW	HRBS	HV	
SUS304	>205	>520	<187	<90	<200	Austenitic
SUS440C		590 - 930			>568	Martensitic
SUS630	>725	>930	>277	>28		Precipitation hardening
SCM440		689 - 897	217 - 235	18 - 22		Chromium-molybdenum
STD11	1000 - 1380	1200 - 1590	341			Tool steel

The properties related to composition were not provided by the supplier, thus the weight loss measurement method was applied to compare the erosion rates. The mechanical properties of the specimens are tabulated in Table 3.4.

3.3. Test Procedure

The main aim of the experiment was to carry out the sediment erosion test in turbine blades to observe erosion patterns and the rate of erosion. The test begins with weighing and clamping the test specimen blades on the disc. The disc was mounted on the shaft and was tightened with a pair of lock nuts and clamp pins. After the cover was firm, a mixture of water and sand was filled in the test chamber.

For the experiment at TTL, sediment samples were collected from the site i.e. Chauri Khola V Micro hydro power plant (MHP). The test specimens were exposed to a high sediment concentration of 127000 ppm which requires 650 gm of sand in a single run. For the experiment, sediment size between 150 to 200 µm was screened using mesh sizes of 150 and 200 µm [90]. The experiment was performed for a total of 3.5 hours; each interval was set to 30 minutes. After each test, the cover was removed and the test samples were cleaned thoroughly and dried. The photographs of the specimens were taken after each experiment in order to analyze wear patterns.

For the experiment at KMOU, the same sediment samples from the Chauri Khola (V) MHP were used. The test specimens made from the same materials were attached to the

rotating disc in radial directions. The test was performed for a total of 600 minutes with sediment size ranging from 75 to 250 µm. The specimens after the test were dried and weighted using an electronic balance of 0.0001 g precision to obtain material removal rate.

3.4. Result and Discussions

3.4.1. Experiment at TTL

A series of experiments were completed at TTL and pictures of all blades were taken after each test as depicted in Figure 3-4.

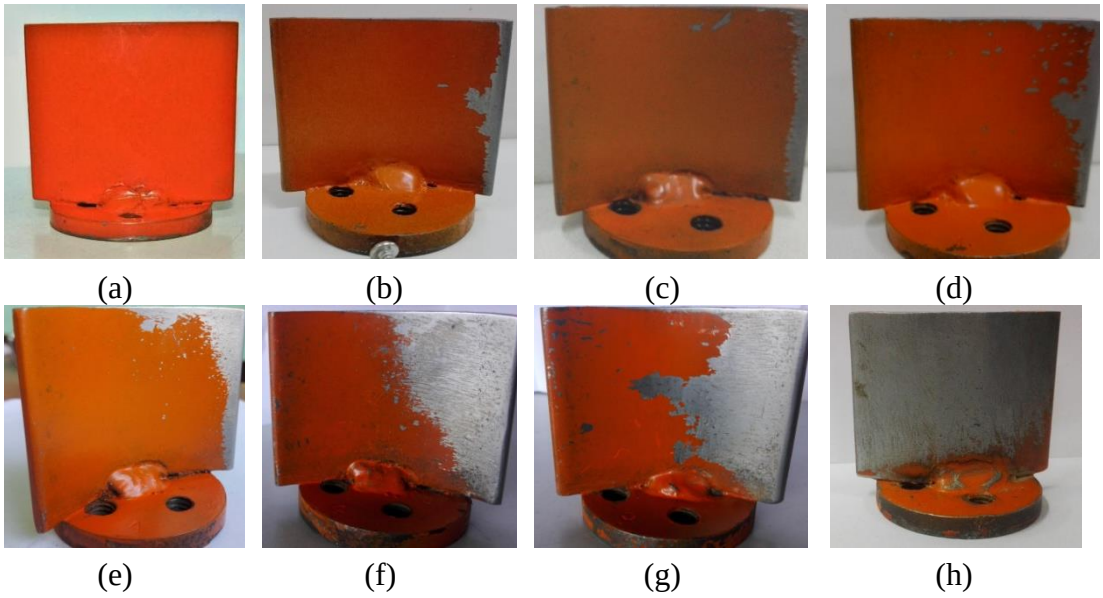

Figure 3-4: Photographs of wear patter observed (a) 0 hr., (b) 0.5 hr., (c) 1 hr., (d) 1.5 hr., (e) 2 hr., (f) 2.5 hr. (g) 3 hr. and (h) 3.5 hr.

Figure 3-4(a) shows the painted blade specimen before the test and from Figure (b) to (h) exhibit the wear pattern. In Figures (b) and (c), it can be clearly seen that paint at the edge is scratched which may be due to secondary flow vortex erosion. It can be caused by obstacles in the flow field or secondary flow in the leading edge of the blade and secondary flow is generated around the blade. The wear pattern observed in the numerical investigation had similar results as observed. The removal of paint at the backside of the trailing edge from Figures (f) and (h) has been significantly increased.

It should be the result of micro erosion as sand particles moving at high velocity creates rotational motion to these particles causing several scratches in the direction of flow. In Figures (d), (e) and (g), it is seen that the elimination of paint started from the upper end of the leading edge and continued toward the trailing edge. When the tester starts, water strikes the surface of the disc and it is forced to flow circularly towards the other end. In the turbine, discs are welded on both ends of the blade. The secondary flow gets generated from both ends. Then wear would occur in similar fashion along the width of the leading edge.

3.4.2. Experiment at KMOU

The observed data of material removed during 600 minutes of operation is enumerated in Table 3.5 [104].

Table 3.5: Average Weight of specimens after every 100 minutes of the test run

Run Time (min)	**SUS304**	**WC-SUS 304**	**SUS 440C**	**WC-SUS 440C**	**SUS 630**	**WC-SUS 630**	**SCM 440**	**WC-SCM 440**	**STD11**	**WC-STD 11**
0	203.126	201.954	198.024	198.050	197.959	201.131	192.750	193.894	192.795	192.289
100	202.997	201.877	197.923	197.986	197.901	201.083	192.716	193.853	192.758	192.249
200	202.821	201.804	197.826	197.918	197.847	201.034	192.672	193.818	192.721	192.214
300	202.670	201.729	197.735	197.856	197.797	200.993	192.636	193.777	192.681	192.184
400	202.513	201.658	197.641	197.798	197.741	200.948	192.596	193.740	192.643	192.146
500	202.363	201.579	197.534	197.738	197.693	200.910	192.554	193.709	192.607	192.118
600	202.208	201.504	197.430	197.684	197.641	200.873	192.516	193.678	192.573	192.085
Total weight loss (g)	0.918	0.45	0.594	0.366	0.318	0.258	0.234	0.216	0.222	0.204

The variation in the erosion in the successive tests on the same specimen is estimated by calculating cumulative erosion (Eq. 3.1).

$$\text{Cumulative erosion, } e_c = \frac{w_i - w_j}{w_i}\ 1000 \qquad (3.1)$$

Where w_i is the weight of test specimen before the experiment (g); w_j is the weight of test specimen after test (g)

The cumulative erosion of each test specimen for a total runtime of 600 minutes is plotted in Figure 3-5.

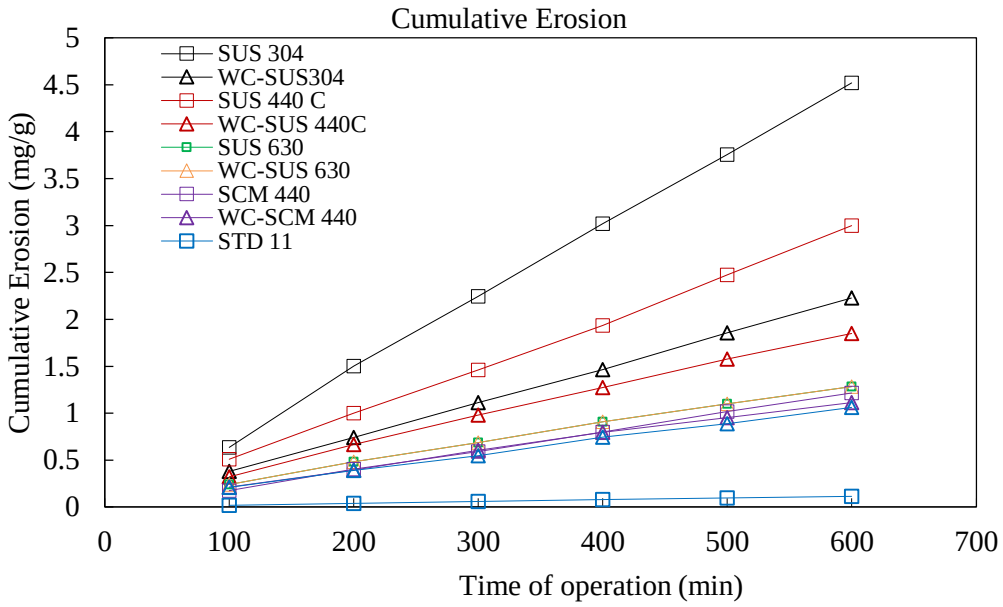

Figure 3-5: Test specimens before the test and after 600 minutes.

Similarly, the erosion rate is the amount of material eroded from the specimen per unit of time and is calculated using Eq. 3.2.

$$e_r = \frac{(W_1 - W_2)}{W_1 \times \Delta t} \times 1000 \quad \frac{mg}{g} perhour \tag{3.2}$$

Where W_1 is the weight of specimen before testing (g); W_2 is the weight of specimen after testing (g) and Δt is the total exposure time (hr.)

The amount of erosion of each test specimen is plotted in Figure 3-6. The amount of erosion of SUS 304 is found to be considerably higher during the first run of 100 minutes. The higher value followed by declined steady value may be due to wear of the shaft seal that resulted in a leakage flow of mixture from slurry chamber to the cooling chamber. The study witnessed the traces of the sediment particles flowing through the outlet of the water-cooling chamber of the RDA. Also, the sand used might get deteriorated and the shape of the erodent becomes smoother after striking the test specimens and baffles continuously, thereby reducing the erosion rate with prolonged duration of tests. However, it can be observed that the amount of erosion is increased with an increase in the time of operation for all the experiments.

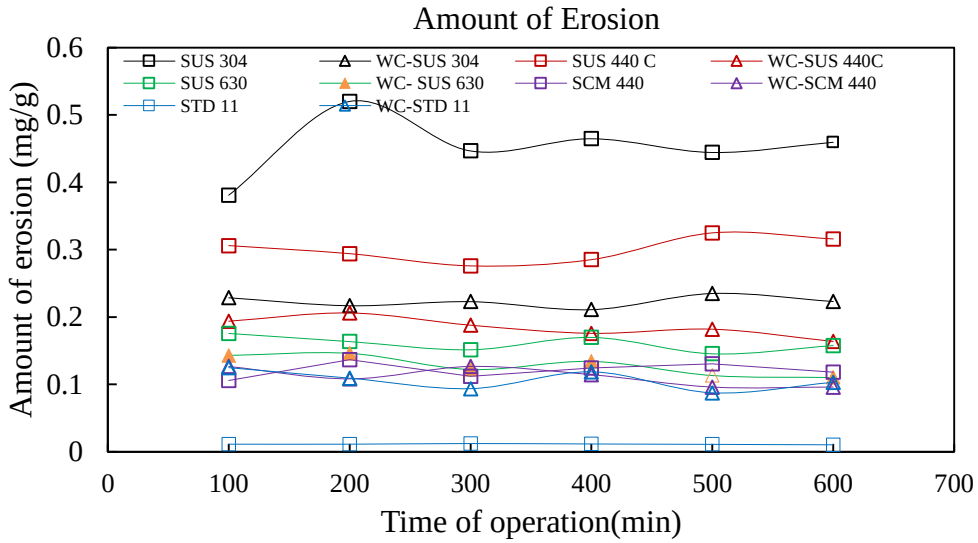

Figure 3-6: Amount of Erosion after each 100 min interval

The erosion comparisons are classified into three categories to study relative erosion resistance of different materials specimen that is exposed to similar operating conditions. Firstly, the parent uncoated- specimens are compared among themselves. The coated specimens are compared among themselves in the second stage. Lastly, the uncoated specimens are compared to coated specimens.

A similar erratic type of erosion pattern was observed in RDA experimental study performed by Park et al. [105] and Rajkarnikar et al. [89]. Figure 3-7 below shows the amount of erosion in the test specimen for each test run.

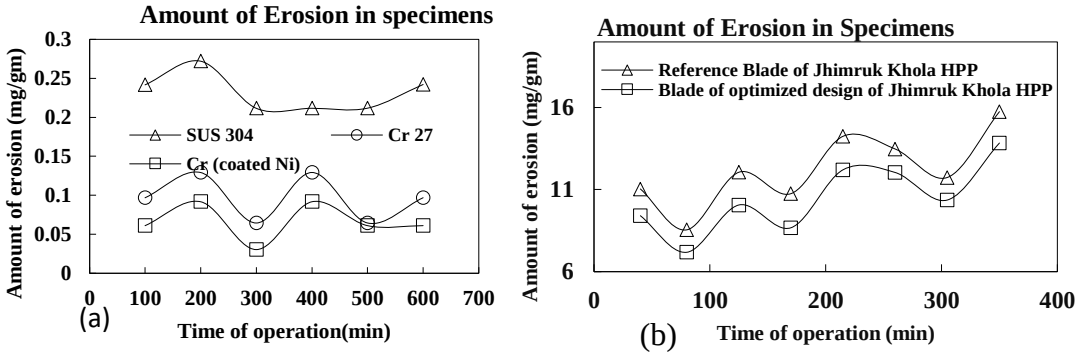

Figure 3-7: Experimental observation on RDA by (a) Park et al. [105] and (b) Rajkarnikar et al. [89]

3.4.2.1. Comparison of non-coated specimens:

It can be observed that the weights of all non-coated test specimens are decreasing linearly after every test runtime. The amount of material loss on all the test specimens is almost the same after a test run of 100 minutes each for a total runtime of 600 minutes. The cumulative erosion is found to decrease with an increase in tensile stress and hardness value of test specimen material. The ranking of the material based on maximum cumulative erosion from high to low are SUS 304 > SUS440C > SUS630 > SCM440 > STD11 with the highest amount of erosion value of 4.52 mg/g in SUS 304 and the lowest amount of erosion value of 1.1 mg/g in STD11. The impingement of the sediment particles at a low angle has resulted in a higher value of material loss in comparison to the softer materials (in terms of hardness) by the action of shear and micro-cutting.

3.4.2.2. Comparison of coated specimens

The coatings applied on five different materials were compared for their erosion resistance in RDA for 600 minutes of exposure to slurry mixture. From Fig. 4, it can be seen that the total cumulative erosion in all the test specimens is in an increasing trend and followed a linear trend. The tungsten carbide coating (WC) on the surface of blades improved sediment resistive properties. The ranking of the material based on weight loss measurement from high to low are WC SUS 304 >WC SUS440C > WC SUS630 > WC SCM440 > WC STD11 with the highest material removal loss of 0.45 mg in WC SUS 304 and lowest removal rate of 0.204 mg in WC STD11. In the case of hydro turbines, the WC coatings are not polished after they are applied by spraying technique because it is a costly process. The rough surface resulted after coatings are thus removed by more of the ploughing action as compared to micro-cutting action at a lower impingement angle.

3.4.2.3. Comparison of non-coated specimens with coated specimens:

The erosion resistance of the coatings is found to be more erosion resistive than un-coated pure metallic specimens. From Table 6, it can be observed that the amount of

erosion is reduced by 50 % in SUS 304 and 45 % in SUS 440C after coating. While in the case of SUS 630 and WC-SUS 630, there is a negligible difference in erosion rate over the entire test run. Similarly, a marginal variation in erosion among SCM 440 and WC- SCM 440 is reported. The coatings can wear easily if penetrated by the impacting particles upon interference with the coating and the metallic surface. The coated specimens may have a high erosion rate as the particle impact cause initial wear and then followed by accelerated wear of coatings from that particular location of impact. Such a phenomenon might have occurred in the case of STD11 where the amount of erosion is found to be lower than that of coated STD11. The surface roughness value of the coated surface also plays a role in localized removal of the material and detachment of the coatings as reported by Zahavi and Schmitt [106] The roughness of the coatings depends on powder properties and spray parameters such as particle size, temperature, and velocity of spray.

3.5. Numerical study of turbine and RDA

The numerical analysis was carried out to investigate the flow field in a CFT turbine and RDA. The generation of the fluid domain of CFT and RDA was done in CATIA V5 (Student Version) and the structured hex mesh was created (See Figure 3-8). The mesh dependence study was carried out for both domains. SST turbulence model was chosen as it can predict field flow in both of the above-mentioned cases, RDA and CFT, with better precision and less time consumption [107] [108].

The flow inlet and exit boundary conditions are used in CFT where a no-slip wall is defined at stationary (a pipe, diffuser, stator up and stator down) and rotating (runner) components of the domain. The mass flow inlet is defined at the pipe and the average static pressure exit is defined at stator down.

Since the RDA is an enclosed type domain, normal boundary conditions cannot be applied. The domain is filled with a mixture of sediment and water and a no-slip wall is defined at stationary (stator with fins) and rotating (rotor with attached blade) components.

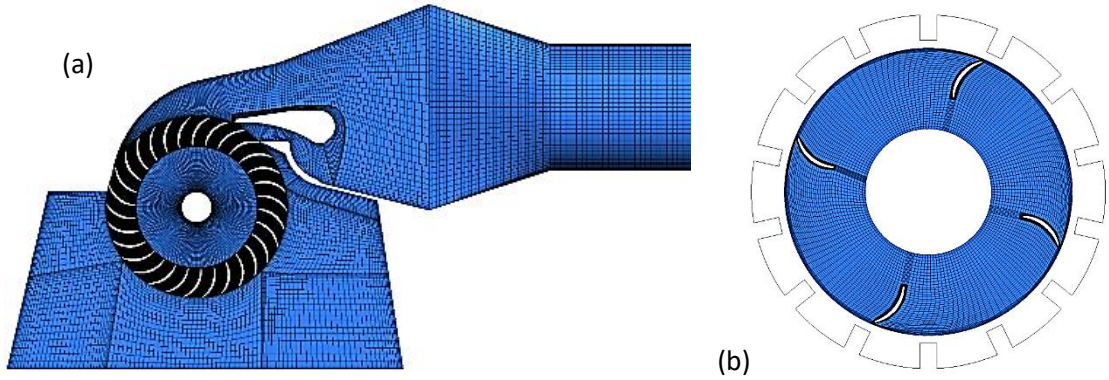

Figure 3-8: ICEM hex mesh of (a) CFT (b) RDA.

General Grid Interface (GCI) was checked so that there is a smoother transition between the domains and to estimate the discretization error [109]. Three different mesh was created as Coarse, Medium and Fine. The number of elements at each edge in a 3-D surrounding block of geometry was increased by 1.5x. For the uncertainty measurement clearance gaps were not introduced. Discretization error for the numerical was determined as follows:

i) The average length of each element for a 3-D mesh was determined as,

$$h = \left[\frac{1}{N} \sum_{i=1}^{N} (\Delta V_i) \right]^{1/3} \tag{3.3}$$

ii) Let $h_1 < h_2 < h_3$ and $r_{21} = h_2 / h_1, r_{32} = h_3 / h_2$,the apparent order, was solved as in Eq. 3.8, 3.9 and 3.10 using fixed-point iteration method,

$$p = \frac{1}{\ln(r_{21})} \left| \ln \left| \varepsilon_{32} / \varepsilon_{21} \right| + q(p) \right| \tag{3.4}$$

$$q(p) = \ln \left(\frac{r_{21}^{p} - s}{r_{32}^{p} - s} \right) \tag{3.5}$$

$$s = 1 sign(\varepsilon_{32} / \varepsilon_{21}) \tag{3.6}$$

iii) The extrapolated values were calculated as,

$$\phi_{ext}^{21} = (r_{21}^{p}\phi_1 - \phi_2)/(r_{21}^{p} - 1) \quad (3.7)$$

Approximate and extrapolated relative error was calculated as,

$$e_a^{21} = \left|\frac{\phi_1 - \phi_2}{\phi_1}\right| \quad (3.8)$$

$$e_{ext}^{21} = \left|\frac{\phi_{ext}^{12} - \phi_1}{\phi_{ext}^{12}}\right| \quad (3.9)$$

$$GCI_{fine}^{21} = \frac{1.25e_a^{21}}{r_{21}^{p} - 1} \quad (3.10)$$

Three different mesh with the number of elements as shown in Table 3.6, were used to measure numerical uncertainty.

In this case, Torque acting on the blade, Pressure on the blade, Velocity at the blade and Velocity at the trailing edge of the blade were considered parameters for measuring the uncertainty. Uncertainty in the torque measurement from medium mesh to fine mesh was found to be 0.1892 %. Moreover, in the case of pressure measurement at the blade, the uncertainty in measurement was 0.3115 %. Similarly, with velocity as a measurement parameter, the uncertainty values for the velocity on the blade and velocity at the trailing edge were 0.0676 % and 0.1819 % respectively. Overall, the uncertainty measurements for the selected parameters were less than 0.5 % which gives good agreement for numerical investigation of desired parameters with the selected model.

Table 3.6: Discretization error for numerical study of RDA

Measurement Parameters (ϕ)	**Coarse**	**Medium**	**Fine**	**Extrapolated parameters (ϕ_{ext}^{21})**	**Approximate Error (e_a^{21})**	GCI_{fine}^{21} **(%)**
Torque on blade (N-m)	46.943	47.69	42.954	46.872	0.0159	0.1892
Pressure on blade (Pa)	134440	135225	133170	134100	0.0058	0.3115
Velocity on blade (ms^{-1})	1.015	1.012	1.023	1.015	0.0027	0.0676
Velocity at trailing edge (ms^{-1})	6.817	6.854	6.952	6.8071	0.0054	0.1819

Figure 3-9 shows the velocity plot of CFT and RDA. It can be observed that the water flows with a similar velocity pattern, entering the leading edge on the pressure side and suction side of the blade. Similarly, the water flow vector in CFT and RDA exhibits an identical flow pattern along the blade and at the trailing edge. The entrained water flow in between the blades of the CFT can be observed whereas flow separation takes place intermittently in RDA. Further in RDA, a vortex is created in between two specimens clamped as can be seen in Figure 3.8 (b). It may have occurred due to the fact that, for the same outside diameter, the runner of CFT is equipped with 30 numbers of blades while only 4 numbers of the test specimens are clamped on the rotating disc of RDA. Further, the runner of the CFT rotates when water strikes the leading edge of the blades of the runner while in RDA; the test blade is rotated with a motor connected with the shaft. . It can be seen that the pressure at the inlet and outlet of the blades for CFT and RDA is almost identical.

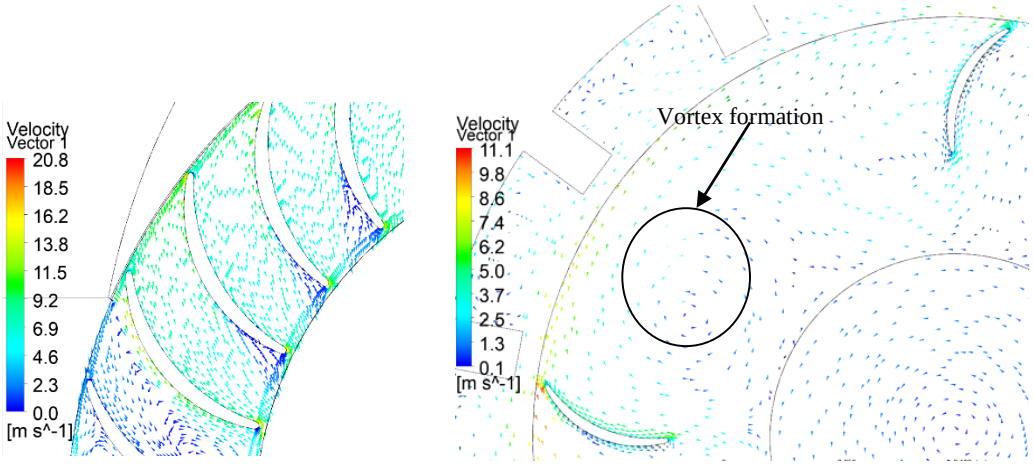

(a) (b)

Figure 3-9: Velocity distributions in (a) CFT and (b) RDA

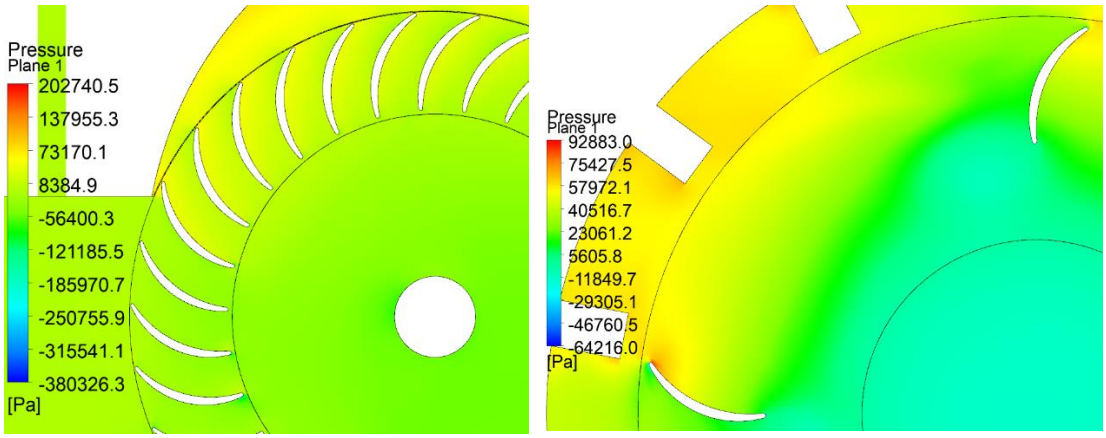

(a) (b)

Figure 3-10: Pressure distributions in (a) CFT and (b) RDA.

This chapter focuses on the applicability of the RDA to estimate the erosion resistive behavior of different materials and tungsten carbide coatings on them. At the operation rpm of 720, the pure metallic specimen along with paints and WC coatings made from different materials was exposed to a high sediment concentration of 127000 ppm to observe rapid erosion results.

i. The erosion resistance of STD11 was found to be highest than that of other materials. It can be concluded that the mechanical properties of the materials have a significant influence on erosion resistivity. The high erosion resistance of STD 11 is due to the dependence of erosion rate on the hardness value, ductility, and tensile stress.

ii. The tungsten carbide coatings on the different materials have been found to enhance the erosion resistance properties to some extent. However, the penetration of sediment particles on coatings erodes it more easily and at an accelerated rate. It can be concluded that the coatings can be suitable for low head turbines or perform better in low-velocity operations.

iii. Although RDA yields result in comparatively less time, the hydraulics of flow in CFT and RDA is found to be different examined in terms of vortex formation in RDA, with numerical analysis and results obtained using RDA might be misleading.

CHAPTER 4: NUMERICAL ANALYSIS ON CFT

Computational models for computing and analyzing fluid flow in CFD with mesh generation, boundary conditions, turbulence models and validation have been discussed in this chapter.

CFD analysis was carried out using ANSYS CFX 13.0 in order to determine the flow behavior, erosion rate density and the performance of the runner. A close investigation on the pressure and velocity distribution, efficiency and erosion rate density were observed for different inlet blade angles at different flow conditions and different rotational speeds.

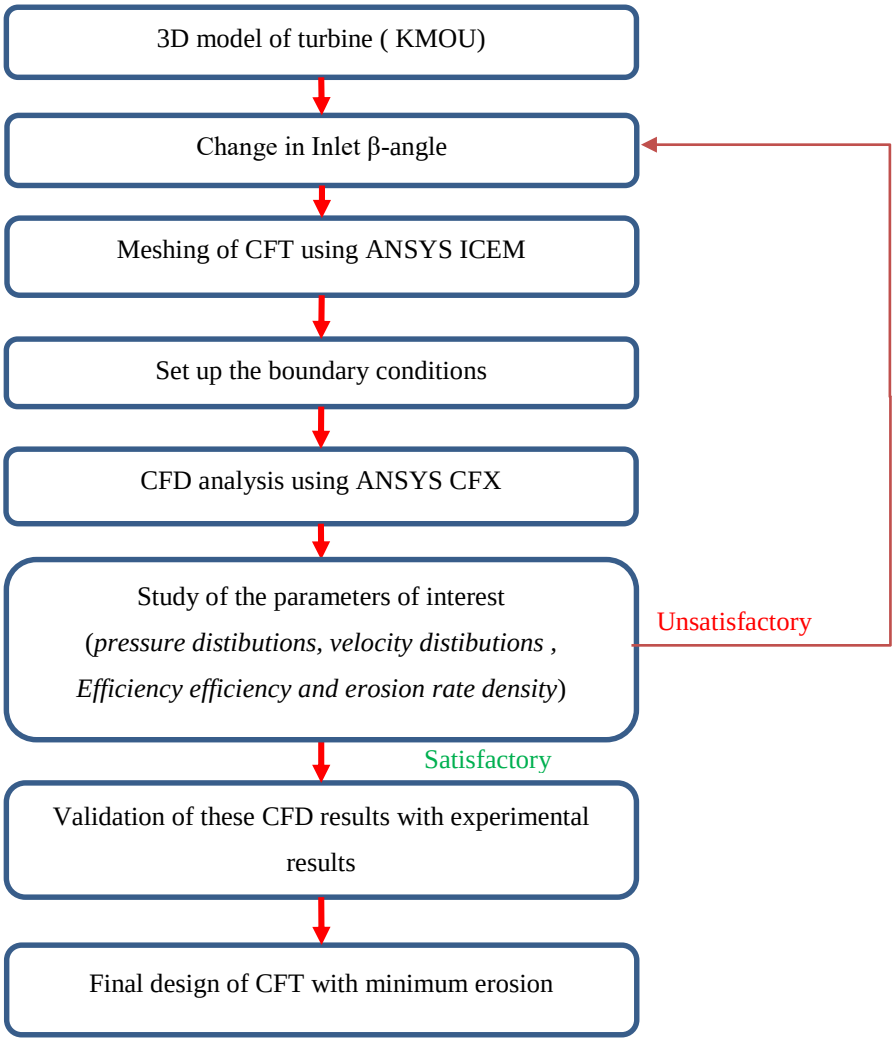

Figure 4-1: Numerical Analysis Methodology

4.1. Geometry Generation

The numerical domain of this CFT is composed of three components: nozzle, Runner and diffuser. The turbine drawings were based on KMOU-model and 3D domain modelling was carried out in the CATIAV5 student version. The runner is composed of 30 number of blades with an outside diameter of 336 mm and a diameter ratio of 0.668. Four different cases are formulated by changing inlet blade angle β as 16^0, 18.42^0, 30^0, 36^0 while keeping the nozzle, guide vane and casing the same for all of the cases.

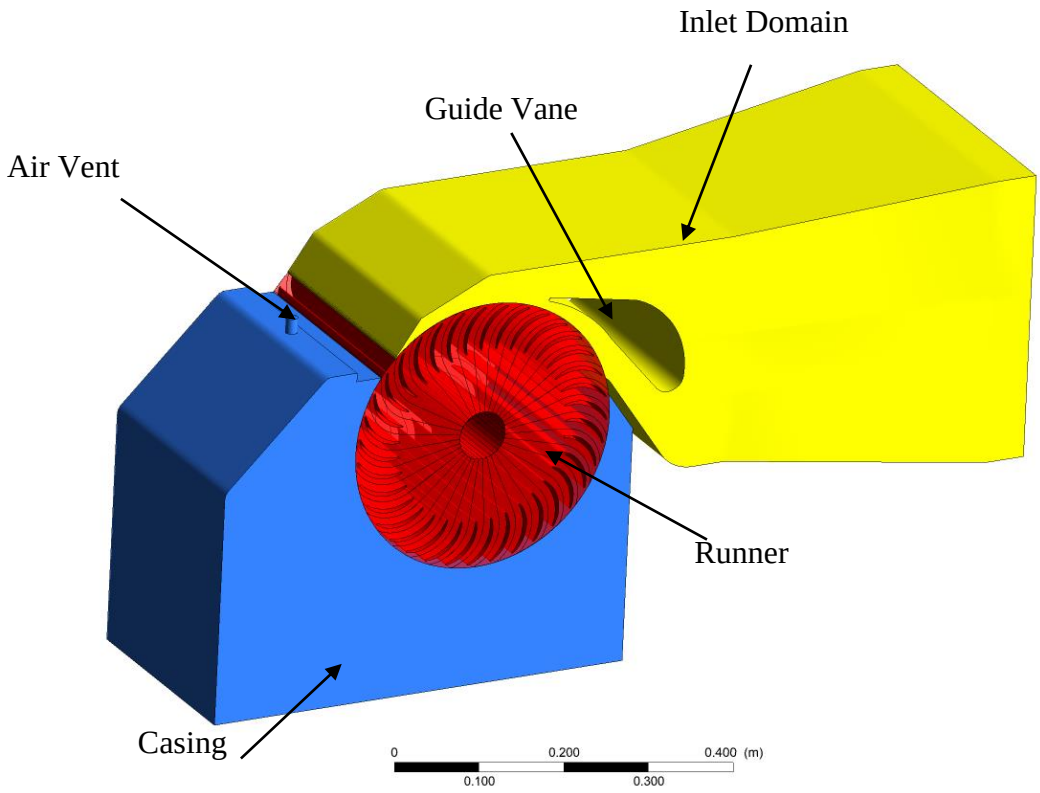

Figure 4-2: Domain for CFD

4.2. Mesh Generation

The meshing of all the components was carried out in ANSYS ICEM so as to generate a structured hexahedral mesh which is more efficient than tetrahedral in terms of accuracy, CPU solving time and memory allocation.

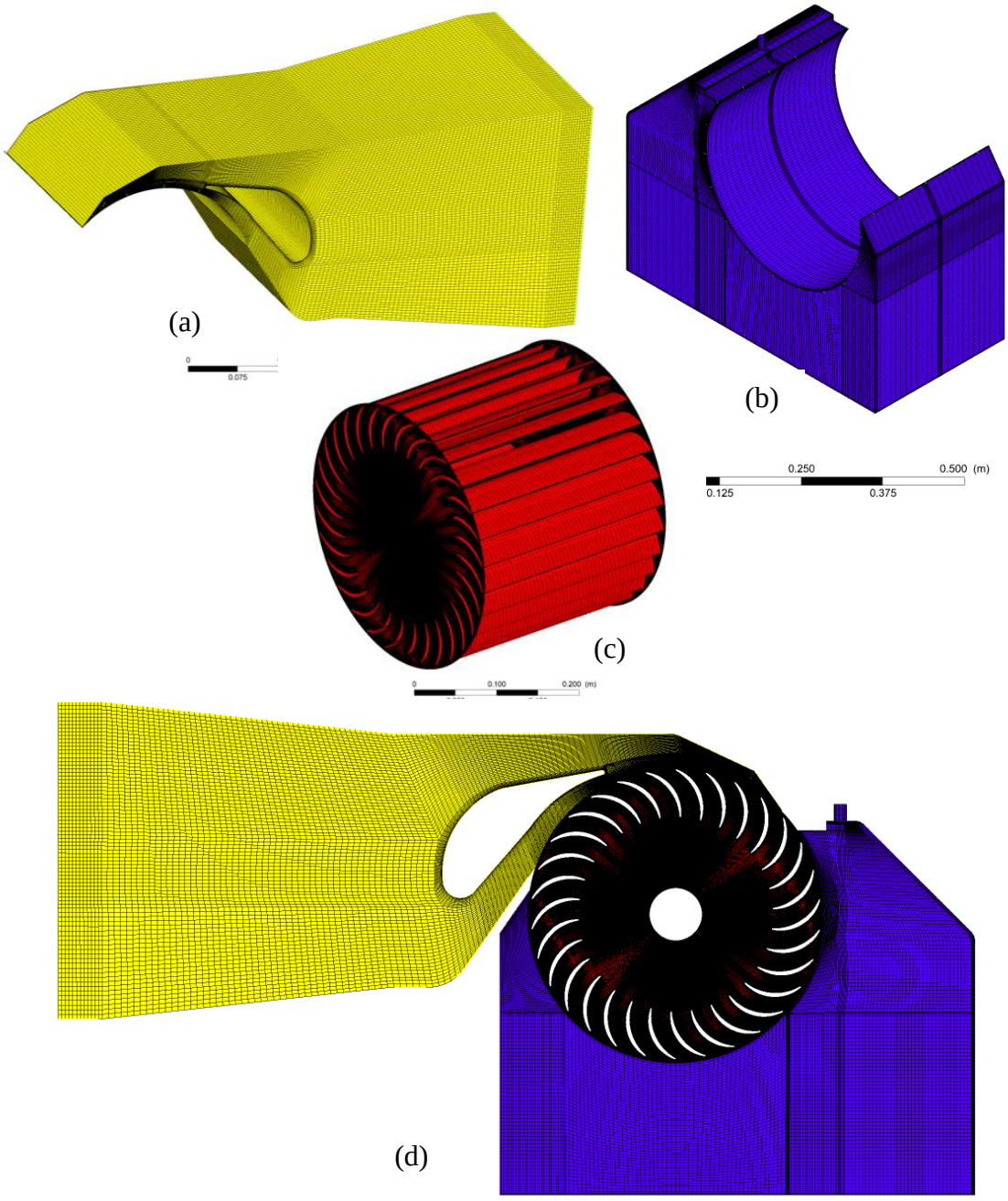

Figure 4-3: ICEM meshing in (a) Nozzle (b) Diffuser (c) Runner and (d) CFT components assembled

Meshing was carried out on nozzle, runner and casing separately. For acceptance minimum mesh quality for simulation is 0.3 and for each and every case the mesh

quality was maintained higher than 0.3 with a minimum element face angle greater than 18^0.

Thirteen different mesh from coarse to fine was created to conduct separate mesh independence tests (MIT) for the nozzle, runner and casing with Values of 50 for each of the mesh.

For the nozzle, a first coarse mesh is produced maintaining a Y+ value of 50. While maintaining the same Y+ value, mesh size is gradually increased and simulation is performed. Through series of simulations, a mesh of 760,444 number of elements for the nozzle is selected as the velocity and mesh fluctuation percentage is well below 1 %.

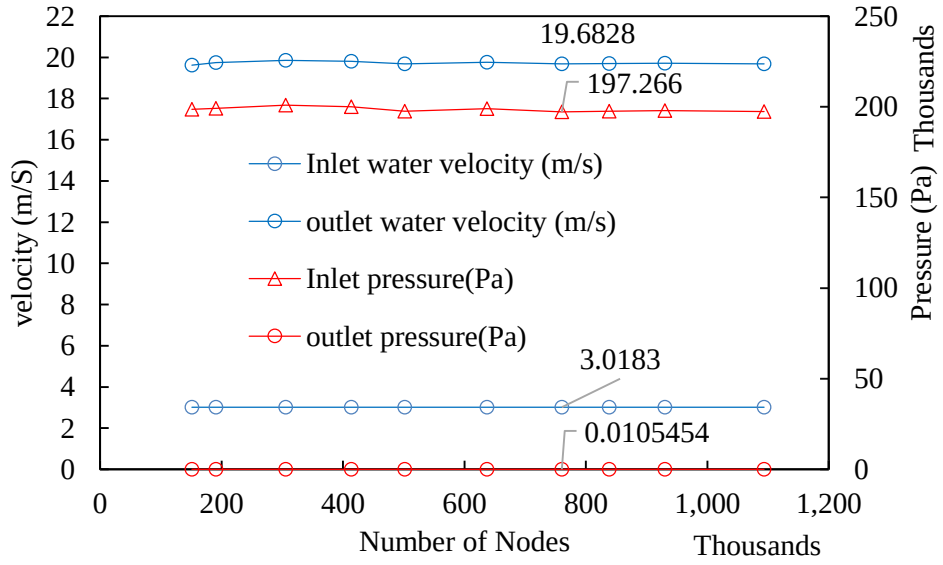

Figure 4-4: MIT of Nozzle

Similarly, for the casing/diffuser mesh of 691,481 number of elements is selected as the velocity fluctuation is within the range of 1 %.

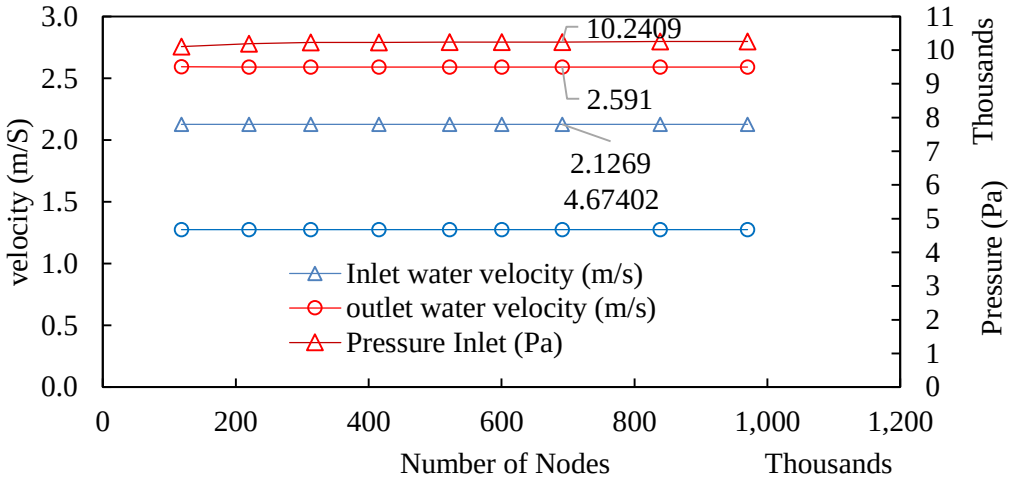

Figure 4-5: MIT of diffuser

Finally, for the runner the mesh with 7,626,360 elements was selected as the fluctuation in torque is within 2 %.

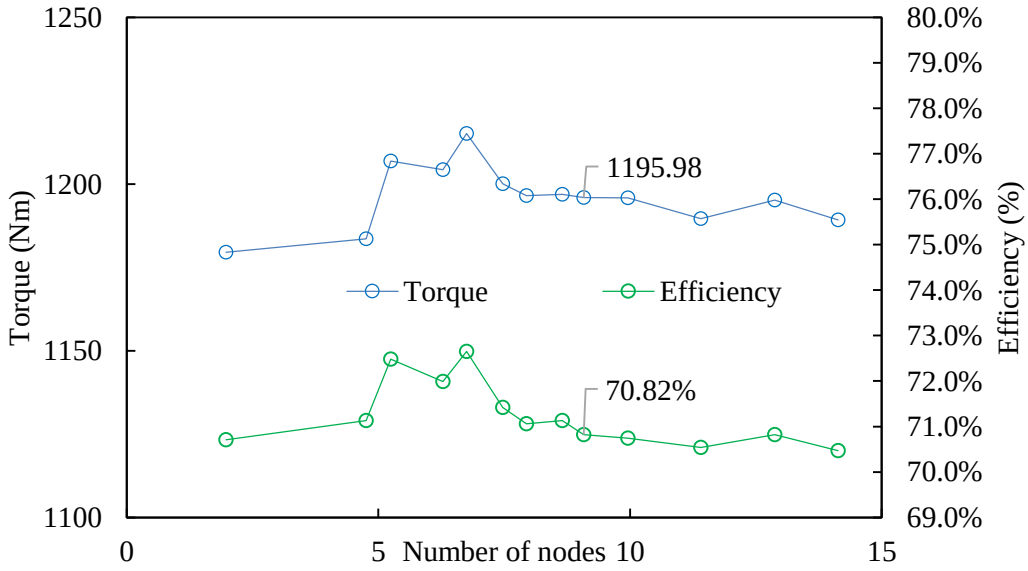

Figure 4-6: MIT of CFT

After the mesh independence test, GCI was checked so that there is a smoother transition between the domains. Three different mesh with the number of elements as shown in Table 4.1, were used to measure numerical uncertainty.

In this case, Torque acting on the runner and water outlet velocity from the nozzle were chosen as the independent variable for GCI estimation. Uncertainty in the torque measurement from medium mesh to fine mesh was found to be 0.7704 %. Moreover, in the case of velocity measurement at the outlet of the nozzle the uncertainty in measurement was 0.0281 %. For the GCI estimation in the case of dependent variables efficiency and net head measured on the nozzle were chosen parameters. In this case, the uncertainties were estimated to be 0.3586 % and 0.0039 % respectively. Overall, the uncertainty measurements for the selected parameters were less than 1 % which gives good agreement for numerical investigation of desired parameters with the selected model.

Table 4.1: Discretization error for the numerical study of CFT

Measurement Parameters (ϕ)	**Coarse**	**Medium**	**Fine**	**Extrapolated parameters (ϕ_{ext}^{21})**	**Approximate Error (e_a^{21})**	GCI_{fine}^{21} **(%)**
Efficiency (%)	70.47	70.59	70.71	70.27	0.0017	0.3586
Torque on runner (N-m)	1189.23	1200.38	1179.53	1181.90	0.0094	0.7704
Net head on nozzle (m)	20.30	20.15	20.17	20.17	0.001	0.0039
Water outlet velocity from nozzle (ms^{-1})	19.6305	19.712	19.6866	6.8071	19.6822	0.0281

4.3. Turbulence Models

There are various types of turbulence models available in ANSYS CFX, however, the selection of a suitable model is very important. The k-ε model is good for the free stream region while k-ω is very good at viscous sublayer but very sensitive in free stream region calculations [45]. Hence, looking at these limitations SST turbulence model is selected which act as k-ε near a free stream and k-ω near a viscous sublayer. For the initial condition, the k-ε turbulence model was used and later on after comparison between k-ε and SST, the SST model was selected.

4.4. Boundary Conditions

Steady-state type setting with no slip viscous condition was applied. The inlet condition was taken as the mass flow and static pressure was taken as outlet condition with a variety of mass flow rates while outlet pressure was set to 1 atm. Nozzle and diffuser/casing were taken as stationary domain and runners as a rotational domain. The rotational speed of the runner was varied from 150 rpm to 950 rpm with a gradual increment of 100 rpm. The sediment of sizes of range 75 microns to 250 micros with an interval of 25 microns and concentration of 3000 ppm with a shape factor of 0.68 [103] was used.

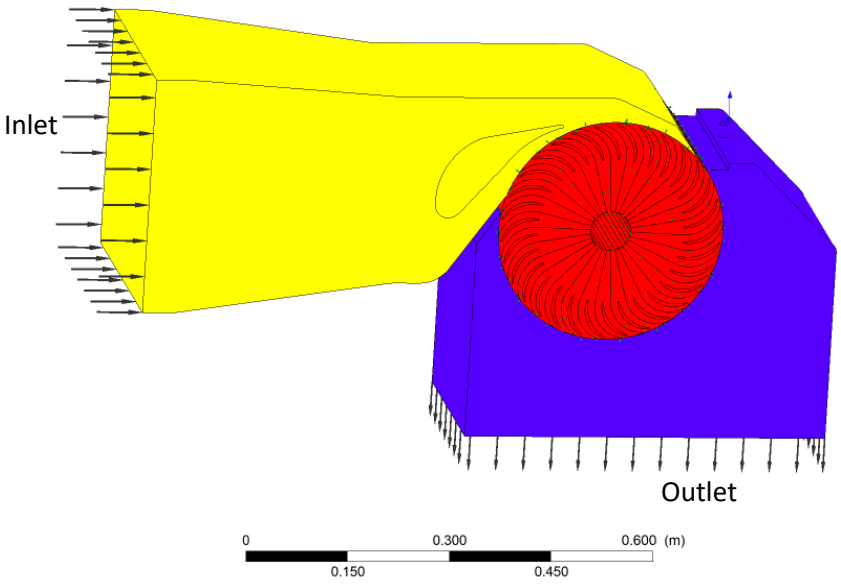

Figure 4-7: Boundary condition of CFT

4.5. CFD Analysis

Numerical analyses were performed on Crossflow turbines, designed with the different beta distributions. The performance of the runners and their sediment erosion resistivity were evaluated numerically according to the methods discussed in chapter 4. The results obtained from CFD analysis have been represented graphically to analyze the performance of the turbines. The blade angle at the inlet was changed, keeping the outlet

blade angle equal to 90^0. Optimum blade angles have been selected for further studies, based on the performance and sediment erosion rate density.

4.5.1. Number of Blades

A number of blades play an important role in both the efficiency and sediment erosion of the turbine. In order to determine the optimal number of blades for best performance in terms of both sediment erosion and efficiency, numerical simulations were performed on turbines with 20, 25, 30, 40 and 45 number of blades. All the boundary conditions were kept constant for all the simulations. The results of simulations showed that the efficiency increased upon increasing the number of blades up to 35 and started decreasing once the number was increased more than that. This could be because of the optimal flow passage created between the blades in a 30 blade runner. This can also be visualized by the flow pattern seen in the following images.

In 20 blade runner, the flow passage is relatively large, hence the water is unable to attain a higher velocity of the flow, which is required for better efficiency. Thus when the number of blades is increased, the efficiency increases until a certain point. Once the number of blades reaches its optimal value, the flow will start interfering with itself upon increasing the number of blades any further. In this study, the efficiency increased to 35 number of blades and decreased upon increasing beyond that. Similarly, the number of blades is also a factor influencing the sediment erosion of the turbine. The sediment erosion rate density is greatly dependent on the relative velocity of the sediment with respect to the runner. As discussed earlier, the velocity of the flow increases with the increase in number of blades due to decrease inflow passage area. And, the sediment erosion rate is proportional to the n^{th} power of velocity, considering all other parameters are the same. Thus, the sediment erosion increases with the increase in number of blades in a crossflow turbine. Similar results are observed from the results of CFD Analysis as well. A runner with 30 blades has been selected for further studies as it has shown maximum efficiency with average sediment erosion performance compared to other runners.

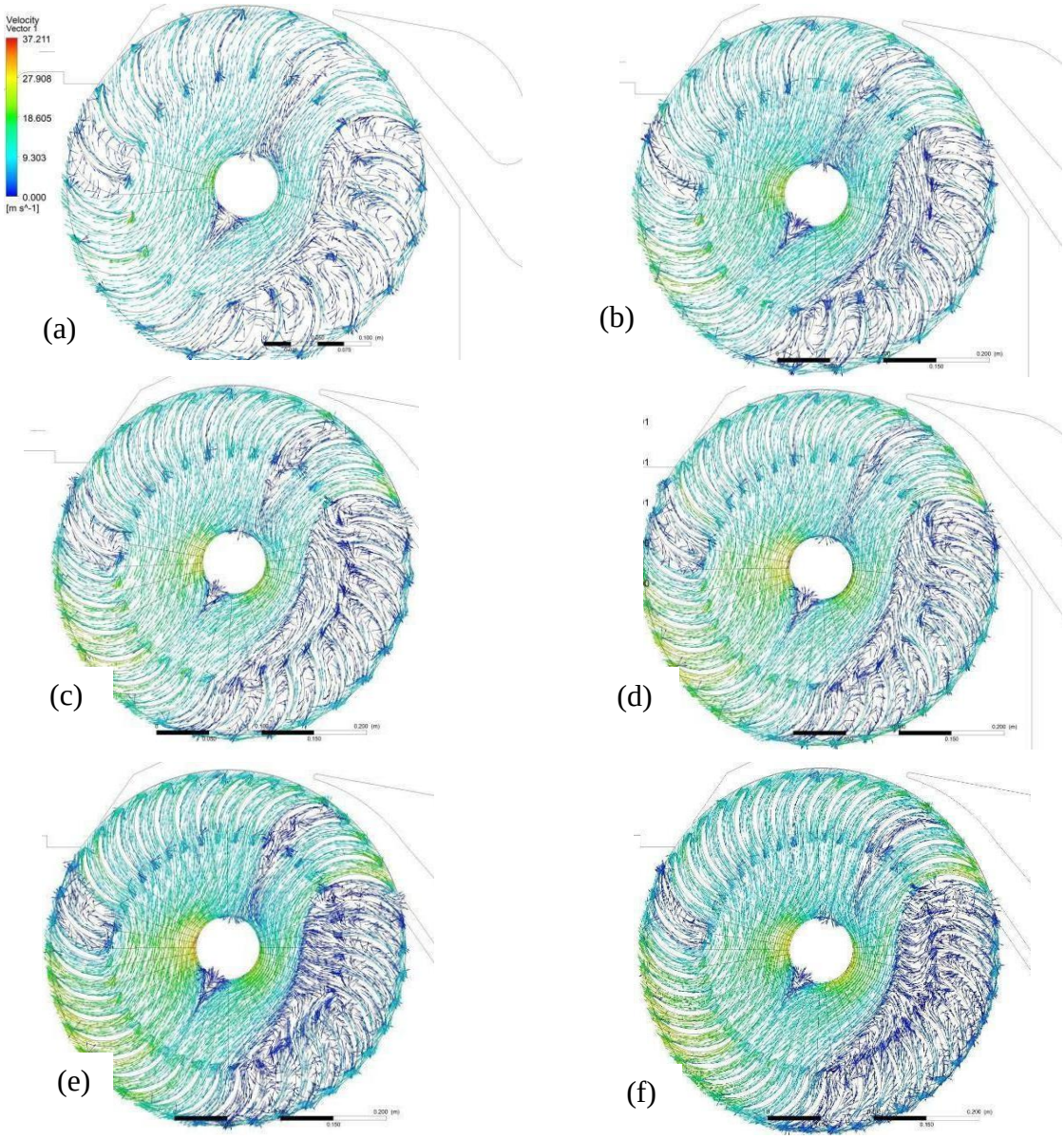

Figure 4-8: velocity vector flow in CFT with (a) 20 blades (b) 25 blades (c) 30 blades (d) 35 blades (e) 40 blades and (f) 45 blades

4.5.2. Beta Distribution

The blades of crossflow turbines are designed such that the blade camber line is an arc of a circle. The blade angle at the inlet is changed as per the requirement of the design, however, the blade is always directed towards the center of the runner, hence the blade

angle, at an outlet, is always equal to 90^0, irrespective of the blade angle at the inlet. Five different runner designs, with different blade angles, were analyzed numerically. Nine number of guide vane openings from full opening named 0^0, 2^0, 4^0, 5^0, 6^0, 8^0, 10^0, 12^0 and 14^0. Sediment erosion rate density, as well as efficiency hill diagram for the runner, have been plotted, for each design to determine the best design.

Investigating the velocity distribution on the mid-plane of the turbine for all the inlet beta angles on the same flow and same rotational speed reveals that in the first stage all of the five designs have similar velocity distribution. In the second stage, however, among all the designs, velocity for the 16^0 inlet blade angle is way less than all other designs which can be observed from Figure 4-9. Further, it is observed that the velocity for all the designs is higher on the suction side of the blade in the second stage. Many research showed that high velocity means the chance of high erosions. Hence, it is likely that the suction side of the blade is more susceptible to sediment erosion. After the close study of the velocity distribution of all the designs, a design with an inlet blade angle of 16^0 is found to be the best design that will have less sediment erosion. Moreover, it is observed that among these designs efficiency for the 16^0 is higher which may be due to a better stagnation angle in the first stage. Although, it seems like decreasing the inlet blade angle could have decreased the sediment erosion on the blade but while reducing

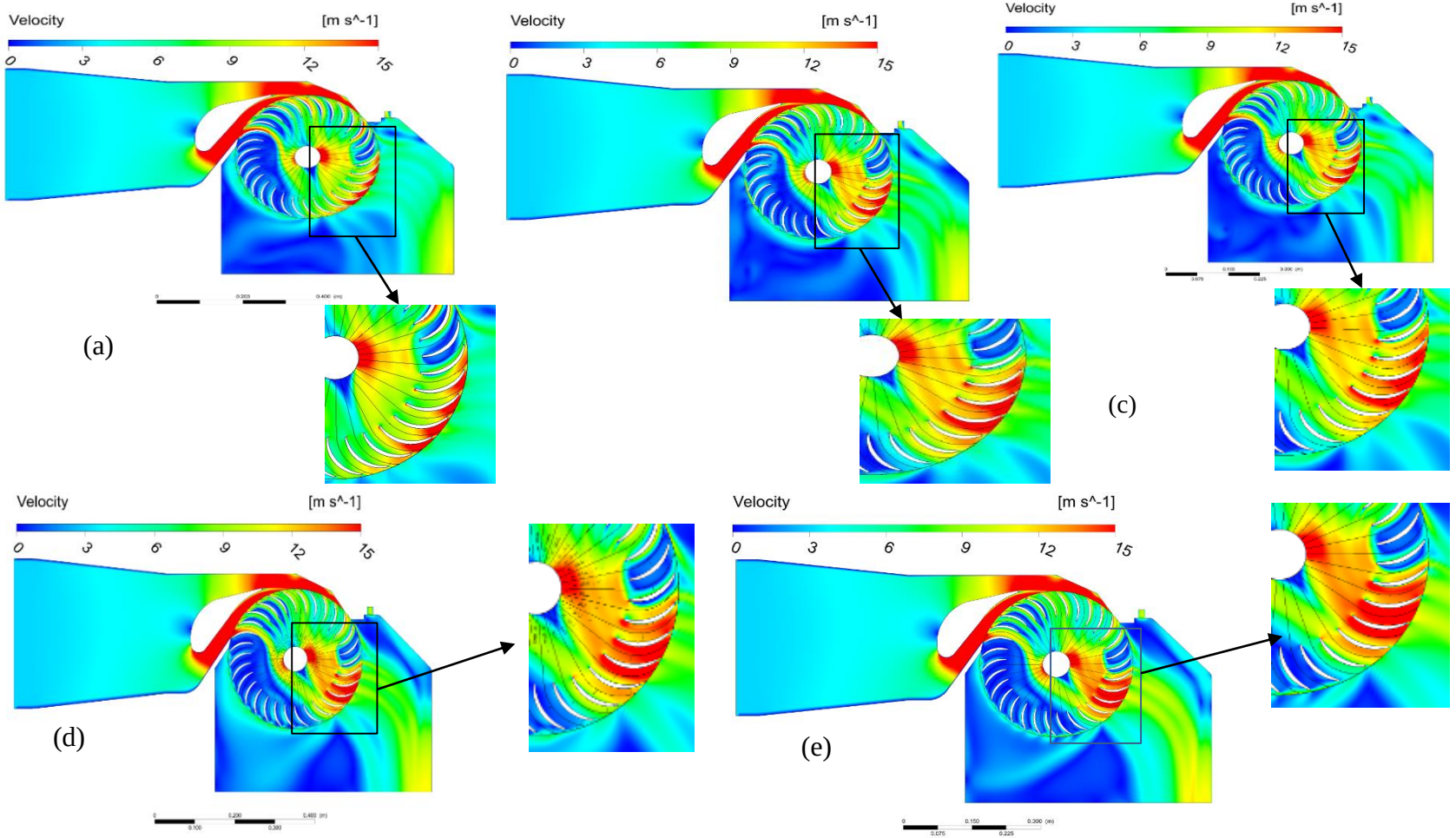

Figure 4-9: Velocity distribution at the mid plane of the turbine for inlet blade angle of (a) 16^0 (b) 18.42^0 (c) 24^0 (d) 30^0 (e) 36^0

the inlet blade angle also reduce the curvature of the blade which will lead to flow separation and eventually reduce efficiency. Therefore, an inlet blade angle of 16^0 is the best design with higher efficiency and low sediment erosion. Hill charts for all the designs have been plotted and discussed below.

4.5.2.1. Design 1 (36^0 blade angle)

The blade angle at the inlet of the blade is equal to 36^0 in the first design. At the outlet, the blade angle is equal to 90^0. The CFD Analysis of the design was performed at different rpm and flowrate keeping the head constant. The efficiency hill diagram has been plotted from the results of the simulation and is shown in Figure 4-10.

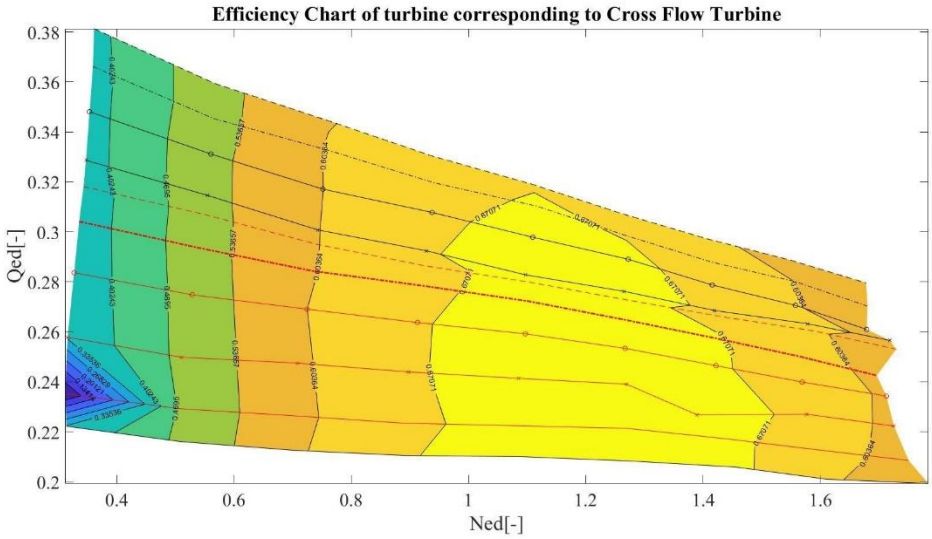

Figure 4-10: Hill chart diagram of 36^0 blade angle

Maximum efficiency of over 73 % was obtained at 12^0 guide vane opening at 750 rpm. The hill diagram shows that the turbine can be operated at 40 % to 73 % efficiency over a wide range of operating conditions. Extremely low efficiency has been obtained at low rpm and low discharge conditions, thus the operating range for design 1 is between Ned values of 0.9 and 1.5.

Similarly, the Sediment erosion rate density hill (SERD) diagram of the turbine with sediment size ranging from 75 microns to 250 microns was constructed based on the results of CFD analysis. The SERD hill diagram is in conjunction with the efficiency hill diagram, such that the sediment erosion rate density is higher at low rpm and low flow conditions, where the efficiency of the turbine was lowest. However, the minimum values of SERD were obtained at higher RPMs where the efficiency of the turbine is not the highest, which may be because the relative velocity of the water and blade is lesser at higher rpm values. As per the hill diagram, the SERD value is minimum at a small region in the hill diagram, hence the design is not selected for further studies.

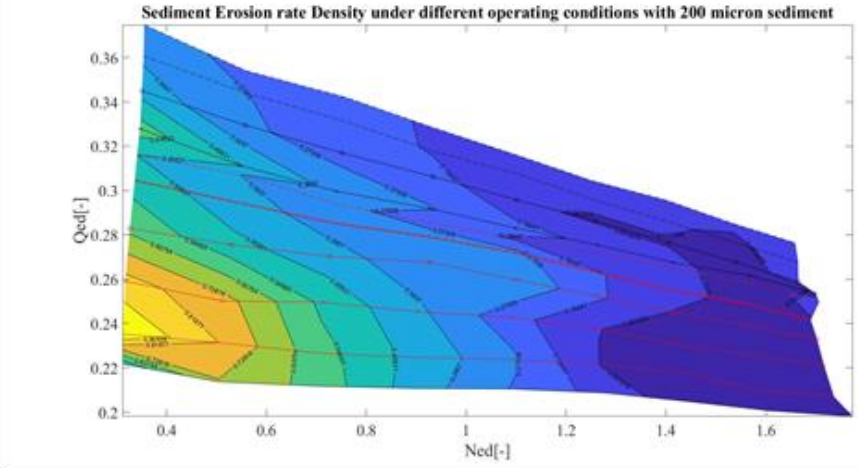

Figure 4-11 SERD Hill diagram of 36^{o} blade angle

4.5.2.2. Design 2 (30^{0} blade angle)

The blade angle at the inlet of the blade is equal to 30^{o} in the design. At the outlet, the blade angle is equal to 90^{o}. The CFD Analysis of the design was performed at different rpm and flowrate keeping the head constant. The efficiency hill diagram has been plotted from the results of the simulation and is shown in the figure below. Maximum efficiency of over 73 % was obtained at 14^{0} guide vane opening at 650 rpm. The hill diagram shows that the turbine can be operated at 40 % to 73 % efficiency over a wide range of operating conditions. Extremely low efficiency has not been obtained at any operating conditions like the one seen on design 1. Based on the efficiency of the

turbine, the operating range for design 2 is between Ned values of 1 and 1.5, where the efficiency is over 69.5 %.

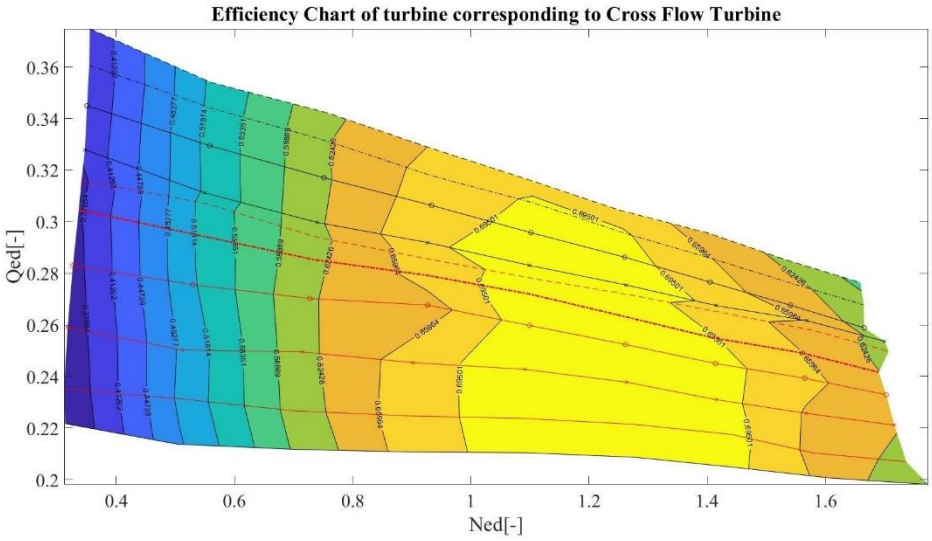

Figure 4-12: Hill diagram of 36º blade angle

Similarly, the Sediment erosion rate density (SERD) hill diagram of the turbine with sediment size ranging from 75 microns to 250 microns was constructed based on the results of CFD analysis. The SERD hill diagram is in conjunction with the efficiency hill diagram, such that the sediment erosion rate density is higher at regions with low efficiency while it was lowest at regions with relatively higher efficiency. However, the minimum values of SERD were obtained at higher RPMs where the efficiency of the turbine is not the highest. In this turbine, the direction of flow and direction of the runner is the same, thus the relative velocity is lowest when the velocity of the water and runner are close to each other, thus when the relative velocity of the water and runner blades at the inlet is lesser, thus showing low sediment erosion. As per the hill diagram, the SERD value is minimum at a small region in the hill diagram, hence the design is not selected for further studies.

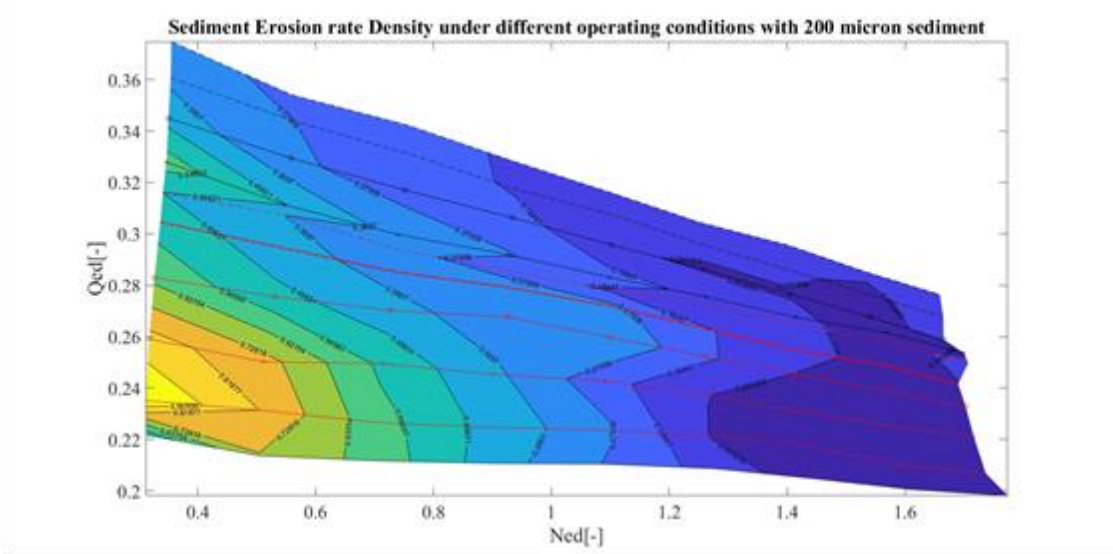

Figure 4-13: SERD Hill diagram of 30^{o} blade angle

4.5.2.3. Design 3 (24^{0} blade angle)

The blade angle at the inlet of the blade is equal to 24^{0} in the design. At the outlet, the blade angle is equal to 90$^{0.}$ The CFD Analysis of the design was performed at different rpm and flowrate keeping the head constant. The efficiency hill diagram has been plotted from the results of the simulation and is shown in the figure below. Maximum efficiency of over 74 % was obtained at 14^{o} guide vane opening at 900 rpm. The hill diagram shows that the turbine can be operated at 40 % to 74 % efficiency over a wide range of operating conditions. Extremely low efficiency has not been obtained at any operating conditions like the one seen on design 1. Based on the efficiency of the turbine, the operating range for design 2 is between Ned values of 1 and 1.5, where the efficiency is over 71.1 %.

Similarly, the Sediment erosion rate density (SERD) hill diagram of the turbine with sediment size ranging from 75 microns to 250 microns was constructed based on the results of CFD analysis. The SERD hill diagram is in conjunction with the efficiency hill diagram, such that the sediment erosion rate density is higher at regions with low efficiency while it was lowest at regions with relatively higher efficiency. However, the

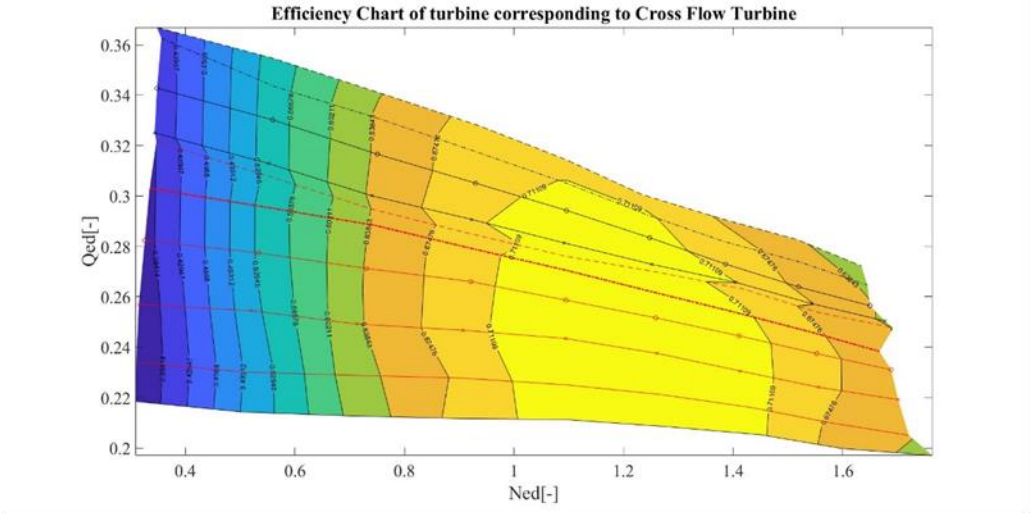

Figure 4-14: Hill diagram of 24^{o} blade angle

minimum values of SERD were obtained at higher RPMs where the efficiency of the turbine is not the highest. In this turbine, the direction of flow and direction of the runner is the same, thus the relative velocity is lowest when the velocity of the water and runner are close to each other, thus when the relative velocity of the water and runner blades at the inlet is lesser, sediment erosion is relatively low. As per the hill diagram, the SERD value is minimum at a small region in the hill diagram, hence the design is not selected for further studies.

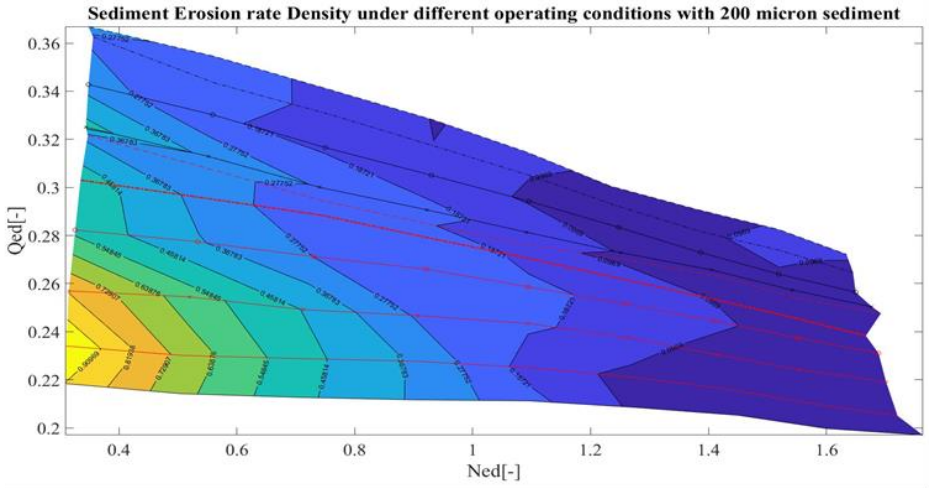

Figure 4-15: SERD Hill diagram of 24^{0} blade angle

4.5.2.4. Design 4 (18^0 blade angle)

The blade angle at the inlet of the blade is equal to 18^o in the design. At the outlet, the blade angle is equal to 90^0. The CFD Analysis of the design was performed at different rpm and flowrate keeping the head constant. The efficiency hill diagram has been plotted from the results of the simulation and is shown in the figure below. Maximum efficiency of over 75 % was obtained at 16^0 guide vane opening at 650 RPM. The hill diagram shows that the turbine can be operated at 42 % to 75 % efficiency over a wide range of operating conditions. Extremely low efficiency has not been obtained at any operating conditions like the one seen on design 1, however, the minimum efficiency region is in the same region. Based on the efficiency seen on the hill diagram, the operating range for design 4 can be set between Ned values of 1 and 1.5, where the efficiency is over 71 % at all the guide vane openings.

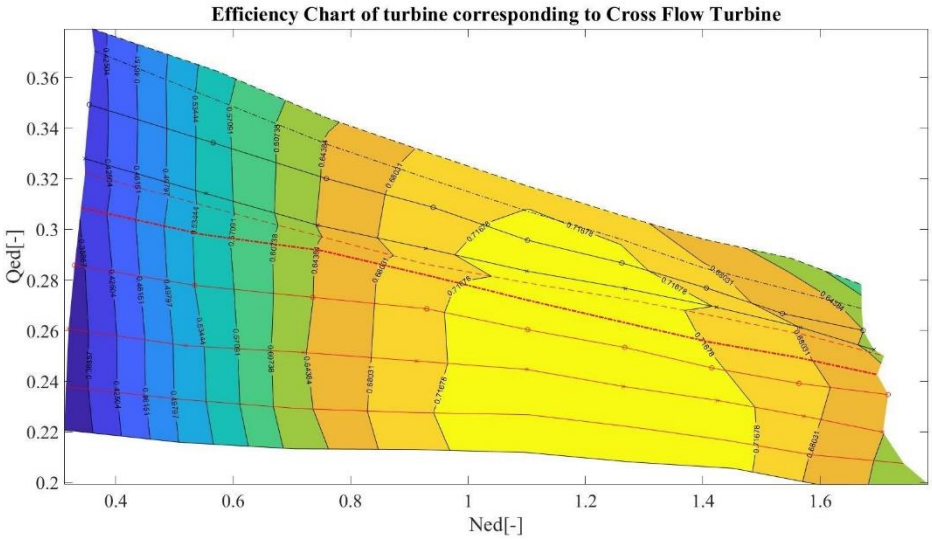

Figure 4-16: Hill diagram of 18^0 blade angle

Similarly, the Sediment erosion rate density (SERD) hill diagram of the turbine with sediment size ranging from 75 microns to 250 microns was constructed based on the results of CFD analysis. The SERD hill diagram is in conjunction with the efficiency hill diagram, such that the sediment erosion rate density is higher at regions with low efficiency. However, the minimum values of SERD were obtained at two regions, a

large operating region at higher rpms show lower values of SERD, which is similar to other designs, while a small patch at Ned value of 0.7 and Qed value of 0.24 showed lower values of SERD. The lowest SERD values at higher rpm can be explained with the same reason explained in design 2: In this turbine, the direction of flow and direction of the runner is same, thus the relative velocity is lowest when the velocity of the water and runner are close to each other, thus when the relative velocity of the water and runner blades at the inlet is lesser, thus showing low sediment erosion.

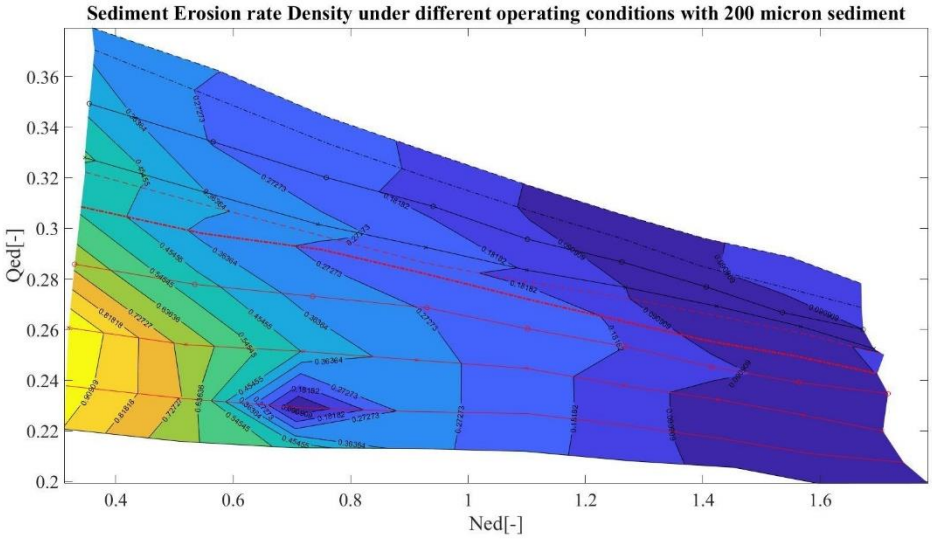

Figure 4-17: SERD Hill diagram of 18^{o} blade angle

4.5.2.5. Design 5 (16^{0} blade angle)

The blade angle at the inlet of the blade is equal to 16^{0} in the design. At the outlet, the blade angle is equal to 90^{0}. The CFD Analysis of the design was performed at different rpm and flowrate keeping the head constant. The efficiency hill diagram has been plotted from the results of the simulation and is shown in the figure below. Maximum efficiency of over 76.8 % was obtained at 12^{0} guide vane opening at 350 rpm. The hill diagram shows that the turbine can be operated at 43 % to 77 % efficiency over a wide range of operating conditions. Extremely low efficiency has not been obtained at any operating conditions like the one seen on design 1, however, the minimum efficiency is obtained in the same region. Based on efficiency as seen on the hill diagram, the

operating range for design 5 can be set between Ned values of 1 and 1.4, where the efficiency is over 73 % at all the guide vane openings.

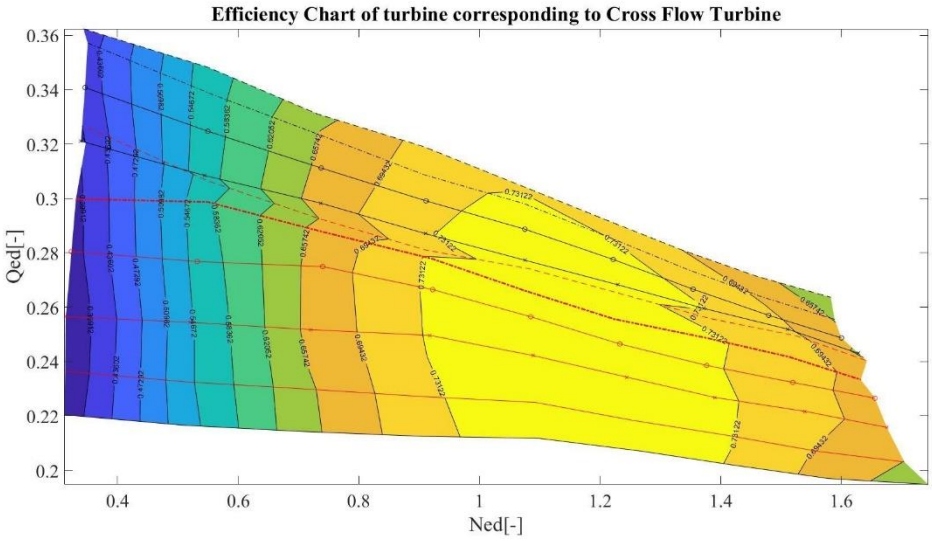

Figure 4-18: Hill diagram of 16^0 blade angle

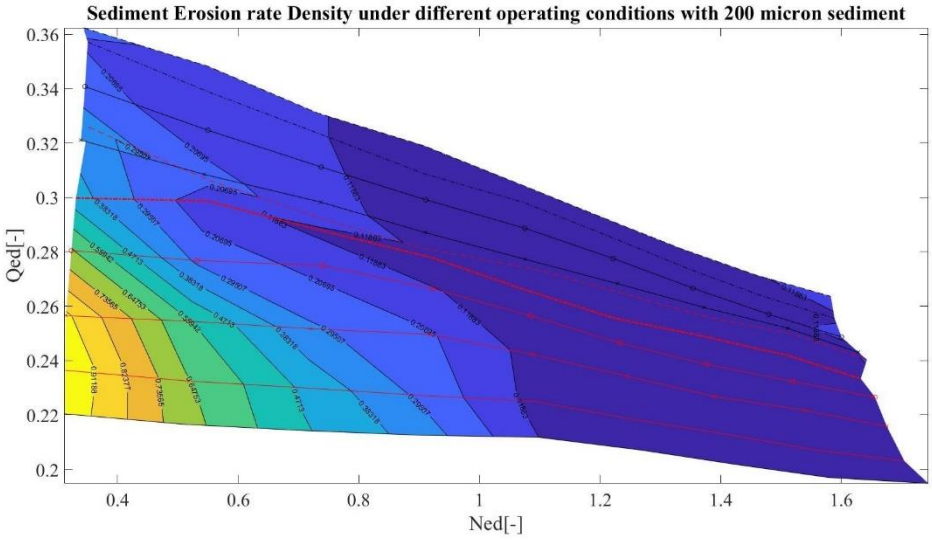

Figure 4-19: SERD Hill diagram of 16^0 blade angle

Similarly, the Sediment erosion rate density (SERD) hill diagram of the turbine with sediment size ranging from 75 microns to 250 microns was constructed based on the results of CFD analysis. The SERD hill diagram is in conjunction with the efficiency

hill diagram, such that the sediment erosion rate density is higher at regions with low efficiency and it is lower at regions with high efficiency. The low SERD region in this design is spread over a greater area compared to other designs for all particle sizes. The sediment erosion is lowest at operating conditions with Ned values of over 1. The operating conditions in terms of sediment erosion are recommended to be a region with Ned values of over 1. The peak efficiency of this design is higher than other designs and the sediment erosion performance is also better compared to other designs, hence this design is considered for experimental analysis and further studies.

CHAPTER 5:VALIDATION AND PERFORMACE ANALYSIS

5.1. Introduction

The experiment was conducted in a open loop in the sediment erosion rig facility at Turbine Testing Laboratory, Kathmandu University. This setup is one of its kind for its ability to conduct sediment erosion tests on model turbines by simulating the operating conditions that exist in actual hydropower plants. The operational limits include a flow rate of 67 l/s and a pressure head of 33 m. The overall layout of the setup is shown in Figure 5-1. A series of experiments were conducted at different speeds and guide vane opening to observe the erosion and performance of CFT.

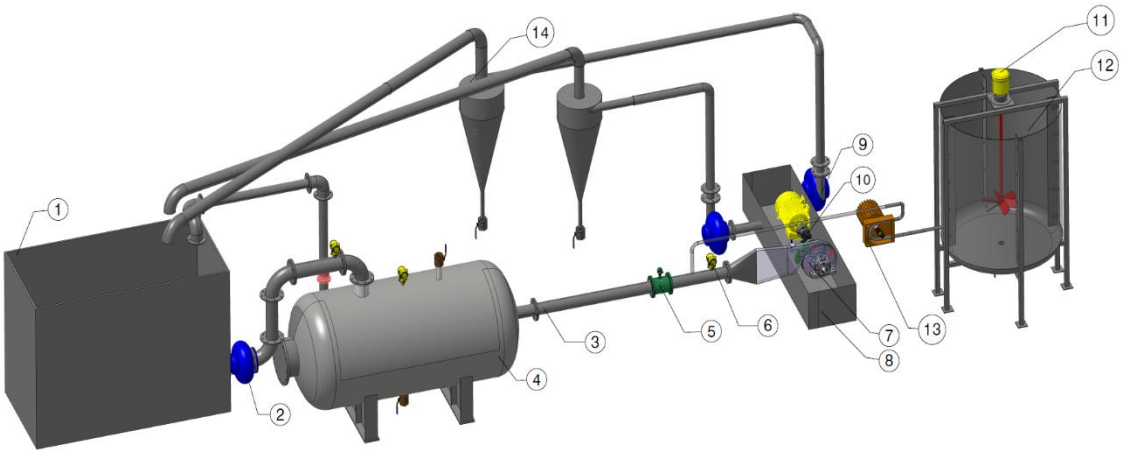

1-Reservior tank, 2-Main pump, 3-Pipeline, 4-Pressure tank, 5-Flowmeter, 6-Pressure transmitter,7-CFT, 8-Turbine outlet tank, 9-Centrifugal pump, 10-Torque transducer,11- Stirrer Motor, 12-Mixing tank, 13-Peristaltic pump and 14- Hydro cyclone

Figure 5-1: 3D view of the experimental test setup

5.2. Experimental setup

This setup consists of two discrete systems that are a sediment injection system and a sediment filtration system as depicted in Figure 5-1 and Figure 5-2. In the former system, the sediment particles are injected into the turbine inlet by the peristaltic pump that delivers the pre-mixed slurry contained inside the mixing tank. The provision of a concentration measurement port at the turbine inlet allows the determination of

sediment concentration using the sand flow method. The latter system includes the hydro cyclone, which separates the sediment particles from the slurry mixture after passing through the turbine. A double suction split type centrifugal pump, driven by VFD is used to supply the required flow into the high pressure tank that stabalizes the fluid to obtain the required head. The electromagnetic flowmeter is mounted between the turbine and pressure tank to measure the discharge. The turbine's inlet pressure is measured by placing two pressures taps, connected to the pressure transducer, at the mid-section of the nozzle. The efficiency measurement is determined by the data obtained from the torque transducer mounted in between the generator and the runner. A data logging system is used to collect and store all the data from the sensors using LabVIEW. The components of the setup as shown in Figure 5-2 are explained in detail.

Figure 5-2: Existing erosion testing facility at TTL

5.2.1. Model turbine

The crossflow turbine is designed at a discharge rate of 45 l/s and operating head of 25 m is used to study and quantify the erosion. The turbine is connected to the main pipeline that branches out of the pressure tank. A torque transducer is mounted between the

runner and a motor, which measure the torque and the speed of the runner. The torque generated during the turbine tests is dissipated in the form of heat through the resistor connected to the VFD that controls the speed of the motor.

CFT with 30 blades and an inlet blade angle of 16^0 was selected for further studies based on the results of numerical analysis. Even though the numerical analysis was performed on a much wider turbine with a width of 280 mm, the turbine was scaled down, by decreasing the width to 31 mm. The turbine was scaled down in order to test it in a lab setup with achievable concentration and quantity. Both performances as well as sediment erosion tests were performed on a 3D printed runner reinforced with the metal casings. The 3D printed runner had 4 slots in which blades, made out of different materials, could be inserted. In order to determine the erosion rate, Aluminum blades were inserted into the slots for experiments in the sediment erosion test rig, described in the previous chapter. The manufacturing drawings of the CFT rig are attached in APPENDIX C.

5.2.2. Pump systems

The pump system comprises of double suction split case centrifugal pump. The model of the pump used is DB 80/16. The specifications of the pump are illustrated in Table 5.1 and the performance curve is shown in Figure 5-3.

Table 5.1: Specifications of the pump

Connection	Fluid	Rated Flow	Rated Head	Rated Speed	Rated Power	Efficiency
Flange-type	Water	41.3 l/s	38.98 m	2940 rpm	17.54 kW	79 %

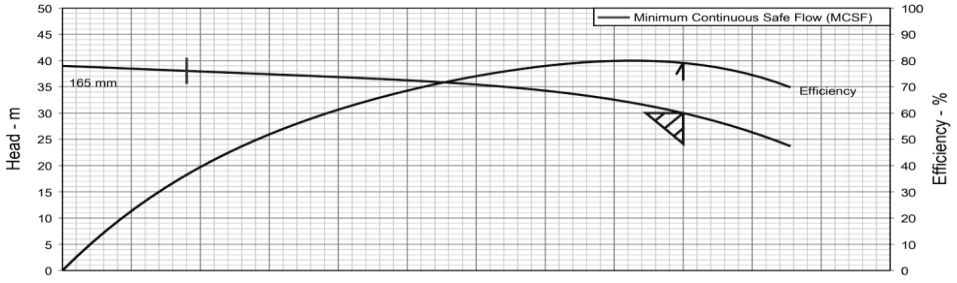

Figure 5-3: Performance curve of the pump

5.2.3. Reservoir tank

A $5m^3$ tank connected to the pump acts as a water supply source to the system. It is used to stabilize the inlet pressure and to prevent fluctuation in the operating head in the main pipeline. The pressure head required for experimentation is generated and varied by changing the rpm of the pump, driven by VFD. The tank is equipped with auxiliary units such as a safety relief valve, a pressure transducer, a bypass valve and a water level indicator. The specifications of the pressure tank are tabulated in Table 5.2.

Table 5.2: Specifications of the pressure tank

Parameters	**Notation**	**Value**	**Unit**
Design pressure	D_p	0.6	MPa
Operating pressure	D_o	0.25	MPa
Shell thickness	T_s	6	mm
Head Thickness	T_h	6	mm
Internal Diameter	D_i	1067	mm
Overall length	L	2400	mm
Maximum allowable working pressure	MAWP	1.4	MPa
Factor of Safety	FOS	3	-
Volume	V	1.75	m^3

5.2.4. Mixing tank

The heterogenous mixture of sediment and water of required volume is prepared inside this tank. This tank comprises four baffles placed at an angle of 90° to disrupt the bulk fluid flow and also to break vortices formed during mixing. The sizing of the mixing tank is calculated based on the empirical relations [110] and the detailed specifications of the tank are tabulated in Table 5.3.

Table 5.3: Specifications of the mixing tank

Parameters	Notation	Relations	Value	Unit
Volume capacity of the tank	V	-	1500	l
Height of the tank	H	-	1.5	m
Diameter of the tank	D_T	-	1.2	m
The ratio of height to diameter	H/D_T	-	1.25	-
The calculated volume of the tank	V_T	$\pi*r^2*H$	1.70	m^3
Diameter of the impeller	D_a	$D_T/3$	0.4	m
Size of the baffle	J	$D_T/12$	0.1	m
A gap of the baffle from the wall	O	$D_T/60$	0.02	m
Location of the impeller	C	$D_T/3$	0.4	m
Width of the impeller	W		0.08	m
Length of the impeller	L	$D_A/4$	0.1	m
No. of baffles	N	-	4	-
Power of the motor	P_m	-	5	hp

5.2.5. Peristaltic pump

The peristaltic pump is a positive displacement pump and is ideal for pumping abrasive-laden mixtures at high concentrations (see Figure 5-4). The detailed specifications of the peristaltic pump are illustrated in Table 5.4. The alternating compression and relaxation of the tube by the rotary movement of rollers are responsible for drawing mixture in and forcing it away from the pump. Also, it works as a check valve, thus preventing the backflow of the mixture due to the high-pressure line at the main pipeline. A precise and variable flow rate at the inlet of the turbine depends on the tube diameter, and speed controlled by the VFD.

Figure 5-4: Peristaltic pump used in the experiment

Table 5.4: Specifications of the peristaltic pump

Model	Power supply	Power	Speed	Tubing	Flow rate	Pressure
		Watts	(rpm)	ID * thickness (mm)	L/min	(MPa)
J25/DZ45	380V/50 Hz	370	30-300	25.4*4.8	2.6-26	0.25

5.2.6. Test specimen

The optimized Runner Design 5 is selected for the test as described in Chapter 4. The 3D CAD model is used for producing Acrylonitrile Butadiene Styrene (ABS) runner through a 3D printer. There is altogether 30 number of blades. The 3D model of the test rig is shown in Figure 5-5(a). Out of 30 blades, 4 specimen blades can be made detached able into the grooves made in the disc of the runner as shown in Figure 5-5(b). These specimens are made up of Aluminum and the properties are illustrated in

Table 5.5.

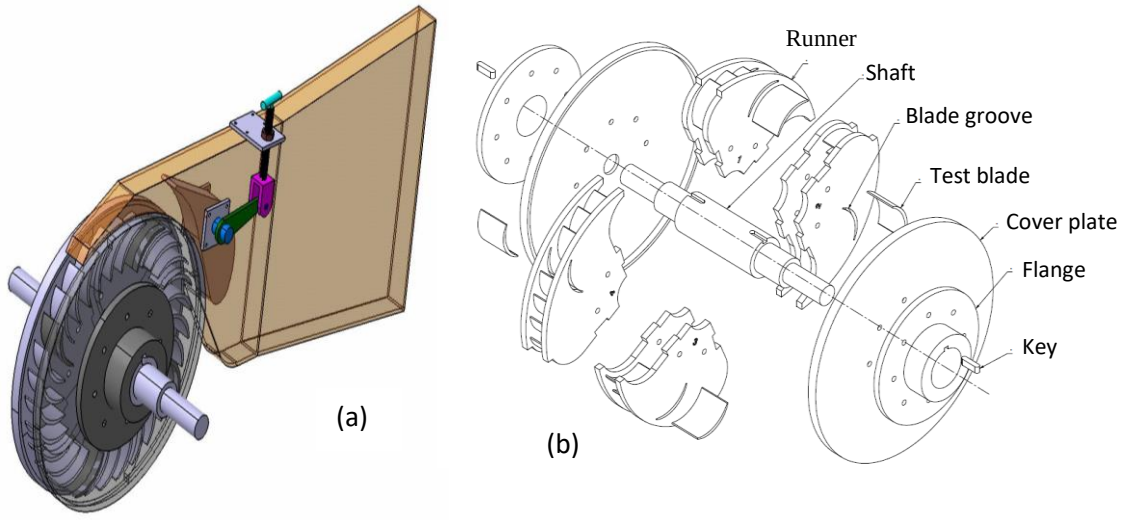

Figure 5-5: (a)3D CAD model of runner and (b) Exploded view of specimen blade arrangement

Table 5.5: Mechanical properties of an Aluminum specimen

Specimen	Standard	Density (kg/m^3)	Hardness (HB)	Modulus of elasticity (MPa)	Tensile strength (MPa)	Ultimate Strength (MPa)
Aluminum	AA5083	2700	70	47	95	110

5.2.7. Hydro cyclone

This device has been used to prevent the re-entry of the sediment particles into the circulating line after striking the runner. The hydro cyclone model is designed based on the Bradley model [111] with an inlet flow conditions of 23 l/s as depicted in Figure 5-6.

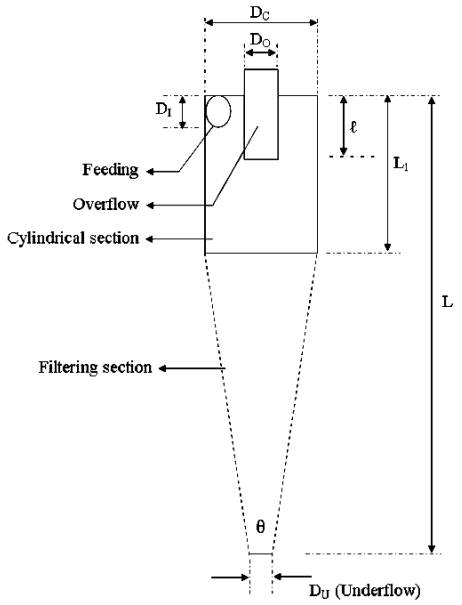

Figure 5-6: Nomenclature of the hydro cyclone

Two hydro cyclones are used in the system which can be run in parallel mode. The details of the geometrical parameters obtained are tabulated in Table 5.6.

Table 5.6: Dimensions of the hydro cyclone

Parameters									
Reduced cut size diameter (d_{50})	**Diameter of cyclone chamber (D_c)**	**Inlet Dia.**	**Overflow Dia.**	**Underflow Dia.**	**Vertex finder length**	**Cylindrical section length**	**Cone angle**	**Length of the cone**	**Circular Inlet Diameter**
		$D_i = D_C/7$	$D_o = D_C/3$	$D_U = D_C/10$	$S_c = D_c/3$	$L_1 = D_C/2$	$\gamma°$	$L_C = 2D_C$	H
30	45	6.43	12.5	4.5	15	23	9	90	80

5.3. Sediment collection and analysis

5.3.1. Particle Size Distribution

The sediment sample used for the testing is obtained from the headworks and forebay of Chauri Khola 'V' Micro hydropower plant by grab sampling method. The collected sample was washed to remove debris and clay particles. The sample was then dried in the oven to remove moisture content. As different types of minerals present in the sediment have varying erosion potential to turbine material due to their hardness and geometric properties, mineral analysis was performed using the Particle count method via. Stereo Trinocular microscope. And, Particle Size Distribution (PSD) of the sample was carried out using sieve analysis to obtain the percentage content of different sized particles as depicted in Table 5.7. This data helps to identify critical sediment size that reaches the turbine and cause runner erosion.

Table 5.7: PSD analysis

S. N	Sediment Size (µm)	Forebay Weight (kg)	Weight of Quartz & feldspar (kg)	Weight %	sediment concentration (kg/s)
1	75- 125	0.24	0.18	7	0.38
2	125-150	0.52	0.39	14	0.82
3	150-200	1.82	1.365	49	2.88
4	200-250	1.1	0.825	30	1.74
Total Weight		**3.68**	**2.76**	**100**	**5.83**

Table 5.7 shows that the maximum sediment concentration of 2880 ppm was obtained for the sediment size range 150-212 µm. From PSD data, it was found that around 49

% of the sediment has a particle size in the range of 150-212 µm, followed by 30 % availability of sediment particles in the range of 212-250 µm. The availability Thus, the sediment size range for the experimentation was taken below 250 µm.

5.3.2. Mineral Analysis

Mineral analysis of the sediment samples collected from the headwork and forebay was conducted. Average percentages of each mineral for the sediments sample are represented by pie charts shown in Figure 5-7.

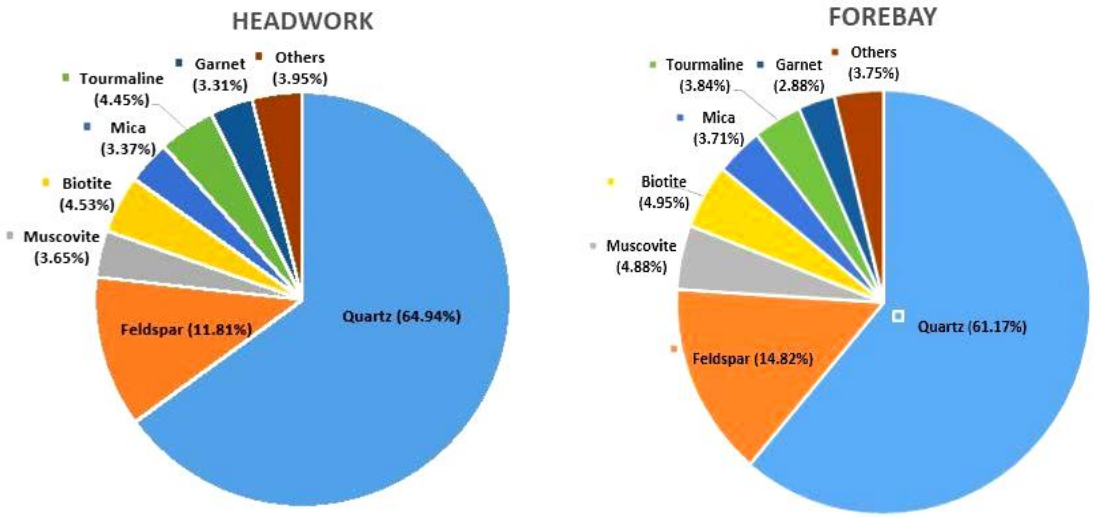

Figure 5-7: Mineral composition of sediment samples used

Figure 5-7 shows that quartz, feldspar, muscovite, biotite, tourmaline, mica and garnet are the constituent minerals of sediment at the headwork and forebay of ChauriKhola V MHP. Quartz is the most common mineral whose percentage is found to vary from around 65 % at headwork to around 61 % at forebay. Similarly, feldspar constitutes almost 11.81 % at headwork and 14.82 % at forebay. The percentage of muscovite at headwork is 3.65 % which slightly increases to 4.88% and biotite gradually increases from 4.53 % at headwork to 4.95 % at forebay. A little variation of tourmaline and garnet is observed at the sampled locations of sediments. Minerals other than the above mentioned are grouped as other minerals which are about 3.5 % of total sediment as indicated by the particle count method of mineral analysis.

5.4. Erosion Measurement

The erosion was measured with an electronic weighing machine having the least count of 0.0001 g. The model of the weighing machine is BEL Engineering MG-124Ai. The weight loss method was used to measure the material removal that occurred after each test run. The overall erosion rate was obtained by taking an average of erosion in all 4 blade specimens after each test.

Figure 5-8: Weight measurement using the electronic balance

5.5. Flow rate and pressure measurement

The flow rate is varied by varying the opening angle of the guide vane of the turbine. It was measured by mounting the electromagnetic flowmeter between the turbine and the pressure tank's outlet. Likewise, the pressure head at the turbine's inlet is measured by taking an average of two pressure tapings, sensed by an absolute pressure transducer placed at the nozzle.

5.6. Instrumentation and Calibration

The CFT was connected to a 15 kW induction motor. The test rig included a pressure transmitter, a volume flow meter, a torque transducer and a rotational speed indicator. All the measuring instruments were connected through a National Instruments logging card to a computer with a specialized LabVIEW logging program. The outputs of the

instruments included current and voltage signals. Figure 5-9 shows a schematic overview of the placement of the instruments on the test rig.

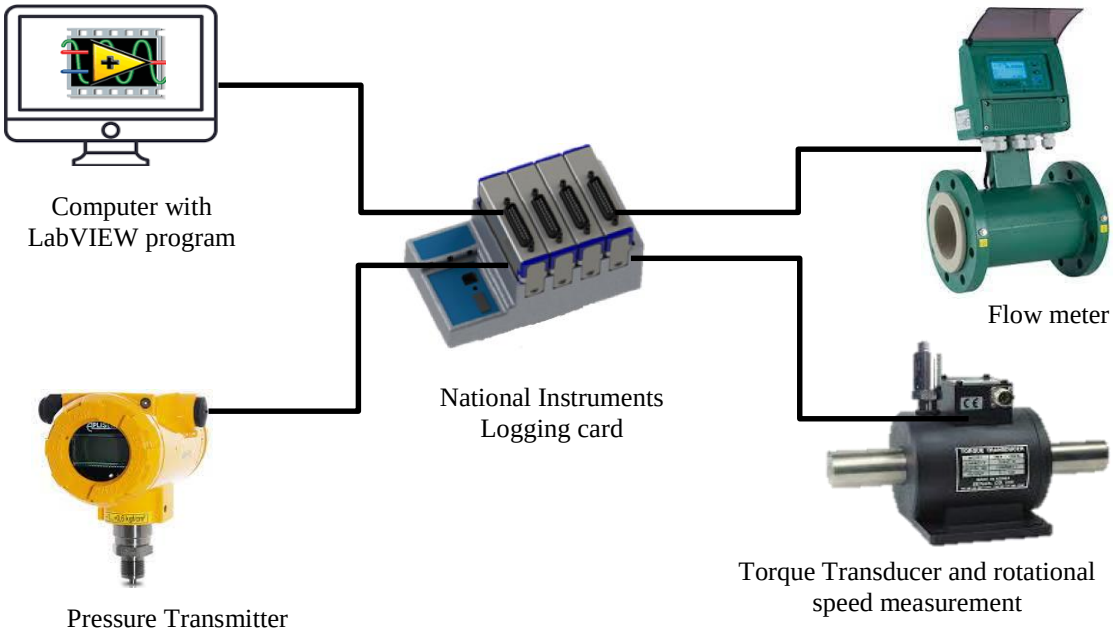

Figure 5-9: Schematic illustration of the measuring instrument setup

5.6.1. Electromagnetic flowmeter

The electromagnetic flowmeter was placed in the main pipeline between the pressure tank outlet and turbine inlet to measure the fluid flow rate. The flow meter works on the principle of the generation of a magnetic field that is proportional to the flow velocity. The model of the flow meter used is MS2500. The detailed specifications of the device are tabulated in Table 5.8.

Table 5.8: Specifications of the Electromagnetic flow meter

Connection	**Size**	**Fluid**	**Output**	**Power**	**Accuracy**
ANSI Flange	DN100	Water	4-20 mA	24-36V DC	±0.2 %

The flow meter used in the experiments and its calibration plot is shown in Figure 5-10.

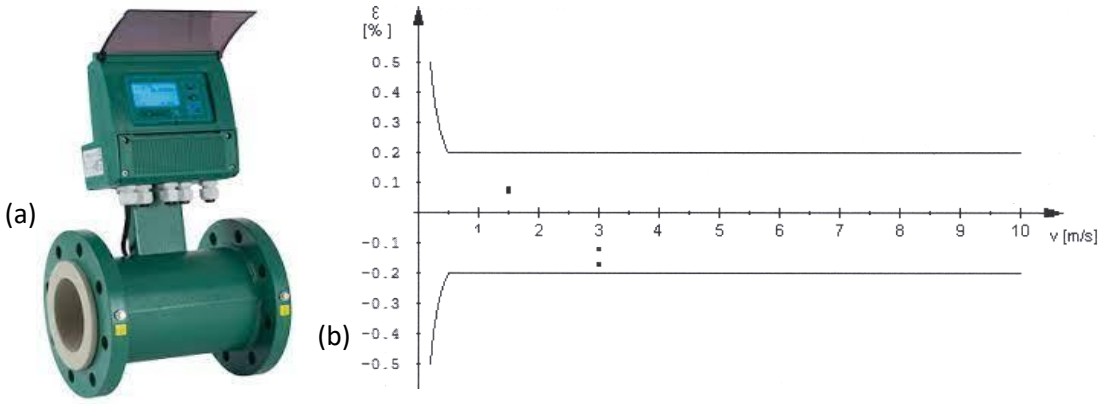

Figure 5-10: (a) Electromagnetic flow meter (b) Calibration data

5.6.2. Peristaltic pump

The flow calibration of the peristaltic pump was conducted on-site to determine the performance of the pump at various speeds. The known volume of a slurry mixture from a 1500 liters' tank was connected to the inlet of the pump while the outlet flow was collected in another measuring cylinder at different speeds of the pump. The plot of flow versus speed of the pump is graphed in Figure 5-11 and it showed that the flow rate from the pump varied in linear trend with the increasing speed of the pump.

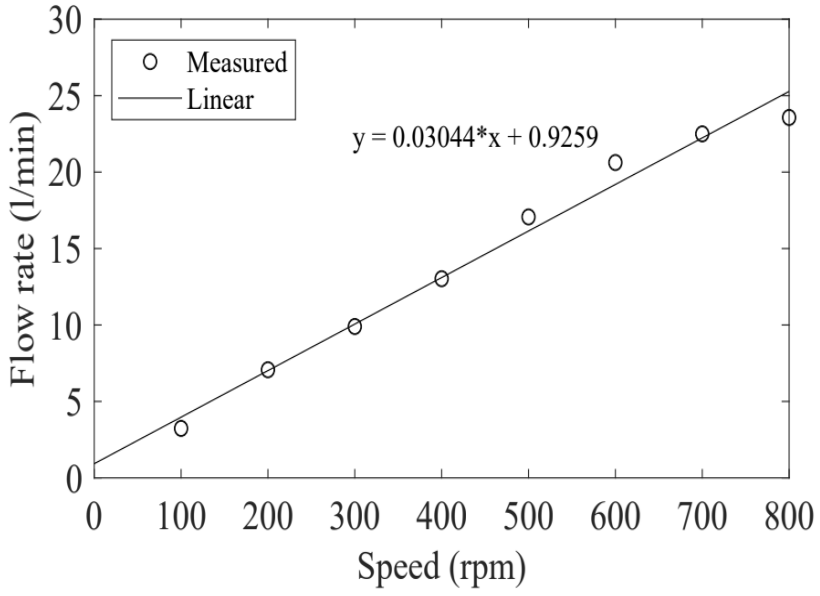

Figure 5-11: Plot of current signal versus flow rate

5.6.3. Pressure transmitter

The erosion test contains two absolute pressure transmitter, one placed at the turbine's inlet and the other at the pressure tank. The *APLISENS* pressure transmitter of measured capacity up to 5 bars was installed in the turbine inlet. The standard specifications of the pressure transmitter are listed in Table 5.9.

Table 5.9: Specifications of Pressure transmitter

Descriptions	**Value**
Type	APC-2000ALW
Pressure set range	0-5 bars
Output signal	4-20 mA
Accuracy	±0.075 %
Ambient temperature	24°C

IEC 60913 [112] describes the dead weight manometer as a primary calibration method for pressure measuring devices. The pressure transmitter was calibrated with a Nagman Pneumatic tabletop model P8600-SP-20-1 deadweight manometer.

Figure 5-12: Setup for pressure transmitter calibration

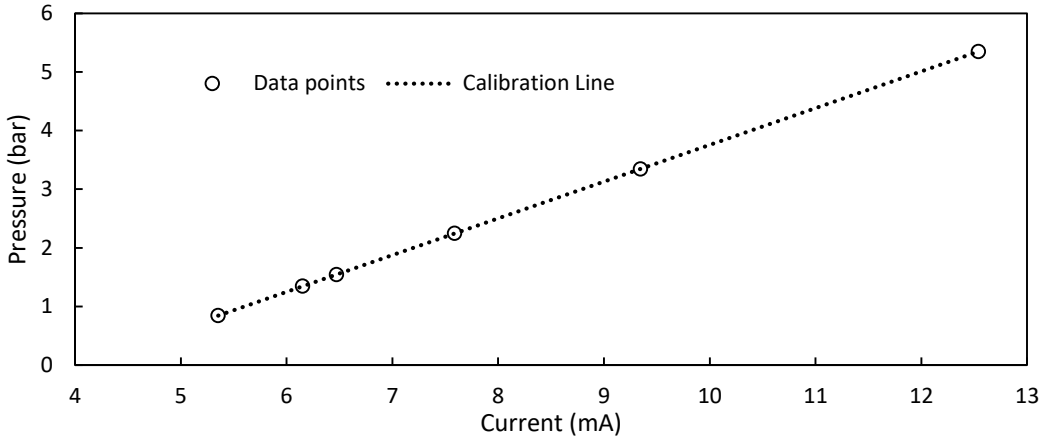

Figure 5-13: Pressure transmitter calibration data

5.6.4. Torque Transducer

The torque transducers' shaft is coupled with the turbine shaft and the generator shaft to measure the output torque generated. The device used in the experimentation is rotary type torque transducer. The transducer used includes built-in rpm and torque sensor. The strain gauge fitted to the shaft along with the brush and slip ring produces a signal that is logged to the logging device to measure torque and speed with high accuracy. Figure 5-14 shows the model, its schematic and overall dimensions of the torque transducer. The detailed specification of the torque transducer is tabulated in Table 5.10.

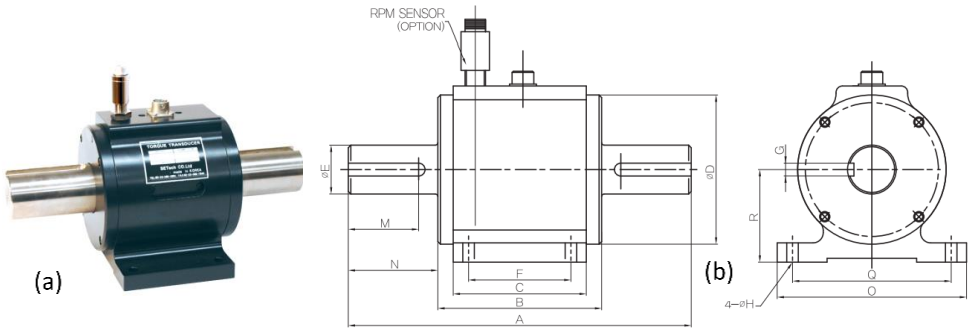

Figure 5-14: (a) Torque Transducer and (b) Dimensions of the Torque Transducer

Table 5.10: Torque transducer specifications

Parameters	**Value**
Rated capacity	0-50 kgf-m
Rated output	1.5 mV/V
Non-Linearity	0.3 % R.O
Hysteresis	0.08 % R.O
Repeatability	0.09 % R.O
Terminal resistance input	350±5Ω
Terminal resistance output	350±5Ω
Insulation resistance	300 MΩ
Temperature safe range	-20°C-70°C
Excitation	10 V DC
Safe overload	150 % R.C

The calibration of the torque transducer was performed using a static calibration method in a calibration setup. This setup consists of two identical lever arms mounted to either end of the torque transducer's shaft. The other end was mounted with known mass loading and unloading systems.

Figure 5-15: Setup for torque transducer calibration

The torque signal generated by the loading known mass was recorded into the logging device. The torque transducer was loaded and unloaded to check hysteresis two times in the direction to be calibrated by applying the maximum torque value of the device.

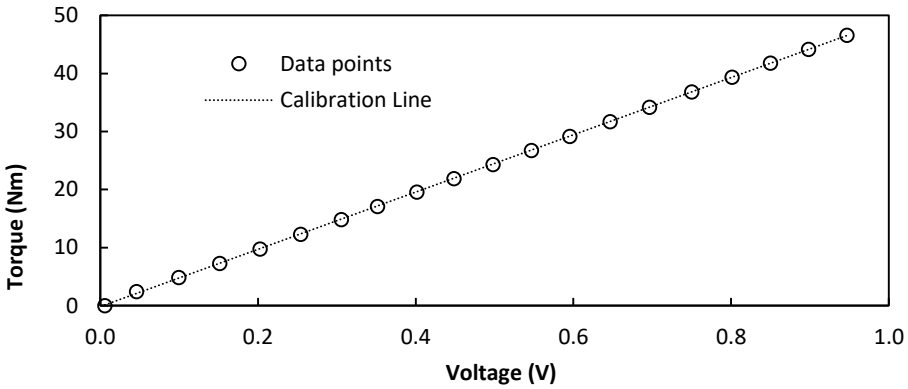

Figure 5-16: Torque transducer calibration curve

For each loading and pre-loading duration of 30 seconds is to obtain stable values. The plot of torque value versus voltage signal is as indiated in

Figure 5-16.

5.7. Uncertainty Analysis

All measurements made while performing experiments always include inaccuracy within the measuring instrument. Experimental uncertainty can be generally classified into two types of errors i.e., random or statistical error and systematic error. Random errors are an outcome of irregular variations that arise during experimental measurement. Unpredictable fluctuations in temperature, grid line voltage, mechanical vibrations in an experimental setup, human error and so on are the source of random errors. Systematic errors are related to measurement instruments or techniques. Systematic errors occur, when improperly “zeroed” or a faulty instrument are used for the measurement.

5.7.1. Uncertainties in calibration

5.7.1.1. Uncertainty in the calibration of Pressure Transmitter

The calibration uncertainty of the pressure transmitter considered are a) total error in calibration method f_{Pab}, b) the uncertainty in the measurement of the height between the deadweight manometer and the measuring point of the pressure transducer $f_{Pf\ and}$ c) systematic and random error in the instrument $f_{\tau\ regression}$. The documentation attached with the dead weight manometer states that the total error in the instrument f_{Pab}, is ±0.025 %. The height difference between the deadweight manometer and the measuring point of the pressure transmitter is measured to be 46.6 mm with the assumed uncertainty of the rule measurement is ±0.1 mm. With 46.6 mm of height difference, the uncertainty f_{pf} is ±0.21 %. The systematic and random error in the instruments is calculated by the methods described in Appendix D and is ± 1.01 %

The maximum total uncertainty for the calibration of the pressure transmitter is combined with the Residual Sum of Squares (RSS) method using Eq. 5.1 and is found to be ±1.0319035 %

$$max(f_{\text{pcal}}) = \pm\sqrt{f_{Pab}^2 + f_{pf}^2 + max(f_{\tau\ \text{regression}})^2} \qquad (5.1)$$

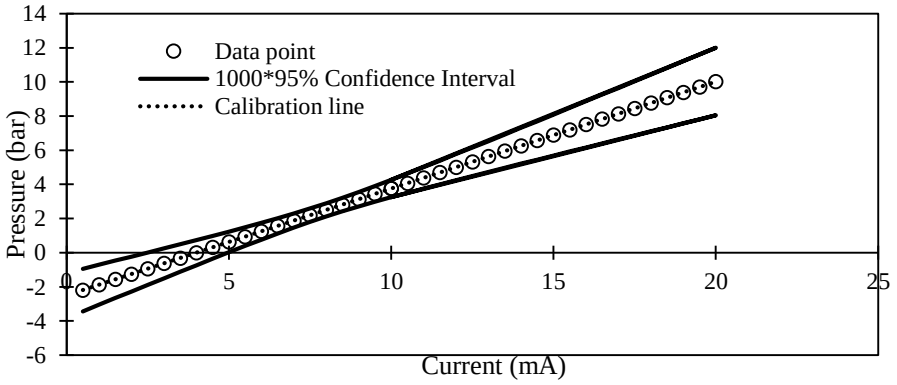

Figure 5-17: Calibration curve and 95 % confidence interval scaled up by 100

The calibration curve with 95 % confidence interval for torque transducer is presented in Figure 5-17.

5.7.1.2. Uncertainty in the calibration of torque Transducer

The calibration uncertainty of the torque transducer is a) Systematic error in weighs and weight bed $f_{\tau W}$, b) systematic error in the length of the arm $f_{\tau\ arm}$ and c) systematic and random error in the instrument $f_{\tau\ regression}$. The systematic uncertainty in the weights used is estimated by using the known weights and calculated to be ±0.17157 %. The systematic uncertainty in the length of the arm with 0.49886m is considered as 0.1 mm which yields uncertainty of ±0.0200457 %. The systematic and random error in the instruments is calculated by the methods described in Appendix B and is ± 1.78 %

The maximum total uncertainty for the calibration of the torque transducer is combined with the Residual Sum of Squares (RSS) method using Eq. 5.2 and is found to be ± 1.7883618 %

$$max(f_\tau) = \pm\sqrt{f_{\tau W}^2 + f_{\tau arm}^2 + max\left(f_{\tau\ regression}\right)^2} \quad (5.2)$$

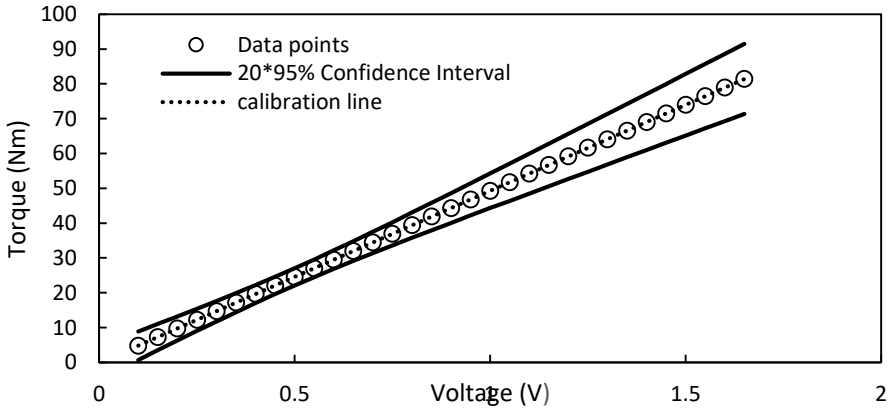

Figure 5-18: Calibration curve and 95 % confidence interval scaled up by 20

The calibration curve with a 95 % confidence interval for torque transducer is presented in Figure 5-18.

5.7.2. Uncertainty of the experiment

The overall uncertainty of the experiment can only be estimated after all experimental observations have been made. This includes calibration uncertainty and errors generated during the experiment. Measurement errors occur when the instrument provides

different outputs for a given input. Output fluctuations are caused by independent variables in the instrument. The error for each device is estimated using the student confidence intervals from the data obtained from the recorded data. The random uncertainty of the measurement of the pressure transmitter, the torque transducer and the flowmeter is calculated using Eq. E.9 and E.10 in Appendix E. The maximum uncertainty during the experiments were 0.9346145 %, 0.0035797% and 0.2398524 % for the pressure transmitter, the torque transducer and the flowmeter respectively. The maximum uncertainty in measurements of the pressure transmitter, the torque transducer and the flowmeter is calculated using Eq. E.8 of Appendix E are found to be 1.3922 %, 1.7883 % and 0.3123 % respectively. The range of systematic uncertainty of rotational speed recommended by IEC 60193 [112] is 0.01% to 0.05%. The maximum random uncertainty of rotational speed measurement was found to be 0.0089%. The combined maximum uncertainty was 0.0508 %.

5.7.3. Total Uncertainty in Efficiency

The uncertainty of efficiency is calculated with the methods described in Appendix E.

The maximum total uncertainty in the efficiency can be found to be 2.833 %. The calibration value is not constant for all the operational conditions, it varies. The maximum uncertainties of all the instruments hardly coincide.

5.8. Experimental result and discussion

Experiments were performed in two stages, with and without the sediment in the system. The performance test was executed at constant head of 10m with variable guide vane openings and different RPMs without injecting the sediment into the system. Then sediment was injected into the system to observe wear pattern and amount of weight loss in the test specimens.

5.8.1. Performance of the turbine

The performance of the turbine is analyzed through the estimation of the efficiency of the turbine. To calculate the efficiency of CFT, four parameters: shaft torque, shaft rotational speed, flow rate, and pressure at the nozzle were measured. The head of the crossflow turbine is estimated as the differences between specific energies at the inlet

and outlet of the turbine. The outlet is under atmospheric pressure and exit velocity is taken as zero. Therefore, the net head is calculated using the following equation.

$$H_e = \frac{{v_1}^2}{2g} + \frac{\Delta p}{\rho g} + Z \quad (5.3)$$

Where v_1 is the Velocity of the water at the inlet, Δp is differential pressure between inlet and outlet, Z is the Difference in height between the pressure transducer and outlet of turbine

The efficiency of the turbine is the ratio of the power available at the shaft of the turbine to hydraulic power delivered to the runner. It is calculated via the following equation

$$\eta = \frac{T\omega}{\rho g Q H_e} \quad (5.4)$$

Where T is Measured shaft torque, ω is Angular velocity, ρ is Density of water, g is Gravitational acceleration, Q is Volumetric flow rate, H_e is the Net head.

The hydraulic efficiency is presented through a hill chart following the procedure provided by IEC 60193 [112]. The efficiency with respect to dimensionless parameters discharge factor Q_{ed} and Speed factor n_{ed} at constant guide vane line opening is plotted. These parameters are computed as stated in equation (3) and equation (4)

$$N_{ed} = \frac{nD}{\sqrt{gH}} \quad (5.5)$$

$$Q_{ed} = \frac{Q}{D^2\sqrt{gH}} \quad (5.6)$$

where n is the rotational speed and D is the outlet diameter of the runner.

A series of experiments were performed with a constant head of 10 m with rotational speed varying from 350 RPM to 750 RPM with an increment of 100 RPM and guide vane opening ranging from 10 % to 100 % with an increment of 10 %. The results of the measurements have been plotted in the Hill chart diagram as shown in Figure 5-19.

The chart shows the normalized efficiency with respect to dimensionless parameters discharge factor Q_{ed} and Speed factor N_{ed} at constant guide vane line opening.

The chart indicates that the turbine has its best efficiency at the range of parameters, N_{ed} (1.8 to 2.2) and Q_{ed} (0.014 to 0.018*)*. The maximum value i.e., 1 is obtained at n_{ed} 1.905 and Q_{ed} 0.014. From 40 % to 80 % guide vane opening, efficiency is above 90 % of the best efficiency point (BEP) values between 1.8 to 2.2. A simple rectangular operating area is drawn in Figure 5-19 that can be a region for the operation of CFT. The turbine can be operated from 40 % to 100 % guide vane opening with N_{ed} from 1.8 to 2.2 to Q_{ed} from 0.014 to 0.018.

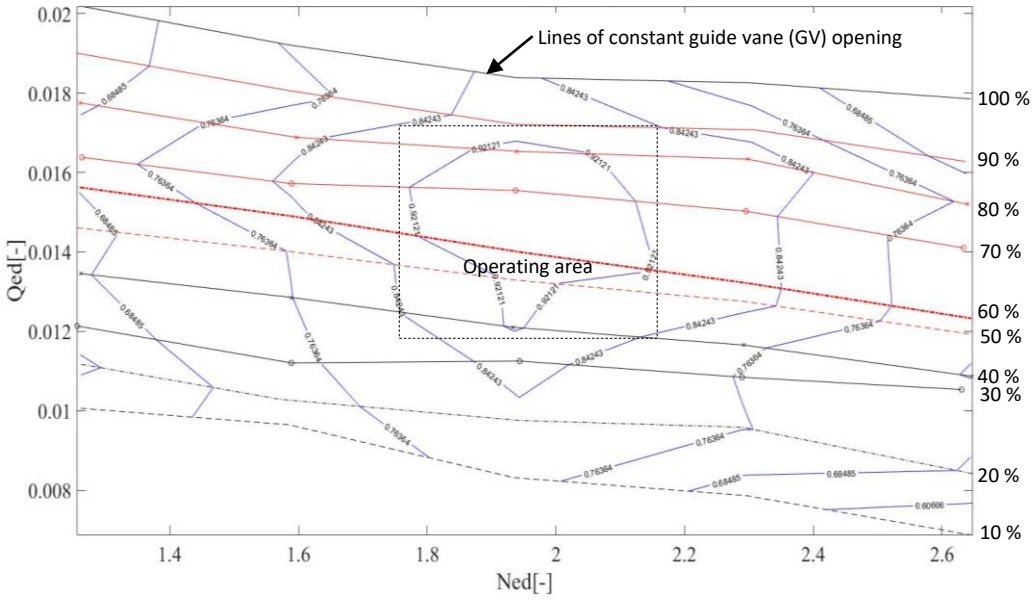

Figure 5-19: Efficiency hill chart of the Crossflow turbine at 10m head

CFD analysis was performed on the model Crossflow turbine with the reduced width under various operating conditions. The CFD analysis was performed by keeping the head at the inlet of the turbine equal to 10m. The performance of the turbine was predicted at various guide vane angles and rpm values. An efficiency hill diagram was plotted based on the results of CFD to compare it to the efficiency hill diagram drawn from the results of the experimental analysis. The hill diagram depicts the efficiency normalized by the maximum efficiency obtained from CFD analysis at 10m head. The

regions with maximum efficiency are obtained between the N_{ED} values between 1.5 and 2.4 and Q_{ED} values between 0.012 and 0.02, which is very similar to the results obtained from the experimental analysis.

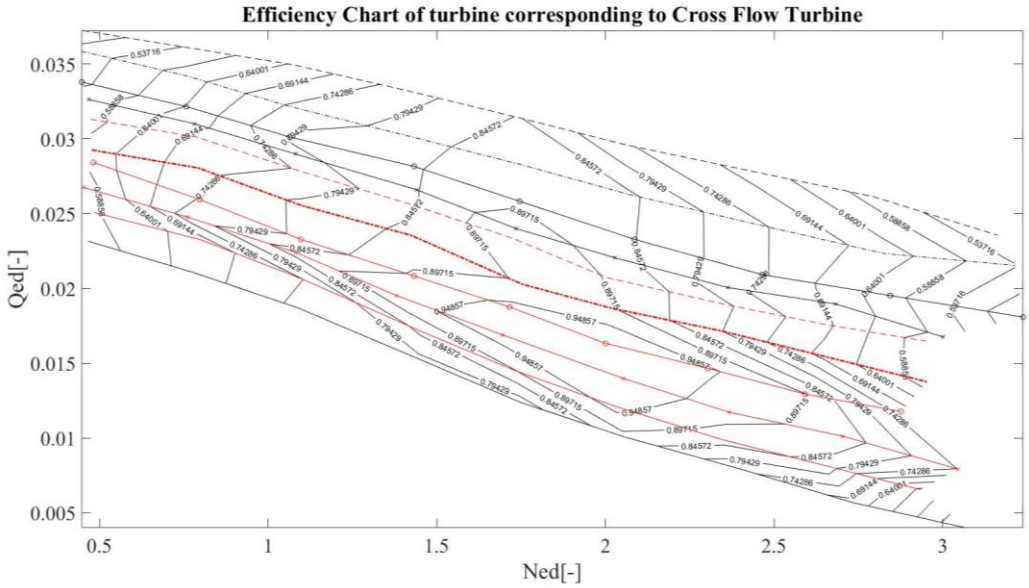

Figure 5-20: Efficiency hill chart from CFD analysis of Crossflow turbine at 10m head

5.8.2. Erosion Pattern

For the observation of abrasive erosion, the detachable aluminium test blades were sprayed with three different colours. The first and second layers were coated with red colours, then the next two with yellow and finally the fifth and sixth with blue colours. Multi-layer coatings were done with a motive to observe the removal of paint from the surface of the test specimens to identify the location of wear due to abrasion erosion. The photographs of the test specimen were taken after every two hours of a test run to observe the removal of paint from the surface of test specimens and study the gradual development of the wear with an advancement of test run time. The series of tests were performed for a total of 8 hours in an interval of 2 hours. The observation of the pattern of wear was carried at 10m head with 357 RPM, 15 l/s flow rate and 15000 PPM at 10^{o} from full closed GV position. The higher sediment concentration was considered to accelerate the experiment. The pattern and location of the wear in all the specimens were

found to be identical. Figure 5-21 and Figure 5-22 show the coated test specimen before the test is performed every two hours and in a total of eight hours of the run. Figure 5-21(a) shows the photograph of coated blades when viewed from the leading edge before the experiment. The removal of layers of paint coatings in Figure 5-21 (b),(c), (d) and (e) clearly indicates that severe erosion has occurred on the surface of the blade. After two hours of operation, abrasion erosion was observed on the tip of the leading edge along the width of the blade. The removal of paint coatings radically increased over the surface of the blade. The multiple coated paint was mostly removed along the width that is located at one-fourth distance from the leading edge of the blade.

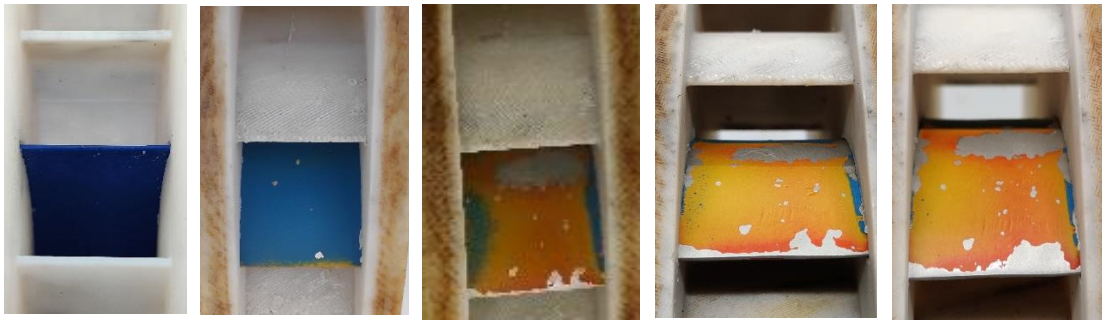

(a) (b) (c) (d) (e)

Figure 5-21: Erosion pattern at suction side from leading edge at first stage : (a) 0 hr., (b) 2 hr., (c) 4 hr.,(d) 6 hr. and (e) 8 hr.

Figure 5-22 exhibits a progressive abrasive erosion pattern on the pressure side of the blade viewed from the trailing edge. The erosion was found at either end of the blade surface along its curvature after a run of 2 hours. As the test progressed, the erosion got more pronounced all over the surface of the blade.

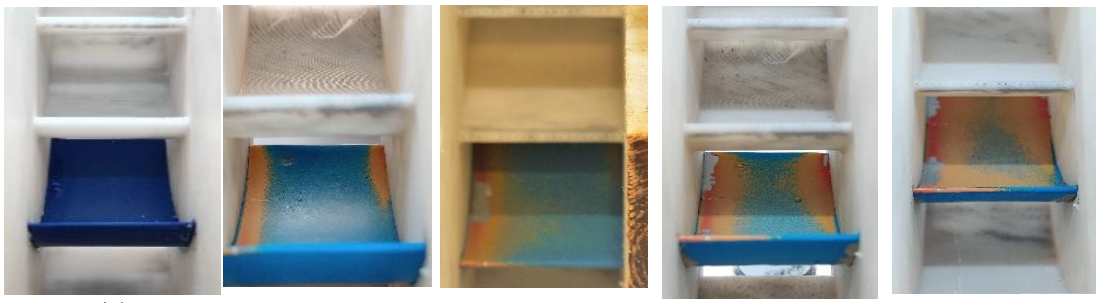

(a) (b) (c) (d) (e)

Figure 5-22: Erosion pattern at Pressure side view from trailing edge at the first stage : (a) 0 hr., (b) 2 hr., (c) 4 hr.,(d) 6 hr. and (e) 8 hr.

Once the experiment work was completed, the coated blade was removed from the plastic runner to observe the overall removal of paint. Figure 5 22 (a) and (b) shows the pressure side and suction side of the test specimen respectively with and without paint

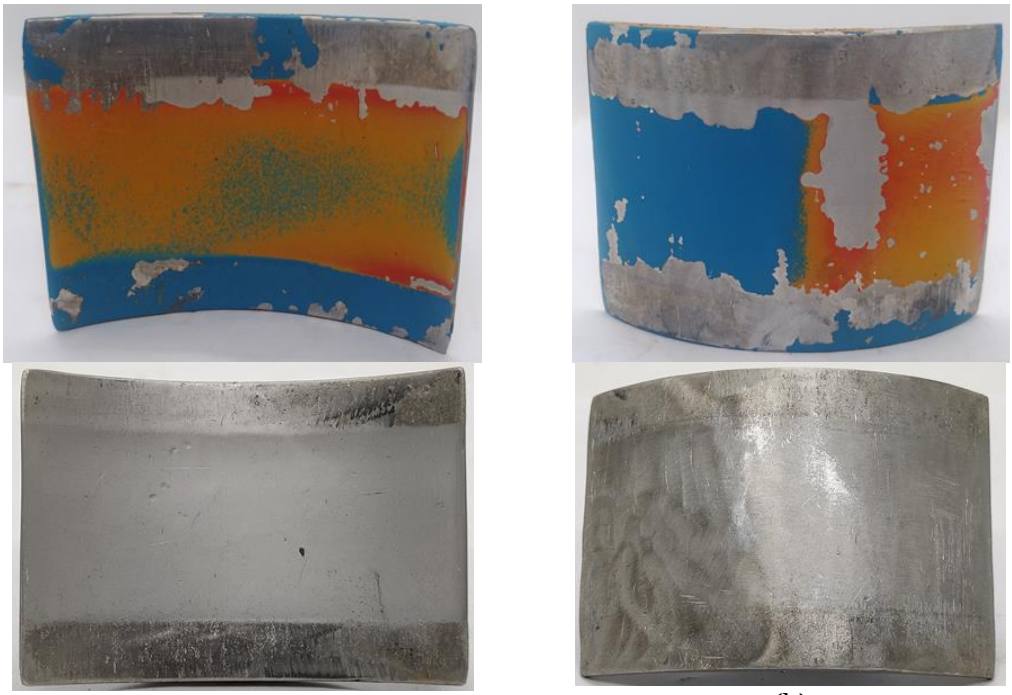

(a) (b)

Figure 5-23: Wear observed in (a) pressure side and (b) suction side.

the coating on the surfaces. The wear effect was observed on the entire surface of the pressure-side blade passing under the water flow path shown in Figure 5-23(a). However, on the suction side, it was found that the erosion on the surface of the blade is drastically uneven. On the one-fourth area of the blade from the leading-edge side, there was a removal of four layers of paint; then in other another quarter area, the coating was chipped away and then on the remaining surface, the paint remained as it was before the test run which is as presented in Figure 5-23(b). The study of the erosion on the blade CFT is very complex as the water led from the guide vane hits the blades twice before it leaves the runner. At the first stage, water strikes on the leading edges of a number of blades and leaves through the trailing edge. Then the jet of water moves through the runner and at the second stage, water again hit the blade from inside of the

runner. On the pressure side of the blade, which comes under the water flow path, the effect of wear was visible throughout its surface as in Figure 5-23(a). The progression of wear pattern and location wear on the surface of the blade was investigated.

The validation of the experimental result is performed through the numerical study and also with the eroded runner of Daram Khola MHP [101]. The project is equipped with two CFT turbines which are mechanically synchronized with a single generator with a gross head of 13 meters and flow rate of 550 l/s. All the technical parameters of the test were considered to perform the numerical simulation of the test turbine. Figure 5-24 shows the predictions of erosion rate density along CFT blade surfaces and especially focuses on blade number 6. The identical erosion pattern was observed on the runner of MHP, on the blade during the experiment and also from the simulation results. This has happened due to a sudden change in direction of the flow of a jet of water while striking the blades of a runner. The density of the water and the sediment flowing along with it is different. In general, the density of sand and water is nearly 2650 kg/m^3 and 1000 kg/m^3 respectively. Therefore, Sand is 2.65 times heavier than water. When there is a sudden change in direction of water flow occurs, sand being a denser particle than water, it tends to continue to follow the same path rather than trained flow which is directed to a runner. As a result due to the higher rotational inertia of the sediment particles, they got separated from the water jet and particles ended up hitting blades number 5 and 6 as illustrated in Figure 5-24. It is spotted that the jet of the higher quantity of larger-sized particles (of 175 microns and above) hits the suction side and smaller sized particles below 175 microns of the blade number 6. It could have happened due to fact that the more the mass, the more the inertia. Bigger sized particle has a greater tendency to resist change in their state of motion which allows them to travel a longer distance than smaller sized particle does. The simulation also predicted that the water passing from beneath the guide vane possesses the highest velocity in the turbine. The sediments flowing along with the water strike the pressure side of blade number 26 resulting in significant erosion on its surface. The jet of water strikes blades number 4,3,2,1 and 30

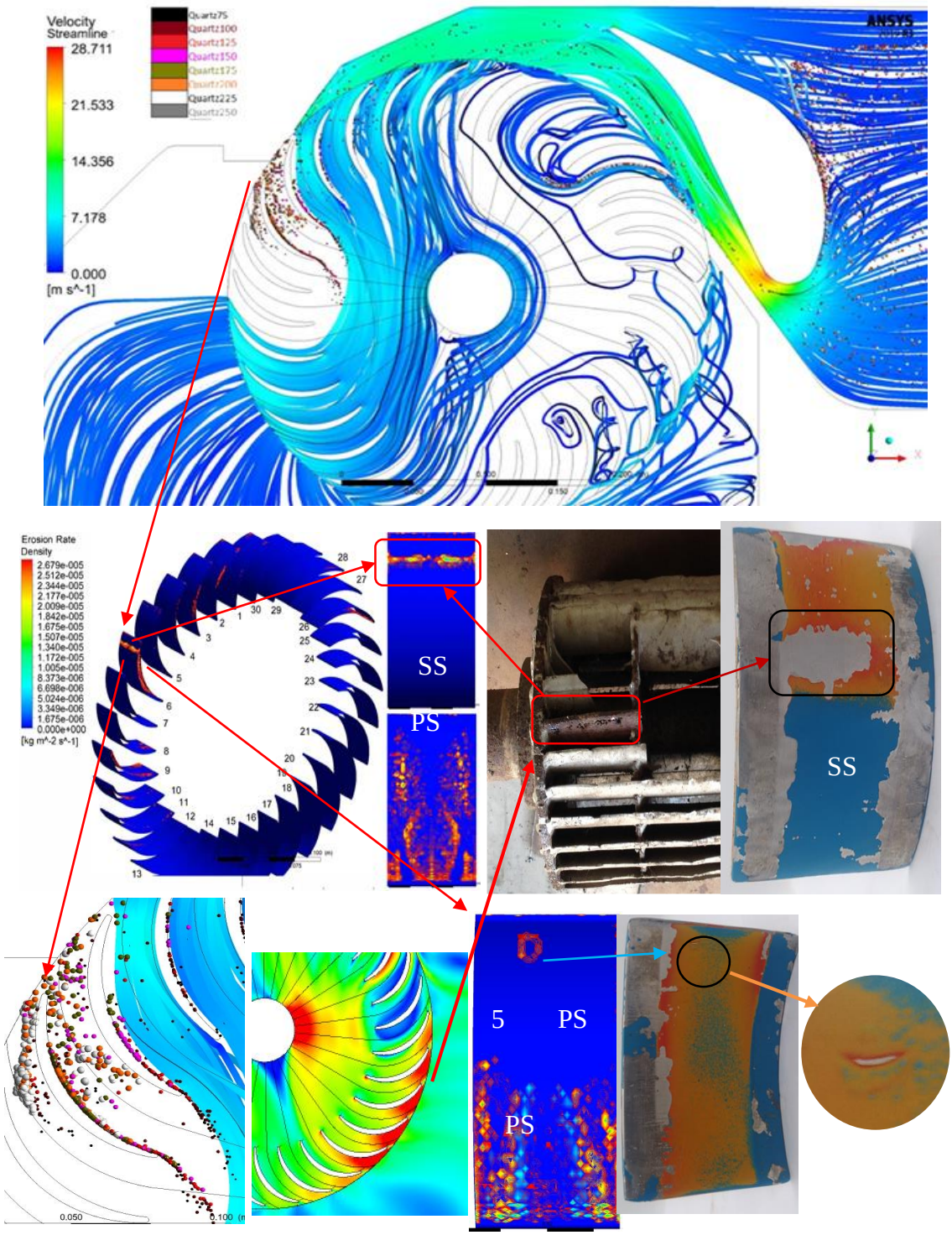

Figure 5-24: the result of CFD analysis, experiment and field observation

at first stage and from 9 to 14 at second stage. It can be seen that these blades are exposed to less erosion intensity. Scattered erosion spots are observed at the pressure side as indicated in Figure 5-25 (a) on both the stages blades. There are no traces of erosion on the suction side in the second stage blades. There are spots on either end of the blades at the leading edge of the suction side in all the first stage blades as indicated in Figure 5-25 (c) and (d).

There are not any traces of the effect of sediment on blade numbers from 15 to 24, 27 and 29 which is obvious as there is no water flow in these areas. The prediction of the simulation is based on a steady-state which is achieved at the end of a dynamic simulation as it reaches equilibrium. As the turbine rotates due to the impact of water along with sediment, every blade of the runner gets eroded in the same way.

The erosion can be anticipated through the erosion rate density (ERD) (kg/s/m^2) parameter in the numerical simulation. It is predicted that erosion on blade 6 alone contributes to 52.8 % of the total ERD. Similarly, blade 26 and 5 contributes to 11.36 % and 6.42 % respectively. Just three blades appear to account for 70.58 % of the runner's overall ERD.

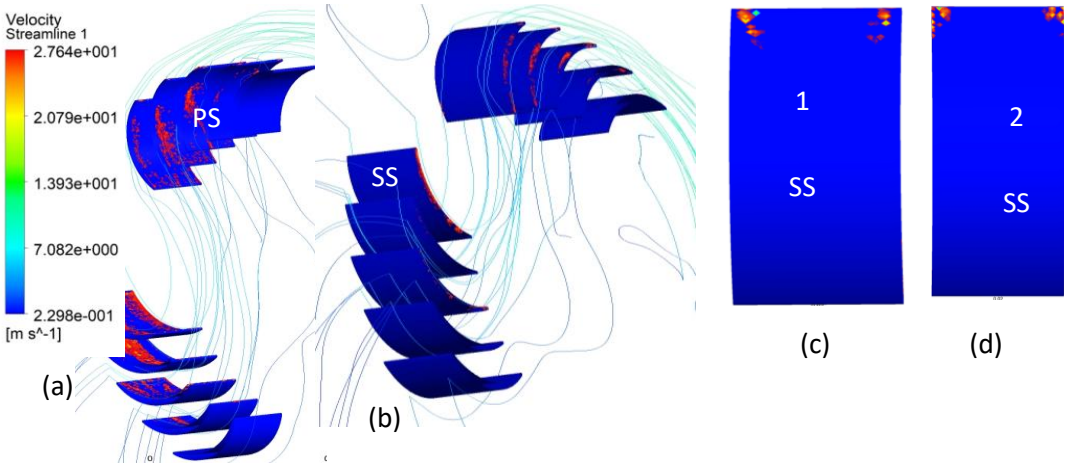

Figure 5-25: A view of First and second stage blades surface of (a) Pressure side (PS), (b) Suction side (SS), (c) blade 1 SS and (d) blade 2 SS

5.8.3. Amount of material loss

A total of five observations were made to observe the amount of weight loss on the test specimen. Experiments are done in two different operating conditions as specified in Table 5.11.

Table 5.11: Test performed introducing sediment in the test rig

S.N	Head (m)	Flowrate (l/s)	RPM	PPM	Guide vane (GV) Opening
Test 1	10	23	550	6000	31^o from full closing GV position (Full opening)
Test 2	10	15	357	15000	10^o from full closing GV position

The weights of the specimens were measured after an interval of 2 hours.

Figure 5-26 and Figure 5-27 show the observation of the weights of test specimens before and after each test run. It can be observed that the weight of all specimens are decreasing after every test run of 2 hours in both the tests. The removal of material in all test specimens are found to be in a linear trend. Regression analysis is used to predict abrasive erosion and its impact on the time of operation. The dependent variable is the weight of the specimen and the independent variable is the time of operation of the rig. For the analysis, the effective specimen width of 31 mm is considered. The useful life of the blade is generally considered till the weight of the runner is redued to half of it original weight. For Test 1, it is predicated, that the useful life of the blade is about 5 and half month of operation for test 1 and less than 3 months for test 2. It is estimated that the severity of abrasive erosion increased with increase in sediment concentration.

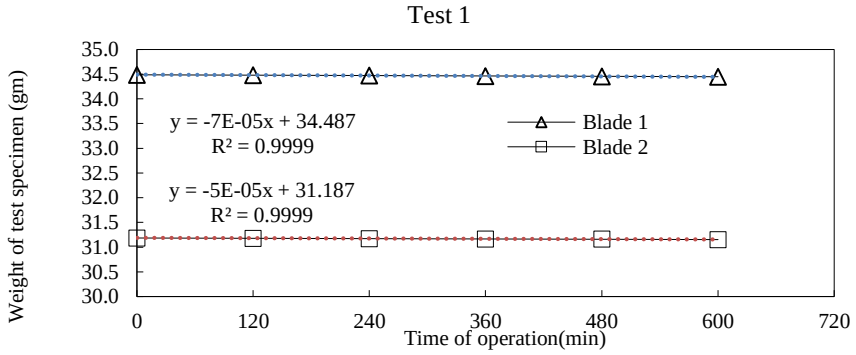

Figure 5-26: Combined weight of test specimens after each run in Test 1

Test 2

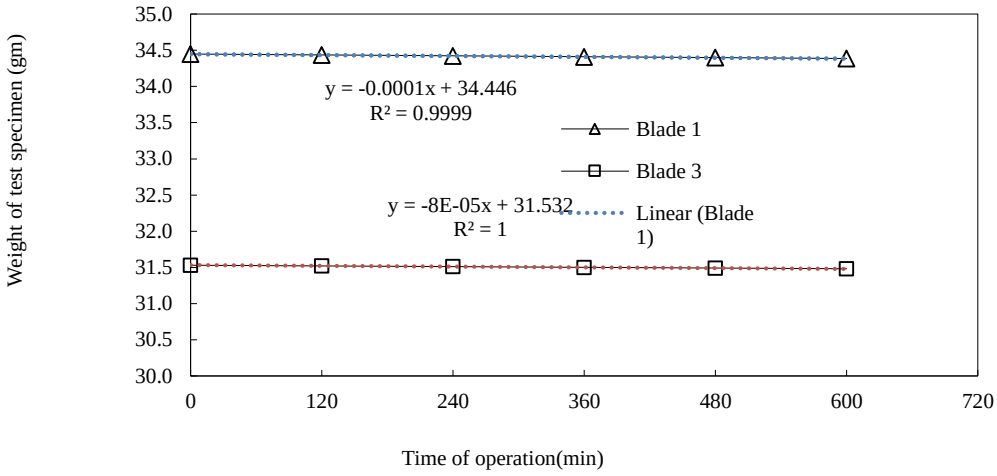

Figure 5-27: Combined weight of test specimens after each run in Test 2

It is very difficult to manufacture blades with identical weights. It varies due to manufacturing constraints and is unavoidable. A similar difference in weight can be observed in the test specimens while conducting present study as well which is evident through

Figure 5-26 and Figure 5-27. Therefore, analysis through the weight loss alone won't be enough as there are differences in the initial weight of the test specimens. Thus, there is a requirement to introduce the ratio of loss of weight in test specimens for comparison. The quantity is termed as amount of erosion is calculated using Eq. 3.2.

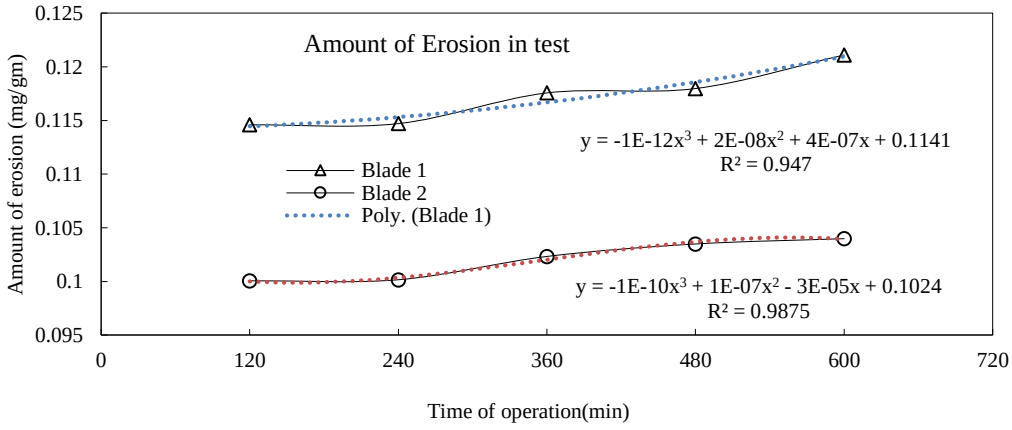

Figure 5-28: Amount of erosion in specimens in test 1

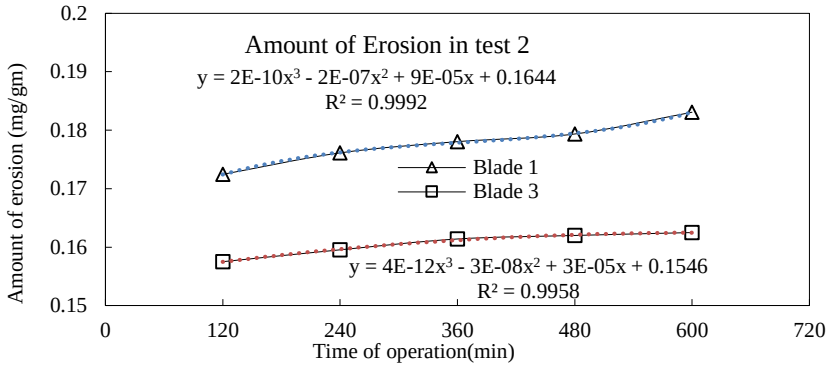

Figure 5-29: Amount of erosion in specimens in test 2

The amount of erosion has been estimated for both the tests and are illustrated in Figure 5-28 and Figure 5-29. There is a steady rise in the amount of erosion in all the test specimens. It is found that the amount of erosion in test 1 is higher than in test 2 in every interval of the test run.

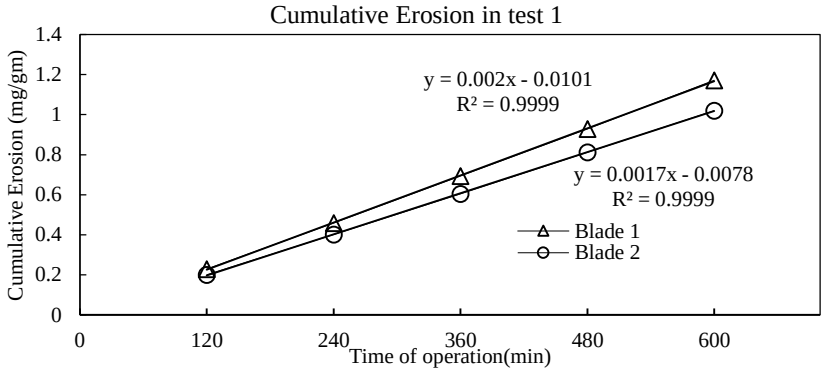

Figure 5-30: Cumulative erosion in specimens in Test 1

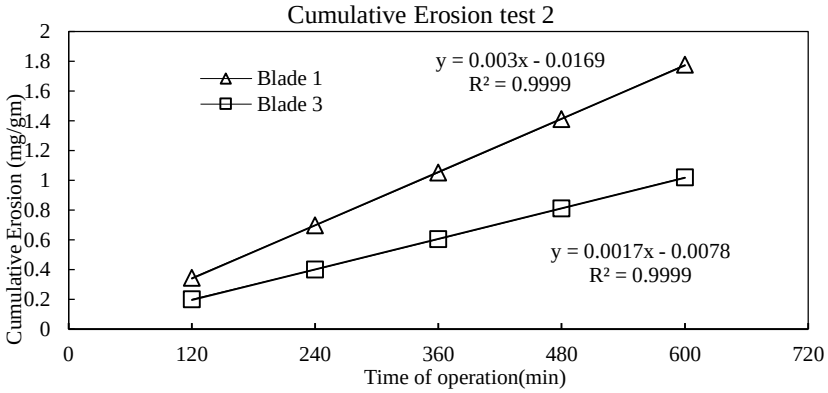

Figure 5-31: Cumulative erosion in specimens in Test 2

Furthermore, a comparison has been made with the ratio of the total weight loss. It is termed cumulative erosion and is expressed using Eq. 3.1. Figure 5-30 and

Figure 5-31 represents the estimation of the cumulative erosion of test specimen used in test 1 and test. It can be evaluated from the graphs that there is a steeper rise in erosion in test 2 compared to test 1 and total erosion in test 2 is significantly higher than that in test 1.

CHAPTER 6: CONCLUSION AND RECOMMENDATION

6.1. Conclusion

Studies have shown that runner water flow behaviour changes in response to changes in inlet beta angle of the runner blade. It is found that decreasing the inlet beta angle also decreases the sediment erosion effects along with improvement in efficiency to a certain degree (up to 16^{o}). However, going down from this value could, on one hand, reduce the sediment erosion problem but can also reduce the efficiency because of the fact that a lower inlet angle means the lower radius of curvature of the blade which induces flow separation and resulting low efficiency. Moreover, it is also observed that there is not much significant drop in the efficiency of the turbine with blade angles ranging from 16^{0} to 36^{0}. However, the sediment erosion effect is more significant at a higher beta angle.

The efficiency increased upon increasing the number of blades up to 35 and started decreasing once the number was increased more than that. This is because of the optimal flow passage created between the blades in a 35 blade runner.

It is also observed from the CFD analysis that the sediment erosion effect is more prominent in the second stage as there is a large relative velocity than that of the first stage. The velocity at the first stage is around 5 to 10 m/s while in the second stage, it rises gradually up and beyond 15 m/s. Furthermore, a small portion of the flow that is coming out of the guide vane disturb the main flow and thus would have created a favorable environment for erosion to occur.

The inspection of the eroded runner, numerical predictions and experimental results confirms that the blades of a runner got severely eroded due to the higher rotational inertia of the sediment particles, got separated from the water pathway while striking the blade.

6.2. Recommendations

It is observed that there is significant erosion in the ABS blade and it is almost not possible to quantify this erosion rate in the case of this runner. So, it is advised to use a runner made out of metal or alternatively all of the blades can be inserted in the plastic moulded endplates.

The severity of sediment erosion is reduced through optimizing beta angle. However, the runner should be optimized for another design parameter such as the shape of the nozzle, width of runner, angle of attack, inner blade angle, Inner to outer diameter rather than only outer blade angle and number of blades which will definitely have minimized the erosion effect to a very low value.

More investigations could be carried out to prevent the separation of sediment particles on first stage and prevent accumulating between first and second stage of CFT.

Injecting sediment into the system at a constant ppm during the test was a major challenge. It was necessary to stop multiple times in a single run of two hours to collect slurry from the peristaltic pump. It consumed an adequate amount of time to calculate ppm and restart the test again. Therefore, a real-time sediment monitoring system is needed.

References

[1] M. Adhikari, *Policy Discussion on "Integration of off-grid and on -grid electrification in Nepal : Challenges and Prospects"*, Patan: Alternative Energy Promotion Centre, 2014.

[2] Renewable Energy Data Book 2012, Patan: Government of Nepal, Alternative Energy Promotion Center, 12.

[3] "Nepal Micro Hydropower Development Association," NMHDA, [Online]. Available: http://www.microhydro.org.np/. [Accessed February 2015].

[4] K. B. Nakarmi, "Turbine and Drive system," Kathmandu, 2010.

[5] O. Shrestha, H. P. Neopane, B. Thapa and M. Shrestha, "Numerical analysis on effect of sizes of sand particle on Cross flow turbine," in *International Conference on ASIAN Community Knowledge Networks for the Economy, Society, Culture and Environmental Stability*, Kathmandu, 2015.

[6] G. D. Shepherd, Principles of turbomachinery, New York: Macmillan, 1956.

[7] F. Merryfield and C. A. Mockmore , The Banki Water Turbine, Engineering Experiment Station Bulletin No.25, 1949.

[8] K. Nakarmi, A. Arther, . R. Widmer and M. Eisenring, MHPG Series : Harnessing Water Power on a small scale ; volume 3 : Cross Flow Turbine Design and Equipment Engineering, SKAT, 1993.

[9] "The entec Cross Flow Turbine T15," entec Consulting & Engineering, St. Gallen.

[10] L. Haimerl, *The cross-flow turbine.*, Water Power Engineering Magazine, 1960.

[11] M. Durali, Design of small water turbines for farms and small communities, Tehran: MASSACHUSETTS INSTITUTE OF TECHNOLOGY, 1976.

[12] J. Fukutomi, Y. Nakase and T. Watanabe, "A Numerical Method of Free Jet from a Cross-flow Turbine Nozzle.," *Bulletin od JSME,* vol. 28, no. 241, pp. 84-119, 1985.

[13] S. Khosrowpanah, A. A. Fluzat and M. L. Albertson, "Experimental study of Cross flow turbine," *J. Hydraul. Div., Am. Soc. Civ. Eng.; (United States,* vol. 114, no. 3, pp. 299- 314, 1988.

[14] N. M. Aziz and V. R. Desai, "An experimental study of the effect of some design parameters on cross-flow turbine efficiency," Department of Civil Engineering, Clemson University, Clemson, 1991.

[15] W. Fay and W. Durgin, Small Hydro Power Machinery,, 1984.

[16] A. Fiuzat and B. Akerkar, "The use of interior guide tube in cross flow turbines," vol. 2, p. 89, 1989.

[17] V. R. Desai and N. Aziz, "An Experimental Investigation of Cross-flow Turbine Efficiency," *Journal of Fluids Enfineering,* vol. 116, pp. 545 - 550, 1994.

[18] H. G. Totapally and N. M. Aziz, "Refinement of Cross-flow turbine design parameters," *Journal of Energy Engineering,* vol. 120, no. 3, pp. 133 - 147, 1994.

[19] N. Y. Fukutomi and T. Watanabe, "A study of the cross-flow turbine, effects of nozzle shape on its performance.," *Small hydro-power fluid machinery, American Society of Mechanical Engineers,* pp. 129-133, 1982.

[20] S. Khosrowpanah, Experimental study of the cross flow turbine, Fort Collins: Colorado State University, 1984.

[21] W. W. Durgin and W. K. Fay, "Some fluid flow characteristics of a Cross flow type hydraulic turbine," pp. 77-93.

[22] A. Abbas, A. Fiuzat and B. Akerkar, "Power outputs os two stages of cross-flow turbine," *Journal of energy engineering,* no. 117, 1991.

[23] C. B. Joshi, V. Seshadri and S. N. Singh, "Parametric study on performance of Cross-flow turbine," *Journal oj Energy Engineering,,* vol. 121, no. 1, pp. 28- 45, 1995.

[24] N. H. Costa Pereira and J. E. Borges, "Study of the nozzle flow in a cross-flow turbine.," *Internation Journal of Mechanical Sciences,* no. 38(3), 1996.

[25] H. Reddy, V. Seshadri and D. P. Kothari, "Effect of Draft Tube Size on the Performance of a Cross-Flow Turbine," *Energy Sources,* vol. 18, no. 2, pp. 143-149, 1995.

[26] H. Olgun, "Investigation of the performance of Cross-flow turbine," *International Journal of Energy Research,* vol. 22, pp. 953-964, 1998.

[27] H. Olgun, "Effect of interior guide tubes in cross-floow turbine runner on turbine performance," *International Journal of Energy Research,* vol. 24, pp. 953-964, 2000.

[28] E. C. Walseth, Investigation of the Flow through the Runner of a Cross-Flow Turbine, Trondheim: NTNU, 2009.

[29] Y.-D. Choi, J.-I. Lim, Y.-T. Kim and Y.-H. Lee, "Performance and Internal flow characterstics of a Cross-Flow Hydro Turbine by Shape of Nozzle and Runner Blade.," *Journal of Fluid science and technology,* vol. 3, pp. 398-409, 2008.

[30] J. D. Andrade, C. Curiel, F. Kenyery, O. Aguillon, A. Vasquez and M. Asuaje, "Numerical Investigation of the Internal Flow in a Banki Turbine," *International Journal of Rotating Machinery,* vol. 2011, no. 841214, pp. 1-12, 11.

[31] V. Sammartano, O. Fecarotta, A. Carravetta and C. Aricò, "Banki-Michell Optimal Design by Computational Fluid," *energies,* p. 24, april 2013.

[32] Z. Chen and Y. D. Choi, "Influence of air supply on the performance and internal flow characteristics of a cross flow turbine," *Renewable Energy,* vol. 9, pp. 103-110, 2014.

[33] S. D. Croquer, J. d. Andrade and J. Clarembaux, "Use of CFD tools in internal deflector design for Cross flow turbine efficiency improvement," in *Proceedings of the ASME 2012 Fluids Engineering Summer Meeting FEDSM2012*, Rio Grande, Puerto Rico, 2012.

[34] K. Kokubu, T. Kanemoto, S. W. Son and Y. D. Choi, "Performance Improvement of a Micro Eco Cross-Flow Hydro Turbine," *Journal of the Korean Society of Marine Engineering,*, vol. 36, no. 7, pp. 902-9090, 2012.

[35] N. Acharya, C. G. Kim, B. Thapa and Y. H. Lee, "Numerical analysis and performance enhancement of a cross-flow hydro turbine," *Renewable Energy,* vol. 80, pp. 819-826, 2015.

[36] R. C. Adhikari, J. Vaz and D. Wood, "Cavitation Inception in Crossflow Hydro Turbines," *Energies* , vol. 9, no. 237, pp. 1-12, 2016.

[37] S. Chichkhede, V. Verma, V. K. Gaba and S. Bhowmick, "A simulation based study of flow velocities across cross flow turbine at different nozzle openings," *ScienceDirect,* vol. 25, pp. 974-981, 2016.

[38] C. V. Duan and V. Y. Karelin, Abrasive Erosion and Corrosion of Hydraulic Machinery, International Research Center on Hydraulic Machinery, 2003.

[39] M. E. Henriksen, Sediment erosjion in Francis turbines, Trondheim: Norwegian University of Science and Technology (NTNU), 2013.

[40] E. Bak, "Construction materials and testing results of the wear of pumps for transporting solid media," *Biuletyn Glownego Instytuta Gornictwa*, vol. 12, 1966.

[41] P. Bergeron and J. Dollfus, "The influence of the nature of the pumped mixture and hydraulic characteriscs on the design and installation of liquid/solid mixture pumps," in *Proc. 5th Conf. on Hydraulics Turbines et Pompes Hydrauliques*, 1958.

[42] A. G. Bain and S. T. Bonnington, "The hydraulic transport of solids by pipeline," *1st ed. Oxford: Pergamon Press,,* pp. 131-136, 1970.

[43] B. K. Gandhi, S. N. Singh and V. Seshadri, "Study of the parametric dependence of erosion wear for the parallel flow of solid-liquid mixtures," *Tribol Int,* pp. 275-282, 1999.

[44] B. Naidu, "Addressing the problems of silt erosion at hydro plants,"," *Hydropower & Dams,* vol. 3, pp. 72-77, 1997.

[45] K. Gjøsæter, "Hydraulic Design of Francis Turbine Exposed to Sediment Erosion," Waterpower laboratory,NTNU, Trondheim, 2011.

[46] J. B. Zu, I. M. Hutchings and G. T. Burstein, "Design of a slurry erosion test rig," *Wear,* vol. 140, pp. 331-344, 1990.

[47] A. Abouel-Kasem, Y. M. Abd-elrhman, K. M. Emara and S. M. Ahmed, "Design and Performance of Slurry Erosion Tester," *Journal of Tribology,* vol. 132, no. 2, p. 021601–021610, 2010.

[48] H. C. Lin, S. K. Wc and C. H. Yeh, "A comparison of slurry erosion characteristics of TiNi shape memory alloys and SUS304 stainless steel," *Wear,* vol. 249, no. 7, pp. 557-565, 2001.

[49] G. T. Burstein and k. Sasaki, "Effect of Impact Angle on the Slurry Erosion Corrosion of 304L Stainless Steel," *Wear,* vol. 240, pp. 80-94, 2000.

[50] A. K. Chauhan, D. B. Goel and S. Prakash, "Erosion behaviour of hydro turbine steels," *Bulletin of Materials Science ,* vol. 31, no. 2, pp. 115-120, 2008.

[51] T. R. Bajracharya, B. Acharya, C. B. Joshi, R. P. Saini and O. G. Dahlhaug, "Sand erosion of Pelton turbine nozzles and buckets: A case study of Chilime hydropower plant," *Wear,* vol. 264, no. 3-4, pp. 177-184, 2008.

[52] A. K. Rai, A. Kumar and T. Staubli, "Developing a Test Rig To Measure Hydro-Abrasive Erosion in Pelton Turbine," in *International Conference in Hydropower Sustainable Development,*, Dehradun, 2015.

[53] B. Thapa and Brekke, "Effect of sand particle size and surface curvature in erosion of hydraulic turbine," in *IAHR Symposium on Hydraulic Machinery and Systems,*, Stockholm, 2004.

[54] H. S. Grewal, A. Agrawal and H. Singh, "Slurry erosion mechanism of hydroturbine steel: Effect of operating parameters.," *Tribology,* vol. 52, p. pages287–303, 2013.

[55] S. Khurana, V. Goel and A. Kumar, "Effect of silt particles on erosion of Turgo impulse turbine blades," *International Journal of Ambient Energy,* vol. 35, no. 3, pp. 155-162, 2014.

[56] M. K. Padhy and R. P. Saini, "Study of silt erosion mechanism in Pelton turbine buckets.," *Energy,* vol. 39, no. 1, pp. 286-293, 2012.

[57] B. K. Gandhi, S. N. Singh and V. Seshadri, "A study on the effect of surface orientation on erosion wear of flat specimens moving in a solid-liquid suspension," *Wear,* vol. 254, p. 1233–1238, 2003.

[58] R. Gupta and V. Sehadri, "Prediction of uneven wear in a slurry pipeline on the basis of measurements in a pot tester," *Wear,* vol. 184, p. 169–178, 1995.

[59] S. Lathabai and D. Pender, "Microstructural influence in slurry erosion of ceramics," *Wear,* vol. 189, no. 1-2, pp. 122-135, 1995.

[60] A. A. gadhikar, A. Sharma, D. B. Goel and C. P. Sharma, "Fabrication and testing of slurry pot erosion tester," *Transactions of the Indian Institute of Metal,* vol. 64, p. 493–500, 2001.

[61] R. N. Sharma and A. A. Shaikh, "Solids suspension in stirred tanks with pitched blade turbines," *Chemical Engineering Science,* vol. 58, no. 10, pp. 2123-2140, 2003.

[62] F. Y. Lin and H. S. Shao, "Effect of Impact Velocity on Slurry Erosion and a New Design of a Slurry Erosion Tester," *Wear,* vol. 143, no. 2, p. 231–240, 1991.

[63] M. A. AL-Bukhaiti, S. M. Ahmen, F. Badran and K. M. Emara, "Effect of impingement angle on slurry erosion behavior and mechanisms of 1017 steel and high-chromium white cast iron," *Wear,* vol. 262, pp. 1187-1198, 2007.

[64] J. J. Tuzson, "Laboratory slurry erosion tests and pump wear rate calculations," *Journal of Fluids Engineering,* vol. 106, no. 2, p. 135–140, 1984.

[65] H. Clark, J. Tuzon and K. K. Wong, "Measurement of specific energies for erosive wear using a Coriolis erosion tester," *Wear,* vol. 241, no. 1, p. 1–9, 2000.

[66] R. J. Llewellyn, S. K. Yick and K. F. Dolman, "Scouring erosion resistance of metallic materials used in slurry pump service," *Wear,* vol. 256, p. 592–599, 2004.

[67] C. I. Walker and P. Robbie, "Comparison of some laboratory wear tests and field wear in slurry pumps," *Wear,* vol. 302, p. 1026–1034, 2013.

[68] B. S. Maan, "High-energy particle impact wear resistance of hard coatings and their application in hydroturbines," *Wear,* vol. 237, no. 1, p. 140–146, 200.

[69] B. S. Mann, V. Arya, A. K. Maiti, M. Rao and P. Joshi , "Corrosion and erosion performance of HVOF/TiAlN PVD coatings and candidate materials for high pressure gate valve application," *Wear,* vol. 260, p. 75–82, 2006.

[70] D. W. Wheeler and R. Wood, "Erosion of hard surface coatings for use in offshore gate valves," *Wear,* vol. 258, p. 526–536, 2005.

[71] S. Dallaire, "Hard arc-sprayed coating with enhanced erosion and abrasion wear resistance," *Journal of Thermal Spray Technology,* vol. 10, no. 3, pp. 511-519, 2001.

[72] "Slurry wear and cavitation erosion of thermal-sprayed cermets," *Wear,* vol. 258, p. 768–775, 2005.

[73] "Influence of impact angle of solid particles on erosion by slurry jet," *Wear,* vol. 265, p. 713–720, 2008.

[74] C. N. Machio, G. Akdogan, M. J. Witcomb and S. Witcomb, "Performance of WC–VC–Co thermal spray coatings in abrasion and slurry erosion tests," *Wear,* vol. 258, p. 434–442, 2005.

[75] R. C. Shivamurthy, M. Kamaraj, R. Nagarajan, S. M. Shariff and G. Padmanabham, "Influence of microstructure on slurry erosive wear characteristics of laser surface alloyed 13Cr–4Ni steel," *Wear,* vol. 267, p. 204–212, 2009.

[76] R. C. Shivamurthy, M. Kamaraj, R. Nagarajan, S. M. Shariff and G. Padmanabham, "Slurry erosion characteristics and erosive wear mechanisms of Co-based and Ni-based coatings formed by laser surface alloying.," *Metallurgical and Materials Transactions A,* vol. 14A, p. 470–486, 2010.

[77] "Slurry erosion studies on surface modified 13Cr–4Ni steels: effect of angle of impingement and particle size," *Journal of Materials Engineering and Performance,* vol. 16, no. 5, p. 567–572, 2007.

[78] J. F. Santa, J. C. Baena and A. Toro, "Slurry erosion of thermal spray coatings and stainless steels for hydraulic machinery," *Wear,* vol. 263, p. 258–264, 2007.

[79] J. F. Santa, L. A. Espitia, J. A. Blanco, S. A. Romo and A. Toro, "Slurry and cavitation erosion resistance of thermal spray coatings," *Wear,* vol. 267, p. 160–167, 2009.

[80] J. Yoganandh, S. Natarajan and S. K. Babu, "Erosive wear behavior of nickel-based high alloy white cast iron under mining conditions using Orthogonal Array," *Journal of Materials Engineering and Performance,* vol. 22, p. 534–2541, 2013.

[81] Q. B. Nguyen, C. Y. Lim, V. B. Nguyen, Y. M. Wan, B. Nai, Y. W. Zhang and M. Gupta, "Slurry erosion characteristics and erosion mechanisms of stainless steel.," *Tribology International,* vol. 79, pp. 1-7, 2014.

[82] G. T. Burstein and K. Sasaki, "Effect of impact angle on the slurry erosion–corrosion of 304L stainless steel," *Wear,* vol. 240, p. 80–94, 2000.

[83] M. C. Lin, L. S. Chang, H. C. Lin, C. H. Yang and K. M. Lin, "A study of high-speed slurry erosion of NiCrBSi thermal-sprayed coating," *Surface and Coatings Technology,* vol. 201, no. 6, pp. 3193-3198, 2006.

[84] B. Thapa, Sand erosion in hydraulic machinery, Norway: Norwegian University of Science and Technology, 2001.

[85] T. R. Bajracharya, Correlation between sand led erosion of Pelton buckets and efficiency losses in high head hydropower scheme, Patan: Intitute of Engineering,Tribhuvan University, 2007.

[86] M. K. Padhy and R. P. Saini, "Effect of size and concentration of silt particles on erosion of Pelton turbine buckets," *Energy,* vol. 34, no. 10, pp. 1477-1483, 2009.

[87] M. K. Padhy and R. P. Saini, "Study of silt erosion on performance of a Pelton turbine," *Energy,* vol. 36, no. 1, pp. 141-147, 2011.

[88] J. Liu, L. Lu and L. Zhu, "Experiment study on sediment erosion of Pelton turbine flow passage component material," in *IOP Conference Series: Earth and Environmental Science*, Beijing, 2012.

[89] B. R. Karnikar, H. P. Neopane and B. S. Thapa, "Development of rotating disc apparatus for test of sediment-induced erosion in Francis runner blades," *Wear,* vol. 306, no. 1-2, p. 119–125, 2013.

[90] H. S. Grewal, S. Bhandari and H. Singh, "Parametric study of slurry-erosion of hydro turbine steels with and without detonation gun spray coatings using Taguchi technique," *Metallurgical and Materials Transactions A,* vol. 43A, p. 3387–3401, 2012.

[91] H. S. Grewal, A. Agrawal and H. Singh, "Design and development of high-velocity slurry erosion test rig using CFD," *Journal of Materials Engineering and Performance,* vol. 22, pp. 152-161, 2013.

[92] H. S. Grewal, A. Agrawal, H. Singh and B. A. Shollock, "Slurry erosion performance of Ni–Al2O3 based thermal-sprayed coatings: effect of angle of impingement," *Journal of Thermal Spray Technology volume,* vol. 23, p. 389–401, 2014.

[93] A. K. Rai and T. Staubli, "Effect of concentration and size of sediments on hydro-abrasive erosion of PeltonTurbine," *Renewable Energy,* vol. 145, pp. 893-902, 2020.

[94] M. Kjeldsen, "Diploma Thesis," Norwegian Institute of Technology, 1991.

[95] M. Knutsen, NTNU, Norway, 1997.

[96] G.M. Wood, L.K. Knudsen, F.G. Hammitt, "Cavitation damage studies with rotating disc in water," *Journal of Basic Engineering,* pp. 98-110, 1967.

[97] A. Shima, H. Tomaru, A. Ihara, N. Miura, "Cavitation damage study with a rotating disk at the high peripheral velocities," *Journal of Hydraulic Research,* vol. 30, no. 4, pp. 521-538, 1992.

[98] B. Mann, "Boronizing of cast martensitic chromium nickel stainless steel and its abrasion and cavitation-erosion behavior," *Wear,* vol. 208, pp. 125-131, 1997.

[99] B. Mann, "High-energy particle impact wear resistance of hard coatings and their application in hydroturbines," *Wear,* vol. 237, no. 1, pp. 140-146, 2000.

[100] B. Thapa, P. Chaudhary, O.G. Dahlhaug, P. Upadhyay, "Study of combined effect of sand erosion and cavitation in hydraulic turbines," in *International Conference on Small Hydropower-Hydro Sri Lanka,* Sri Lanka, 2007.

[101] O. Shrestha, N. Acharya, B. Thapa, H.P. Neopane, Y.H. Lee, "Design and Development of Rotating Disc Apparatus to Test Sediment Erosion in Cross Flow Turbine Runner Blades," in *Proceedings of the International Symposium on Current Research in Hydraulic Turbines,* Turbine Testing Lab, Kathmandu University, Dhulikhel, Nepal, 2016.

[102] R. Koirala, . H. P. Neopane, O. Shrestha, B. Zhu and B. Thapa, "Selection of guide vane profile for erosion handling in Francis Turbines," *Renewable Energy,* vol. 112, pp. 328-336, 2017.

[103] R. Gantawa, N.K. Tamrakar, "Analysis of sediment abrasion potential in hydro turbines by studying fine sediments from the Budhi Gandaki-Trishuli River of Nepal," *Journal of Nepal Geological Society,* vol. 58, pp. 29-38, 2019.

[104] M. K. Sung, "A Study on CFD Analysis and Model Experiment for Cross-flow Turbine to Protect Sediment Erosion," Korea Maritime and Ocean University, Busan, 2018.

[105] J. H. Park, d. h. Lee, S. J. Cha and Y. H. Lee, "Development of a sediment Erosion-Proof Micro Class Cross-Flow Hydro Turbine," in *Precedings of the International Symposium on Current Research in Hydraulic Turbines*, Dhulikhel, 2016.

[106] J. Zahavi, G.F. Schmitt, "Solid particle erosion of polymer coatings," *Wear,* vol. 71, pp. 191-210, 1981.

[107] A. KC, B. Thapa and Y. H. Lee, "Transient numerical analysis of rotorestator interaction in a Francis turbine," *Renewable Energy,* vol. 65, pp. 277-235, 2014.

[108] N. Acharaya , C. G. Kim, B. Thapa and Y. H. Lee, "Numerical analysis and performance enhancement of a cross-flow hydro turbine," *Renewable Energy,* pp. 1-8, 2015.

[109] I. b. Celik, U. Ghia, P. J. Roache, C. J. Freitas, H. Coleman and P. E. Raad, "Procedure for Estimation and Reporting of Uncertainty Due to Discretization in CFD applications," *Journal of Fluids Engineering*, vol. 130, no. 7, pp. 0780011-0780014, 2008.

[110] J. F. Pietranski, "Mechanical Agitator Power Requirements for Liquid Batches," 2012.

[111] M. Antunes and R. A. Medronho, Bradley Hydrocyclones: Design and Performance Analysis, Springer Science+Business Media Dordrecht, 1992.

[112] "Hydraulic turbines, storage pumps and pump-turbines-Model acceptance tests," International Electrotechnical Commision. IEC 60193, Geneva, 1999.

[113] R. E. Walpole, R. H. Myers, S. L. Myers and K. Ye, Probability & Stastics For Engineers and Scientist, pearson Interational Edition ed., Pearson Education International, 2012.

[114] P.-T. S. Storli, Modelltest av Francis Turbin i Vannkraftlaboratoriet ved NTNU, Trondheim: NTNU, 2006.

[115] E. C. Walseth and S. O. Danielsen, Virkningsgradmåling av cross-flow turbin. Project at, Trondheim: NTNU, 2008.

Appendix A: List of Publications

- **Oblique Shrestha,** Hari Prasad Neopane, BholaThapa, Young-Ho Lee, Aman Kapali, "Rotating Disc Apparatus and its application to estimate sediment erosion in Hydro turbines“ International Journal of Scientific Research in Science and Technology (IJSRST), Online ISSN : 2395-602X, Print ISSN : 2395- 6011, Volume 8 Issue 6, pp. 348-358, November- December 2021.
- **Oblique Shrestha**, Aman Kapali, Bhola Thapa, Hari Prasad Neopane, Young- Ho Lee," Experimental study of Crossflow turbine under different operating conditions” IAHR-Asia 2021 Symposium on Hydraulic Machinery and Systems, 22nd – 23rd November, Kathmandu, Nepal
- Aman Kapali, Hari Prasad Neopane, Sailesh Chitrakar, Atmaram Kayastha, **Oblique Shrestha** Series: Journal of Physics: Conf. Series 1 1608 (2020) 012014“Experimental and CFD study of influence of sediment size on efficiency of hydro cyclone for use as sediment separation device" IOP Conference
- Aman Kapali, Sailesh Chitrakar, **Oblique Shrestha**, Hari Prasad Neopane and Biraj Singh Thapa, “A Review on Experimental Study of Sediment Erosion in Hydraulic Turbines at Laboratory Conditions”, IOP Conference Series: Journal of Physics: Conf. Series 1266 (2019) 012016
- Nirmal Acharya, Hari Prasad Neopane, **Oblique Shrestha**, Atmaram Kayastha Young-Ho Lee," Design & Development of Cross-flow Turbine Test Rig at Turbine Testing Lab for Better Sediment Handling", International Symposium on Current Research in Hydraulic Turbines, Volume 8, 20 March, 2018, Dhulikhel, Nepal
- Ravi Koirala , Hari Prasad Neopane , **Oblique Shrestha**, Baoshan Zhu, Bhola Thapa," Selection of guide vane profile for erosion handling in Francis turbines", Renewable Energy, Volume 112, November 2017, Pages 328–336, http://dx.doi.org/10.1016/j.renene.2017.05.033
- **Oblique Shrestha**, Nirmal Acharya, Bhola Thapa, Hari Prasad Neopane, Young- Ho Lee," Development of Cross flow Turbine Test Rig at Turbine Testing Lab ", International Symposium on Current Research in Hydraulic Turbines, Volume 7, 4 April, 2017, Dhulikhel, Nepal
- **Oblique Shrestha**, Nirmal Acharya, Atmaram Kayastha, Bhola Thapa, Hari Prasad Neopane, Young- Ho Lee," Design and Development of Rotating Disk Apparatus to Test Sediment Erosion in Cross Flow turbine Runner Blades", International Symposium on Current Research in Hydraulic Turbines, Volume 6, 14 March, 2016, Dhulikhel, Nepal
- Nirmal Acharya, **Oblique Shrestha**, Bhola Thapa, Hari Prasad Neopane, Young- Ho Lee," Performance analysis of 5 kW cross-flow turbine with insertion of air layer effect", International Symposium on Current Research in Hydraulic Turbines, Volume 6, 14 March, 2016, Dhulikhel, Nepal
- **Oblique Shrestha**, Hari Prasad Neopane, Bhola Thapa, Mausam Shrestha, "Numerical analysis on effect of sizes of sand particle on Crossflow turbine", International Conference on ASIAN Community Knowledge Networks for the

Economy, Society, Culture and Environmental Stability, Volume 11, 30 March - 03 April, 2015, Kathmandu, Nepal.

- Binaya Baidar, **Oblique Shrestha**, Hari Prasad Neopane, "An LCA approach in analyzing environmental sustainability and policy making of a typical micro - hydro power plant in Nepal", International Conference on ASIAN Community Knowledge Networks for the Economy, Society, Culture and Environmental Stability, Volume 11, 30 March - 03 April, 2015, Kathmandu, Nepal.

Appendix B: Manufacturing drawings of RDA

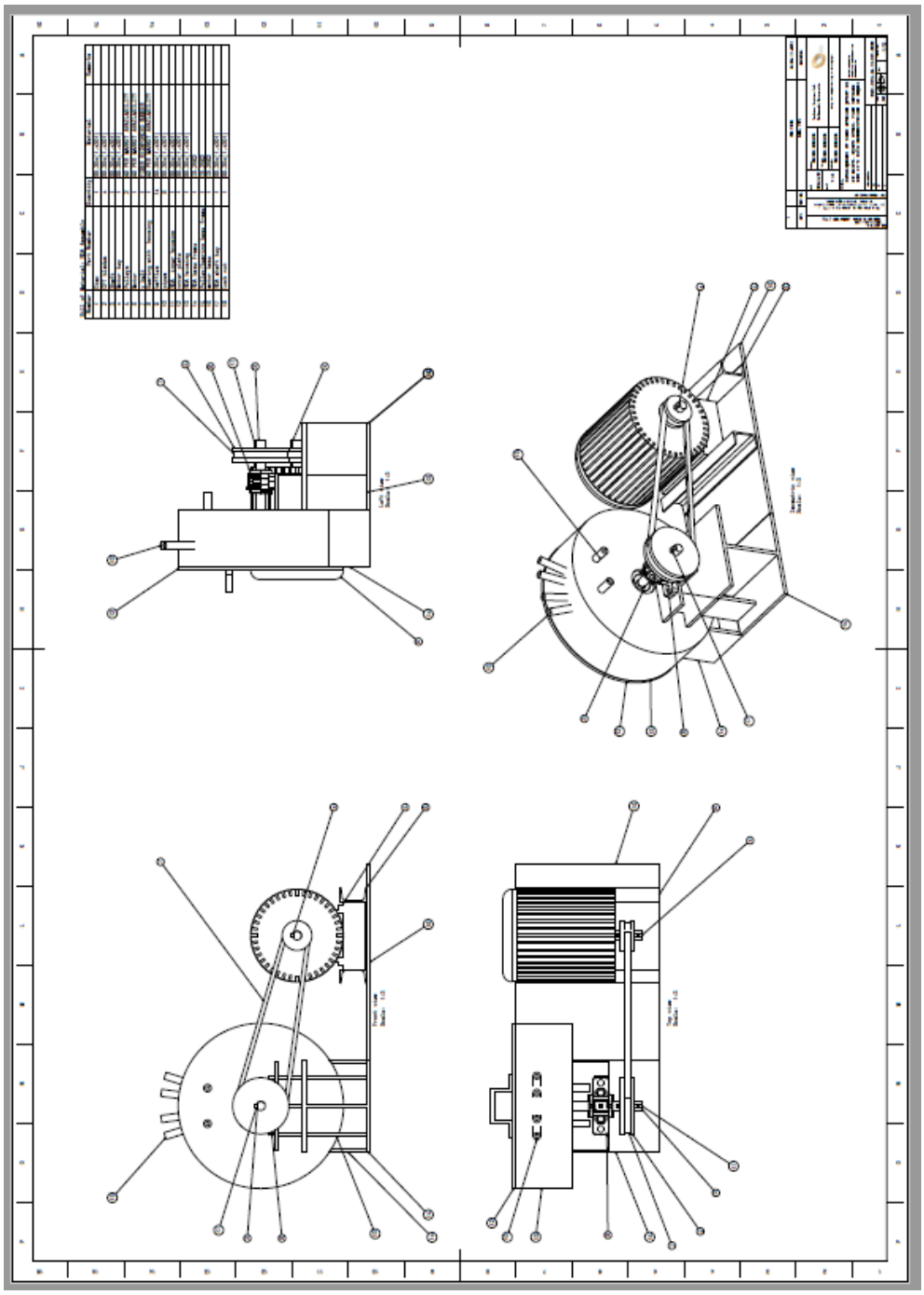

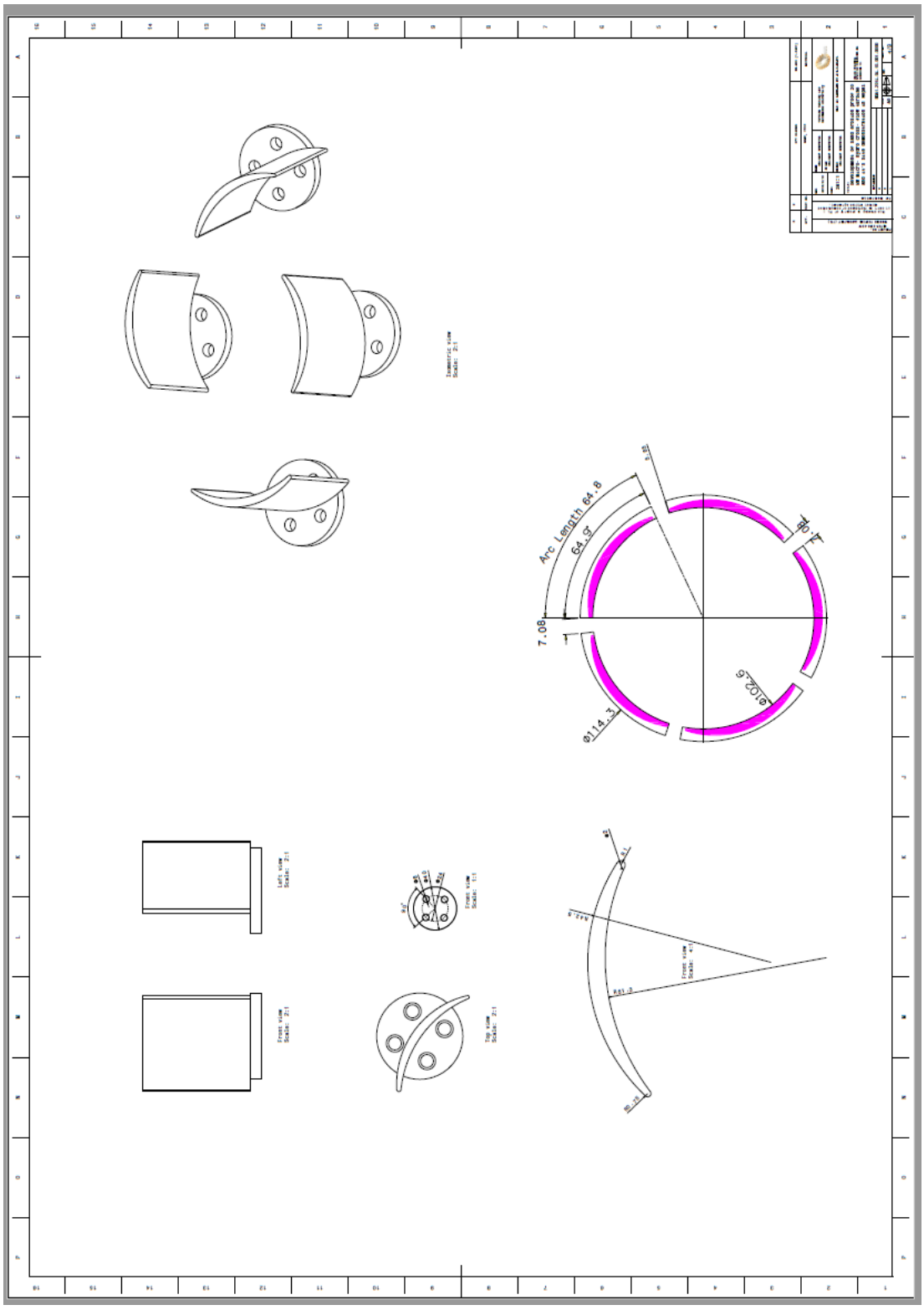
Arc Length 64.8
64.5
7.08
Ø102.6
Ø114.3
Left view
Scale: 2:1
Front view
Scale: 2:1
Top view
Scale: 2:1
Front view
Scale: 1:1
Front view
Scale: 1:1

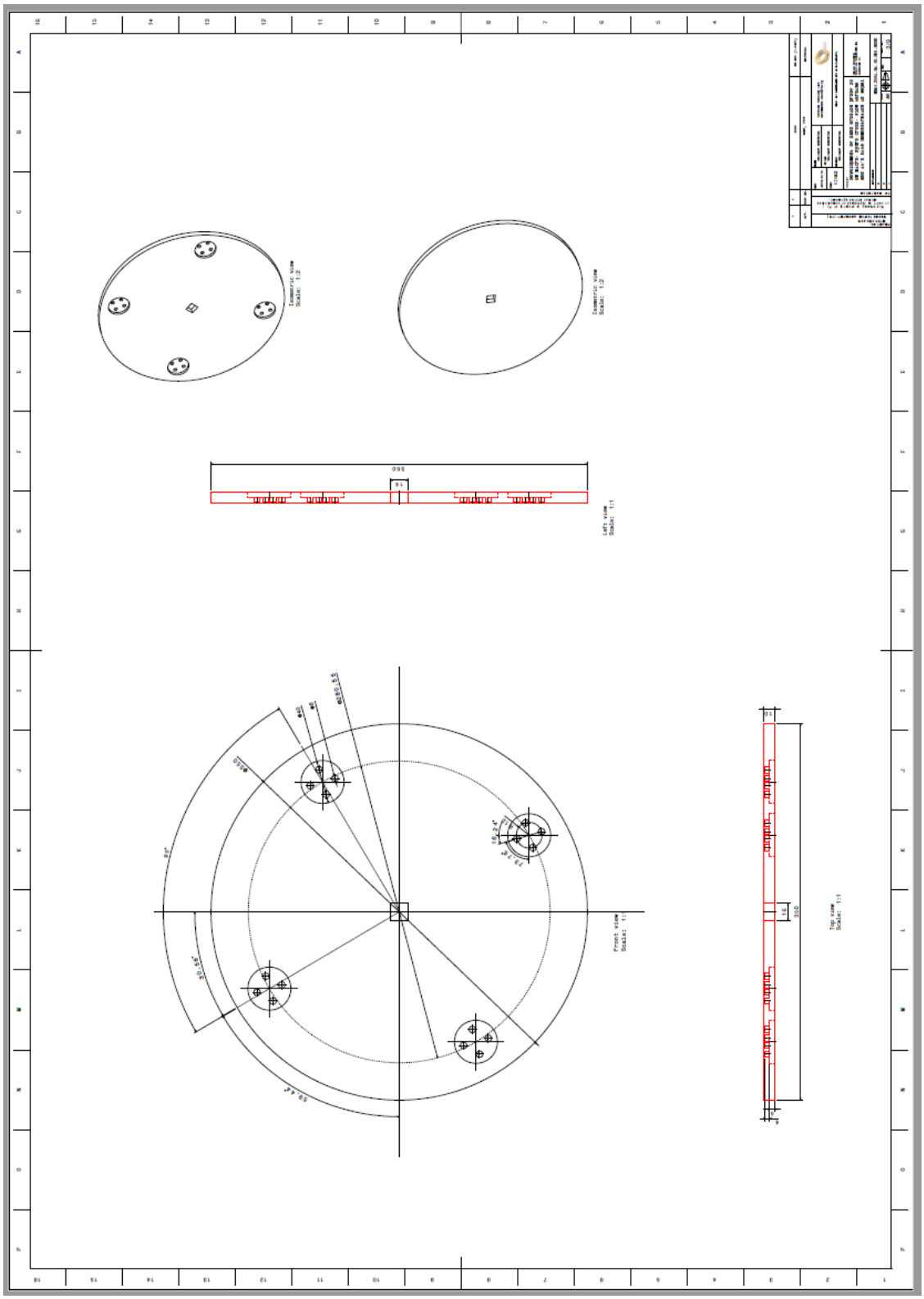

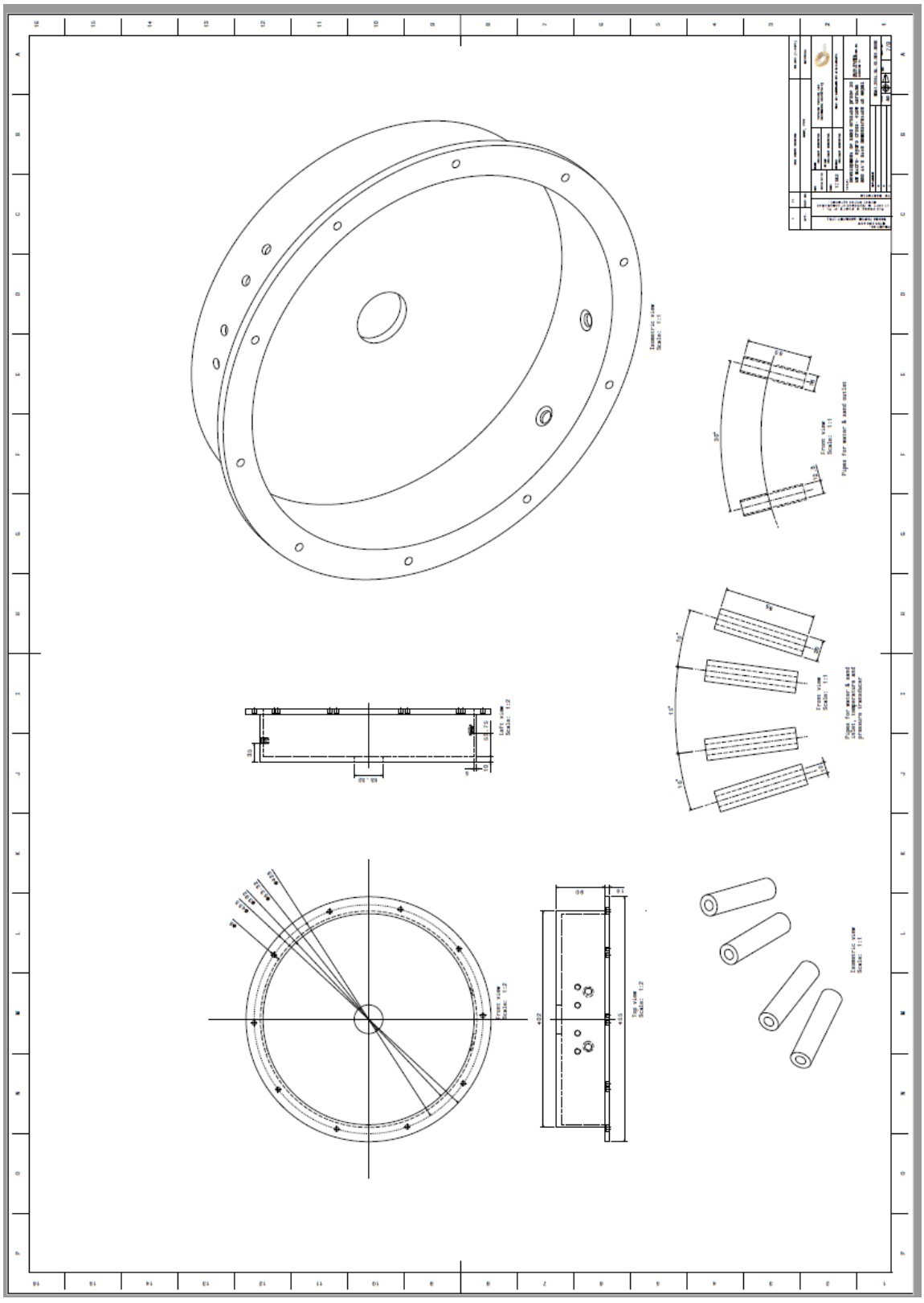

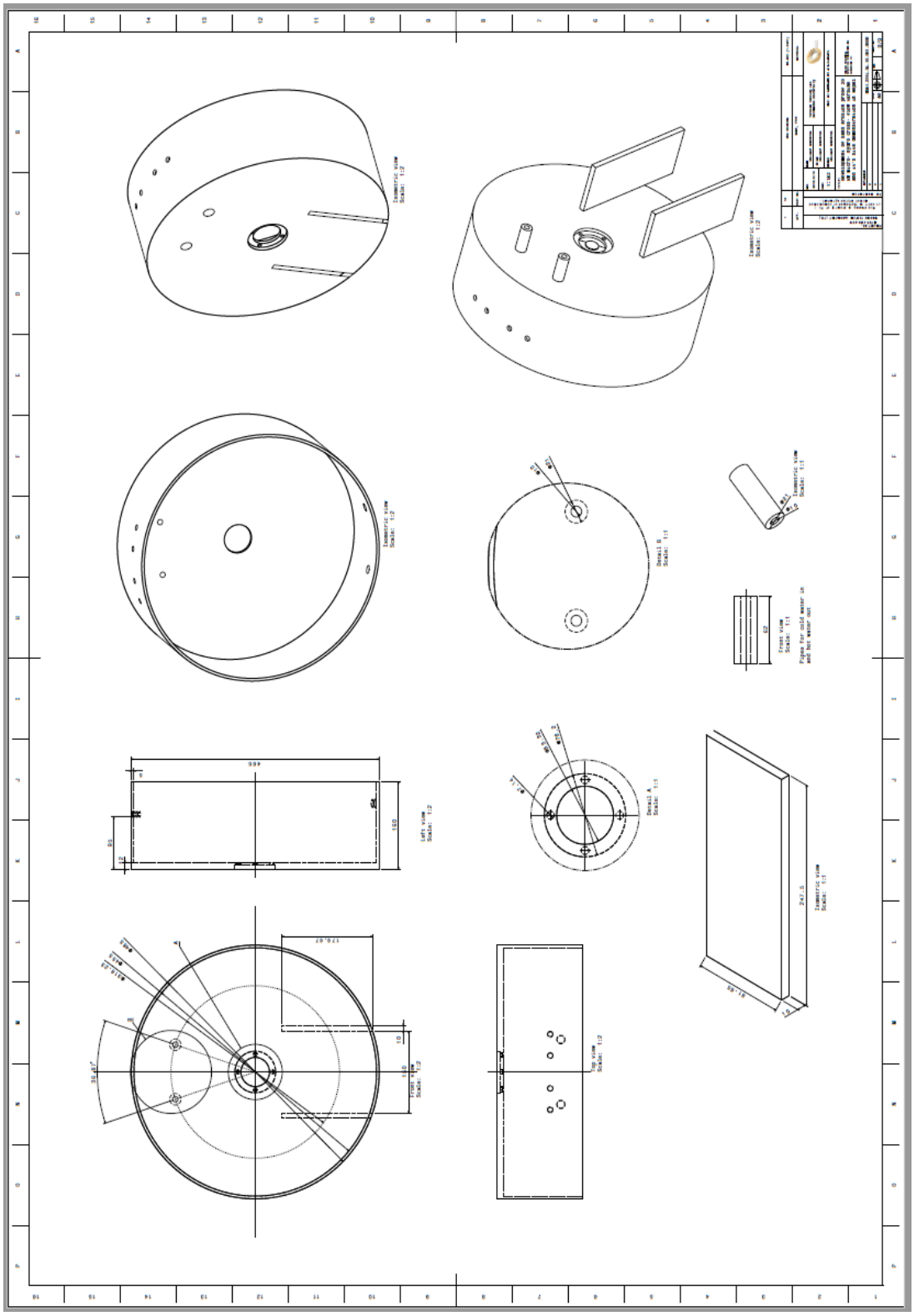

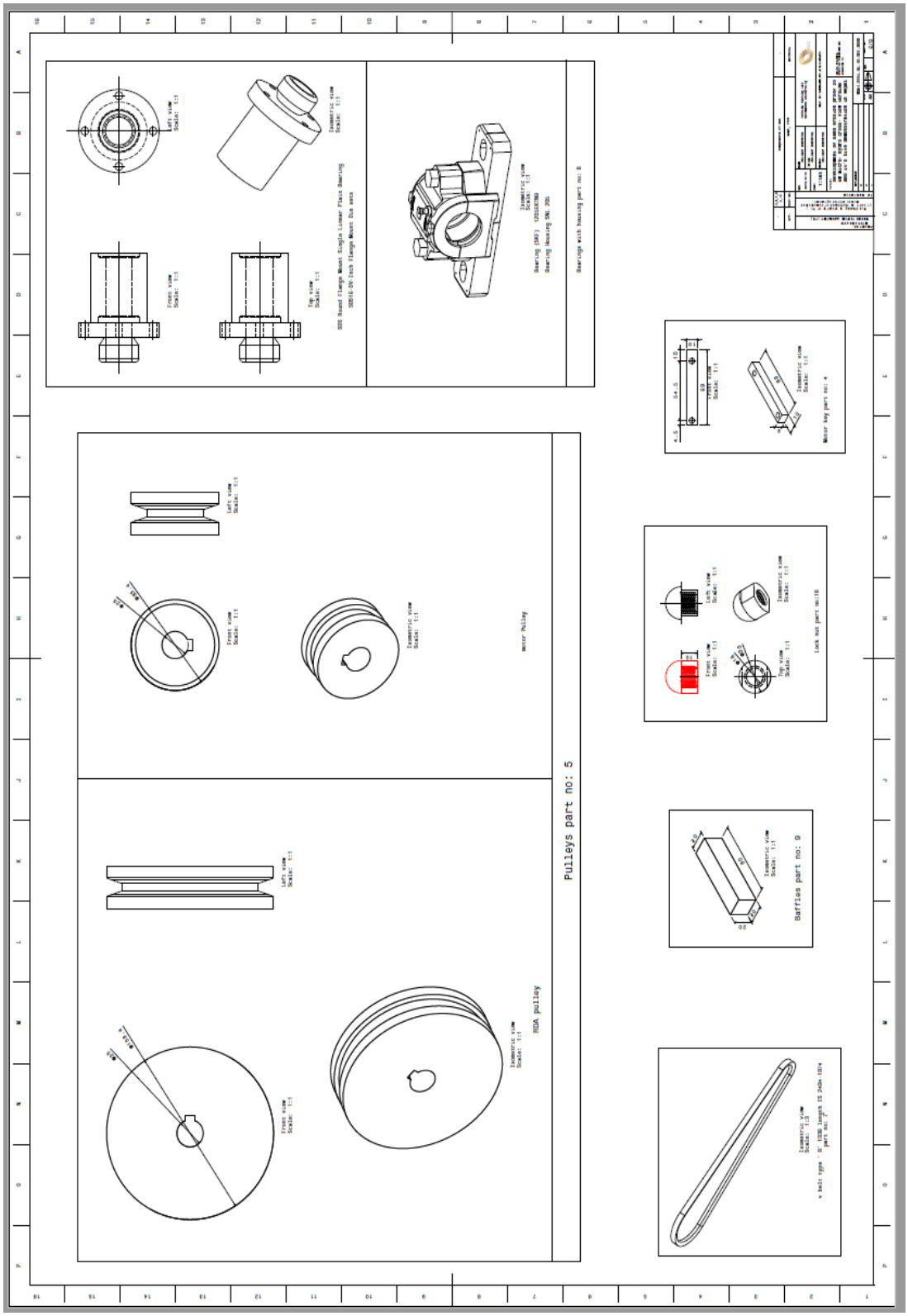
Pulleys part no: 5
Baffles part no: 9

Appendix C: Manufacturing drawings of CFT test rig

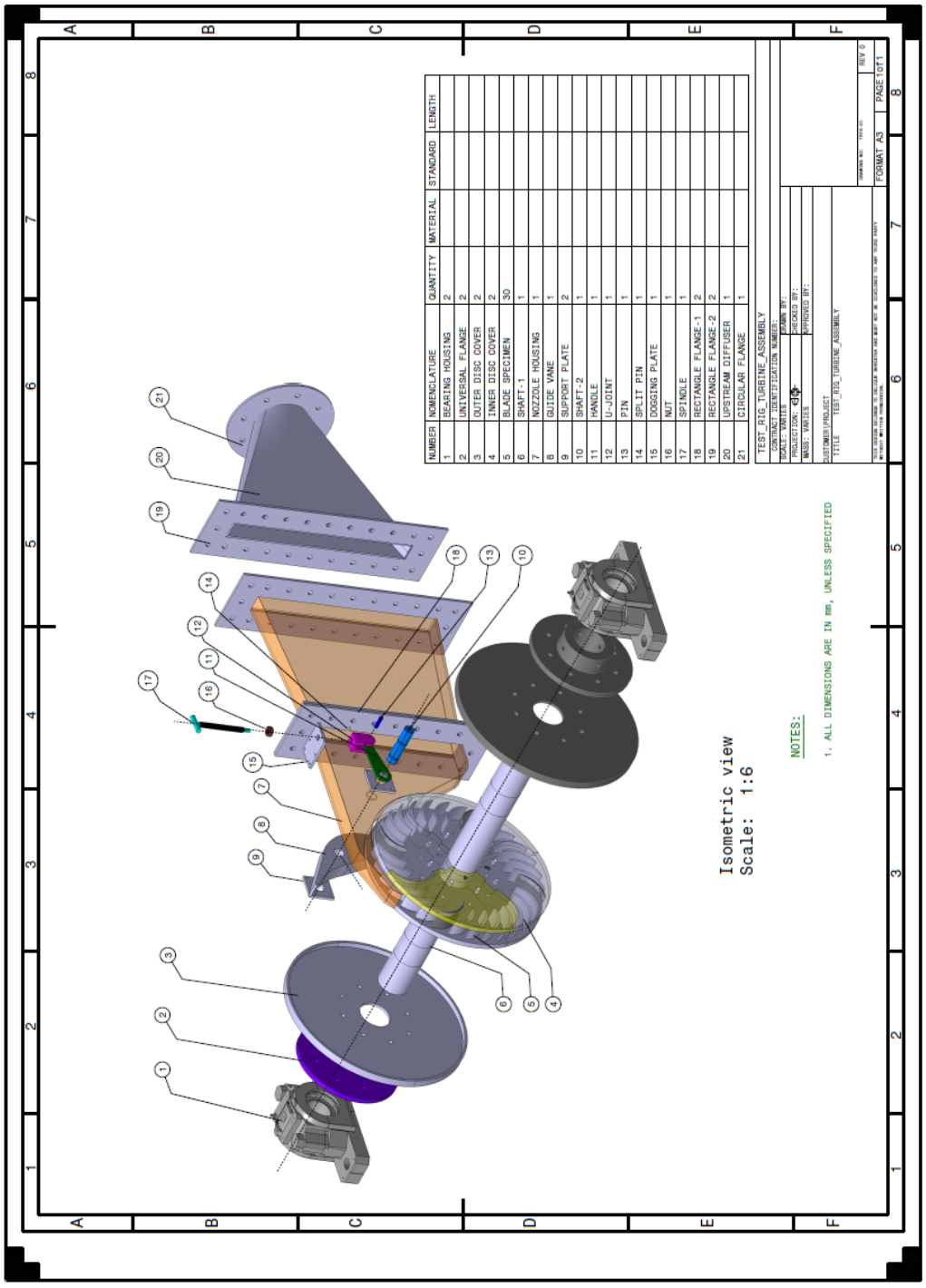

NUMBER	NOMENCLATURE	QUANTITY	MATERIAL	STANDARD	LENGTH
1	BEARING HOUSING	2			
2	UNIVERSAL FLANGE	2			
3	OUTER DISC COVER	2			
4	INNER DISC COVER	2			
5	BLADE SPECIMEN	30			
6	SHAFT-1	1			
7	NOZZOLE HOUSING	1			
8	GUIDE VANE	1			
9	SUPPORT PLATE	2			
10	SHAFT-2	1			
11	HANDLE	1			
12	U-JOINT	1			
13	PIN	1			
14	SPLIT PIN	1			
15	DOGGING PLATE	1			
16	NUT	1			
17	SPINDLE	1			
18	RECTANGLE FLANGE-1	2			
19	RECTANGLE FLANGE-2	2			
20	UPSTREAM DIFFUSER	1			
21	CIRCULAR FLANGE	1			

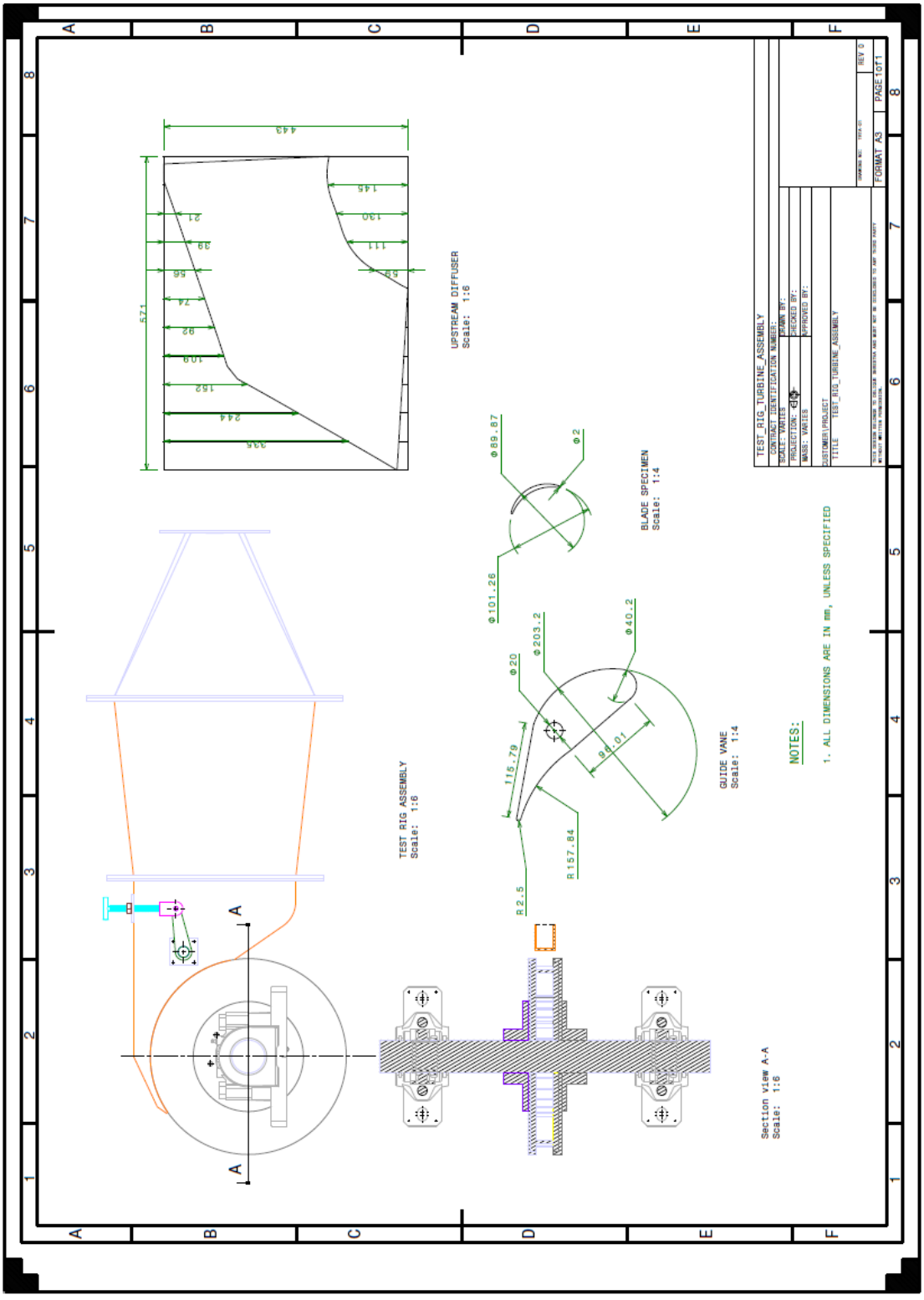
443
571
145
130
111
89
21
29
56
74
92
109
152
244
335
UPSTREAM DIFFUSER
Scale: 1:6
Ø89.87
Ø2
Ø101.26
BLADE SPECIMEN
Scale: 1:4
Ø203.2
Ø40.2
Ø20
116.79
94.01
R157.84
R2.5
GUIDE VANE
Scale: 1:4
TEST RIG ASSEMBLY
Scale: 1:6
A
A
NOTES:
1. ALL DIMENSIONS ARE IN MM, UNLESS SPECIFIED
Section view A-A
Scale: 1:6
TEST_RIG_TURBINE_ASSEMBLY
CONTRACT IDENTIFICATION NUMBER:
SCALE: VARIES
PROJECTION:
MASS: VARIES
DRAWN BY:
CHECKED BY:
APPROVED BY:
CUSTOMER\PROJECT
TITLE
TEST_RIG_TURBINE_ASSEMBLY
FORMAT A3
PAGE 1 of 1
REV 0

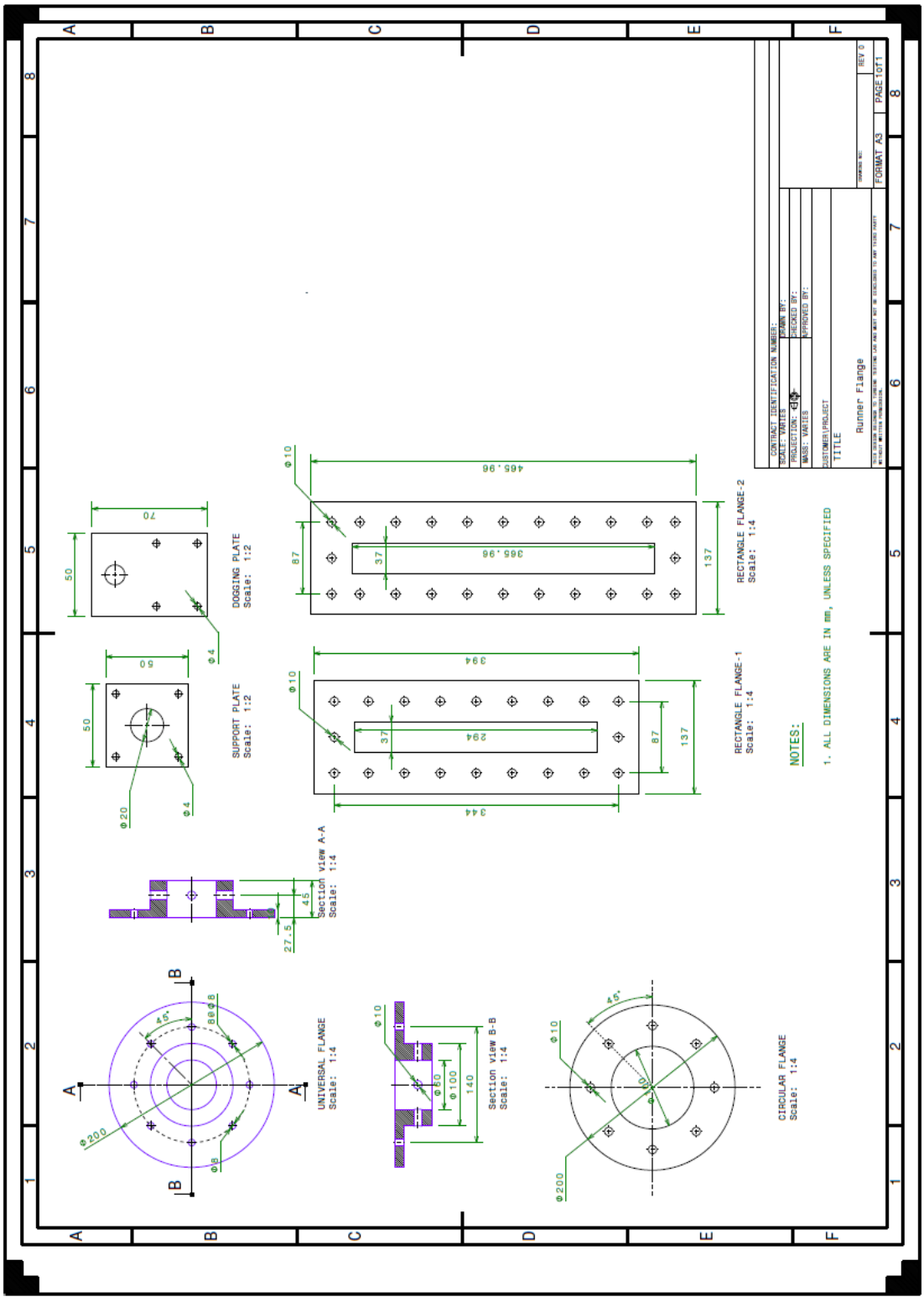
Runner Flange
FORMAT A3
PAGE 1 of 1
REV 0
CONTRACT IDENTIFICATION NUMBER:
DRAWN BY:
CHECKED BY:
APPROVED BY:
PROJECTION:
MASS: VARIES
CUSTOMER\PROJECT
TITLE
NOTES:
1. ALL DIMENSIONS ARE IN mm, UNLESS SPECIFIED
DOGGING PLATE
Scale: 1:2
SUPPORT PLATE
Scale: 1:2
RECTANGLE FLANGE-2
Scale: 1:4
RECTANGLE FLANGE-1
Scale: 1:4
Section view A-A
Scale: 1:4
UNIVERSAL FLANGE
Scale: 1:4
Section view B-B
Scale: 1:4
CIRCULAR FLANGE
Scale: 1:4

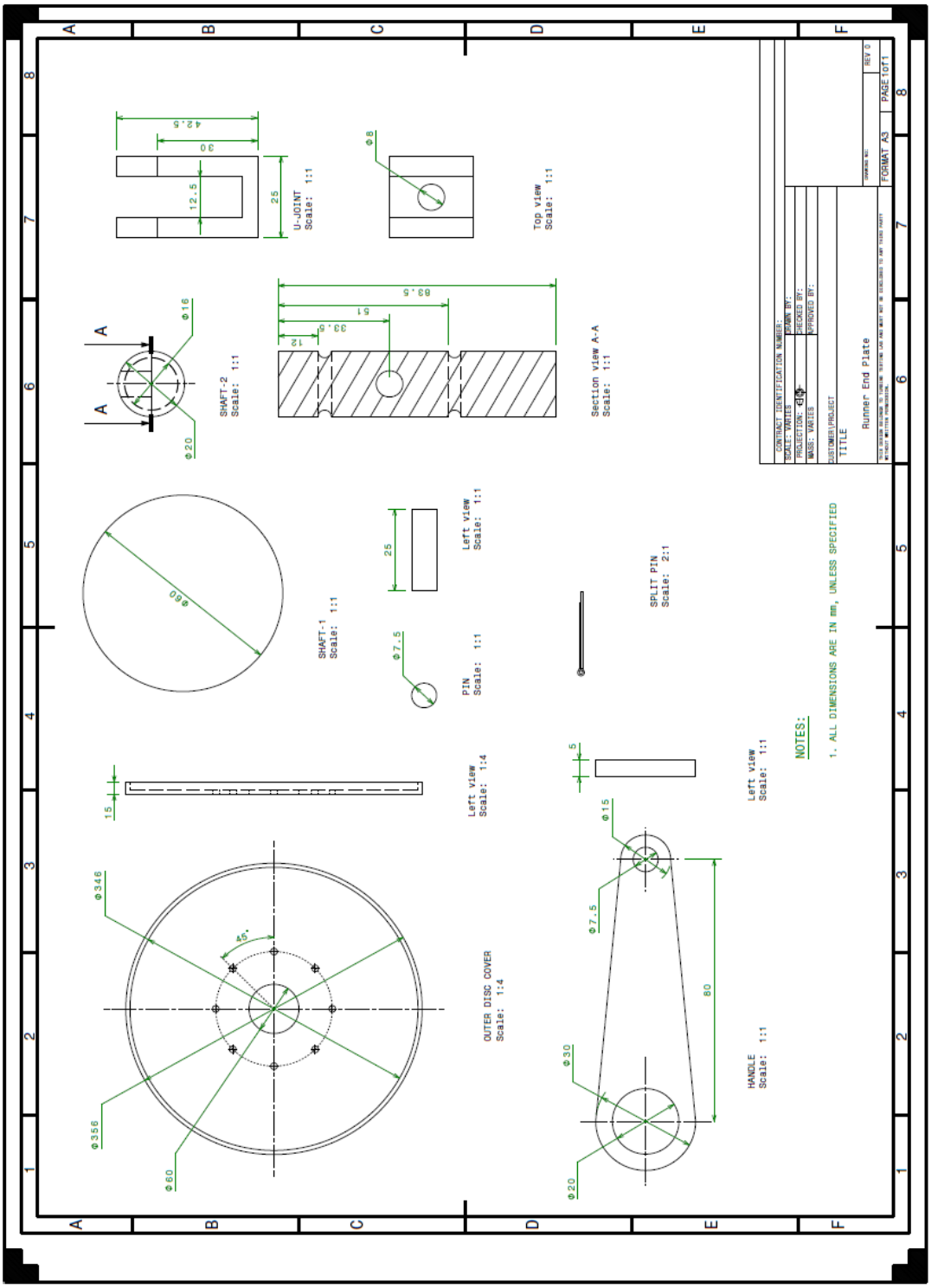
U-JOINT
Scale: 1:1
Top view
Scale: 1:1
SHAFT-2
Scale: 1:1
Section view A-A
Scale: 1:1
SHAFT-1
Scale: 1:1
Left view
Scale: 1:1
PIN
Scale: 1:1
SPLIT PIN
Scale: 2:1
Left view
Scale: 1:4
OUTER DISC COVER
Scale: 1:4
Left view
Scale: 1:1
HANDLE
Scale: 1:1
NOTES:
1. ALL DIMENSIONS ARE IN mm, UNLESS SPECIFIED
CONTRACT IDENTIFICATION NUMBER:
SCALE: VARIES
PROJECTION:
MASS: VARIES
DRAWN BY:
CHECKED BY:
APPROVED BY:
CUSTOMER/PROJECT
TITLE
Runner End Plate
FORMAT A3
PAGE1of1
REV 0

Appendix D: Computing regression/systematic error

The error is a variation between the measured value and the actual value. From the statistical methods, a 95 % standard probability of the confidence interval is considered.

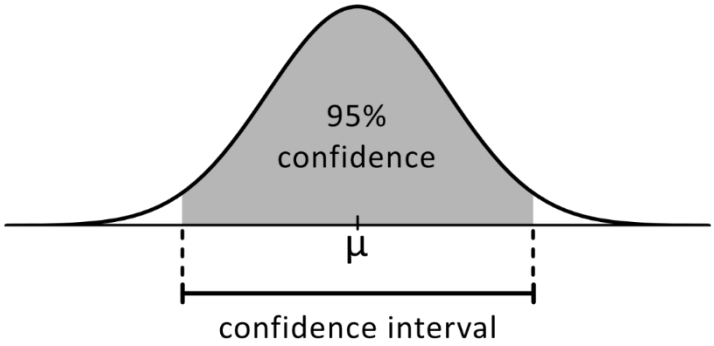

Figure B. 1: A normal distribution with a 95 % confidence level.

Whenever a linear approximation is generated as a calibration curve it is obvious that an error due to the assumption that all the measurements must be in the curved fashion occurs. S_{xx} (Eq. B.1) and S_{yy} (Eq. B.2) are the variations of x and y individually around the regression line.

$$S_{XX} = \sum_{i=1}^{N}(x_i - \bar{x})^2 \quad \text{(D.1)}$$

$$S_{YY} = \sum_{i=1}^{N}(y_i - \bar{Y})^2 \quad \text{(D.2)}$$

$$S_{XY} = \sum_{i=1}^{N}(x_i - \bar{x})\,(y_i - \bar{Y}) \quad \text{(D.3)}$$

S_{xy} is the combined variation of x and y around the regression line. Equation (B.4) indicates the expression for the sum of squared errors about the regression line and is expressed as SSE. Eq. B.5 shows an unbiased estimate of the variance of the regression line fashioned with the SSE. [113]

$$SSE = S_{yy} - bS_{xy} \quad \text{(D.4)}$$

$$S^2 = \frac{SSE}{N-2} \quad \text{(D.5)}$$

The regression curve can be expressed as an estimate of the mean response, Y_0, of an input x_0. Eq. B.6 indicates the expression for the confidence interval of the mean response of a given input around the regression line.

$$\hat{Y}_o - t_{\alpha/2} \times S\sqrt{\frac{1}{n} + \frac{(x_o - \bar{x})^2}{S_{xx}}} \leq \mu_{Y|x_o} \leq \hat{Y}_o + t_{\alpha/2} \times S\sqrt{\frac{1}{n} + \frac{(x_o - \bar{x})^2}{S_{xx}}} \quad \text{(D.6)}$$

$$f_{Y|x_o} = \pm t_{\alpha/2} \times S\sqrt{\frac{1}{n} + \frac{(x_o - \bar{x})^2}{S_{xx}}} \quad \text{(D.7)}$$

It is essential to calculate uncertainty for each y-value with the corresponding x-value in order to find the confidence interval along with the linear approximation.

Appendix E: Uncertainty analysis

The uncertainty analysis is considered based on the method described in Storli [114] and the calculations performed by Danielsen and Walseth for experimentation on Crossflow turbine [115]

The relative uncertainty, f_x, of measurement, is articulated as:

$$f_x = \frac{e_x}{x} \tag{E.1}$$

e_x = Absolute uncertainty in measurement of X

X = the measured quantity

Using the root-sum square method to determine the systematic uncertainty in the efficiency measurements the expression for the uncertainty in the efficiency is

$$f_{\eta\,(sys)} = \sqrt{f_\rho^2 + f_g^2 + f_{He}^2 + f_Q^2 + f_T^2 + f_\omega^2} \tag{E.2}$$

f_ρ = Uncertainty in the density of the water = 0, Negligible compared to the other uncertainties

f_g = Uncertainty deciding the gravitational constant= 0, Negligible compared to the other uncertainties

f_{He} = Uncertainty in calculated net head

f_Q = Uncertainty in measured volume flow rate

f_T = Uncertainty in measured torque

$f\omega$ = Uncertainty in measured rotational speed

The expression of the uncertainty of the measured net head

$$f_{He\,(SYS)} = \pm \frac{\sqrt{\left(\frac{e\Delta p}{\rho g}\right)^2 + {e_z}^2 + \left(\frac{e_{v_1}^2}{2g}\right)^2}}{H_e} \tag{E.3}$$

$e\Delta p$ = The absolute systematic error for the pressure

e_z = The absolute systematic error for the measured difference in height

e_{v1} = The absolute systematic error for the velocity at the turbine

$$\frac{e\Delta p}{\rho g} = \frac{\Delta p}{\rho g} f_{\Delta p} \tag{E.4}$$

$$\frac{e_{v1}}{g} = \frac{v_1^2}{g} f_{v1} \quad \text{(E.5)}$$

$$f_{v1} = \sqrt{f_Q^2 + 2\left(\frac{e_r}{2r}\right)^2} \quad \text{(E.6)}$$

$$e_r = \sqrt{e_Q^2 + e_L^2 + e_B^2} \quad \text{(E.7)}$$

Uncertainty is a combination of systematic and random error and can be expressed as:

$$f_n = \sqrt{f_{rand}^2 + f_{sys}^2} \quad \text{(E.8)}$$

f_{sys} = Systematic uncertainty in measuring devices

f_{rand} = Random uncertainty in measurements, where

$$f_{rand} = \frac{s_y t_{\alpha/2}}{\bar{Y}_\eta \sqrt{n}} \quad \text{(E.9)}$$

S_y = Standard deviation

$\bar{Y}_\eta$ = Aritmetic mean value

n =Number of measurements

t = Student t distribution

$$s_y = \sqrt{\frac{\sum_{i=1}^{n}(Y_i - \bar{Y})^2}{n-1}} \quad \text{(E.10)}$$

Y_i – Individual measurement

Appendix F: LabVIEW GUI

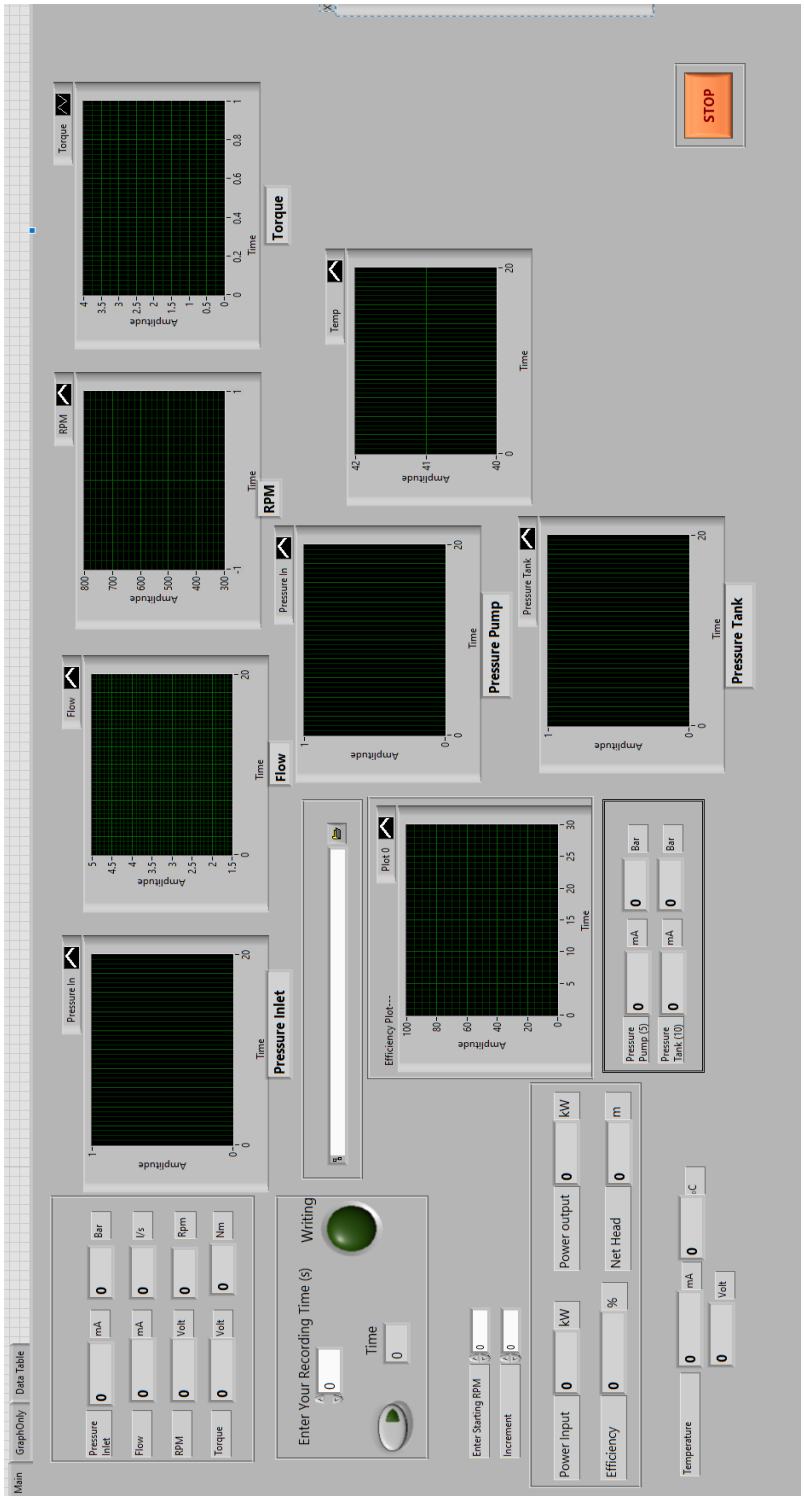

Appendix G: MATLAB script to plot efficiency hill diagram and sediment erosion hill diagram.

```
clear all
close all
    effi(:)=xlsread('10m_31mm_RPM_DOGV_BETA-16d.xlsx','Sheet1','I2:I91');
    Ned_a(:)=xlsread('10m_31mm_RPM_DOGV_BETA-16d.xlsx','Sheet2','D3:D92');
    Qed_a(:)=xlsread('10m_31mm_RPM_DOGV_BETA-16d.xlsx','Sheet2','E3:E92');
   SERD(:,:)=xlsread('10m_31mm_RPM_DOGV_BETA16d.xlsx','Sheet1','Y2:AF91');

 SERD_all=zeros(10,9,8);
Efficiency_all = zeros(10,9);
Ned_all = zeros (10,9);
Qed_all = zeros (10,9);
D = 0.3;
Maxe=0;
for i = 1:10
    for j=1:9
        Efficiency_all(i,j) = effi((i-1)*9+j);
       if Maxe<Efficiency_all(i,j)
          Maxe=Efficiency_all(i,j);
       end
        Ned_all(i,j) = Ned_a((i-1)*9+j);
        Qed_all(i,j) = Qed_a((i-1)*9+j);
    end
end
 for i=1:10
     for j=1:9
         for k=1:8
            SERD_all(i,j,k)=SERD((i-1)*9+j,k);
         end
     end
 end

contourf(Ned_all,Qed_all,Efficiency_all/Maxe,10,'ShowText','on');
colormap(white);
set (gcf, 'unit', 'centimeters', 'Position', [0 1 9 10]);
set (gca, 'FontSize', 24, 'FontName', 'Times New Roman');

hold on;
plot(Ned_all(1,:),Qed_all(1,:),'k--');
plot(Ned_all(2,:),Qed_all(2,:),'k-.');
plot(Ned_all(3,:),Qed_all(3,:),'k-o');
plot(Ned_all(4,:),Qed_all(4,:),'k-x');
plot(Ned_all(5,:),Qed_all(5,:),'r--');
```

```
plot(Ned_all(6,:),Qed_all(6,:),'r-.','linewidth',2);
plot(Ned_all(7,:),Qed_all(7,:),'r-o');
plot(Ned_all(8,:),Qed_all(8,:),'r-x');
plot(Ned_all(9,:),Qed_all(9,:),'r');
plot(Ned_all(10,:),Qed_all(10,:),'k');
xlabel('Ned[-]');
ylabel('Qed[-]');
title ('Efficiency Chart of turbine corresponding to Cross Flow Turbine','FontSize',16);
set (gcf, 'unit', 'centimeters', 'Position', [0 1 9 10]);
set (gca, 'FontSize', 24, 'FontName', 'Times New Roman');

hold off;
 mic=75;
 for i=1:8

    figure(i+1);
    contourf(Ned_all,Qed_all,SERD_all(:,:,i),10,'ShowText','on');
    set (gcf, 'unit', 'centimeters', 'Position', [0 1 9 10]);
    set (gca, 'FontSize', 24, 'FontName', 'Times New Roman');
    hold on;
    plot(Ned_all(1,:),Qed_all(1,:),'k--');
    plot(Ned_all(2,:),Qed_all(2,:),'k-.');
    plot(Ned_all(3,:),Qed_all(3,:),'k-o');
    plot(Ned_all(4,:),Qed_all(4,:),'k-x');
    plot(Ned_all(5,:),Qed_all(5,:),'r--');
    plot(Ned_all(6,:),Qed_all(6,:),'r-.','linewidth',2);
    plot(Ned_all(7,:),Qed_all(7,:),'r-o');
    plot(Ned_all(8,:),Qed_all(8,:),'r-x');
    plot(Ned_all(9,:),Qed_all(9,:),'r');
    plot(Ned_all(10,:),Qed_all(10,:),'k');
    xlabel('Ned[-]');
    ylabel('Qed[-]');
    title ([sprintf('Sediment Erosion rate Density under different operating conditions
with %d micron sediment',mic)],'FontSize',16);
    set (gcf, 'unit', 'centimeters', 'Position', [0 1 9 10]);
    set (gca, 'FontSize', 24, 'FontName', 'Times New Roman');
    hold off;
    mic=mic+25;
 end
```

Appendix H: SERDs with five Beta Angles with various sided sediments

Beta Angle 16°

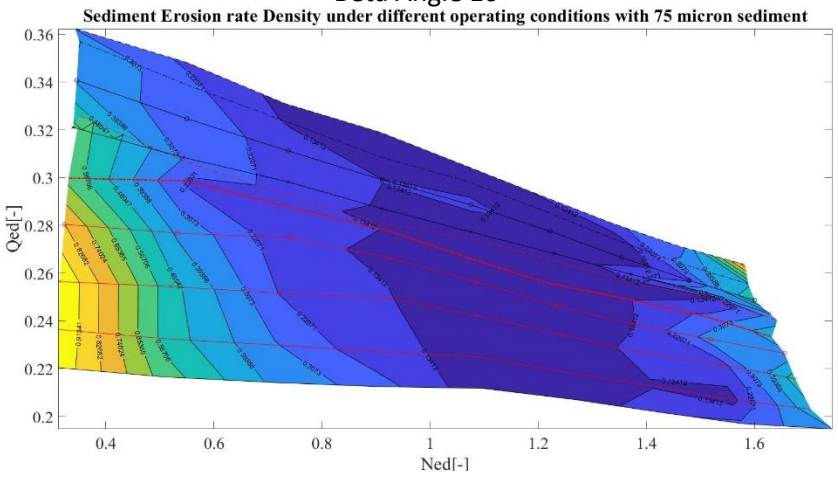

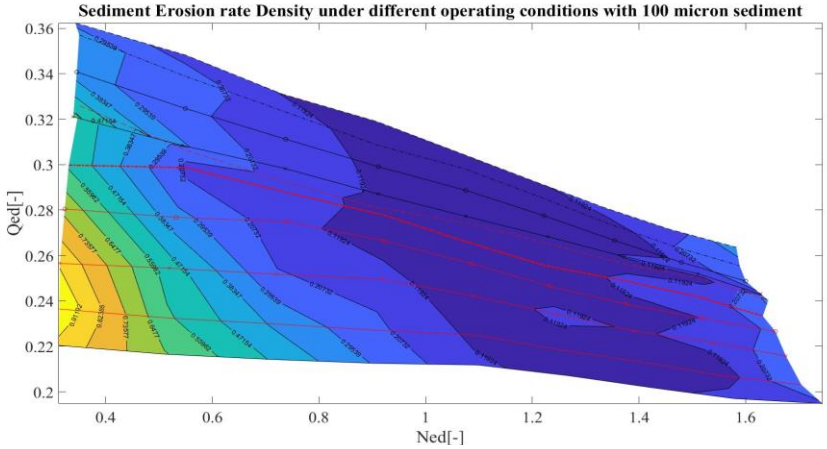

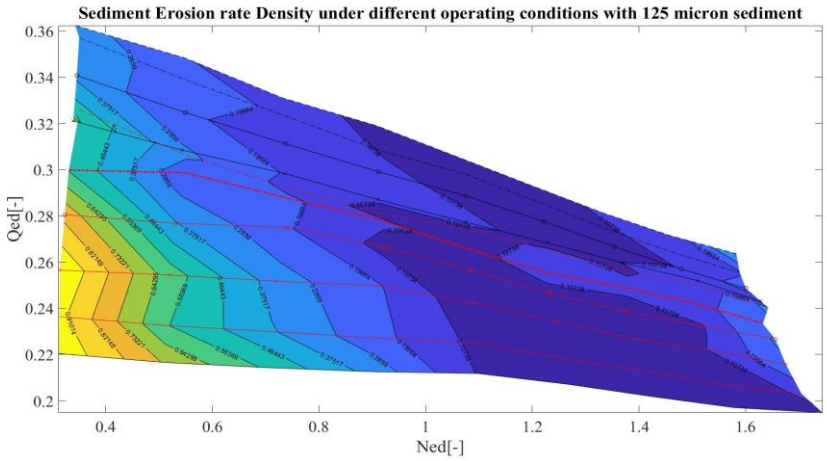

Beta Angle 16°

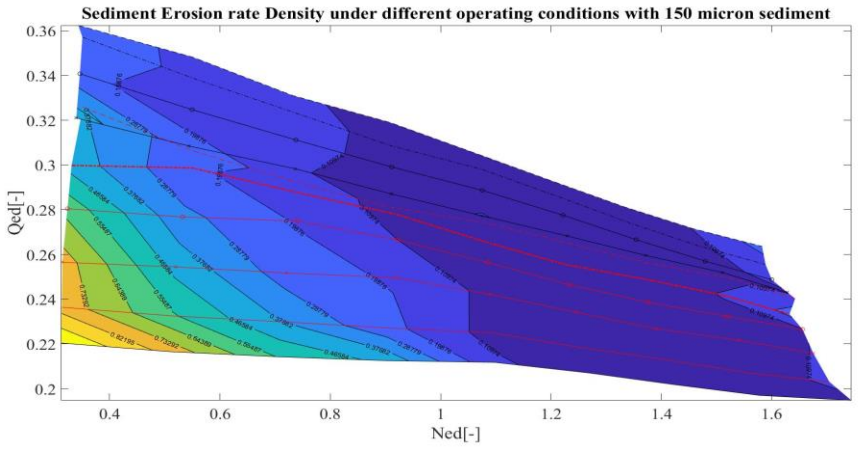

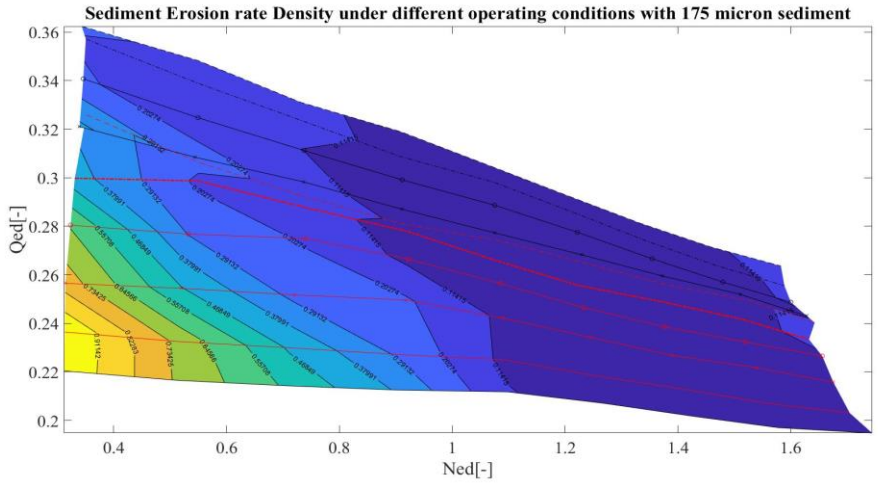

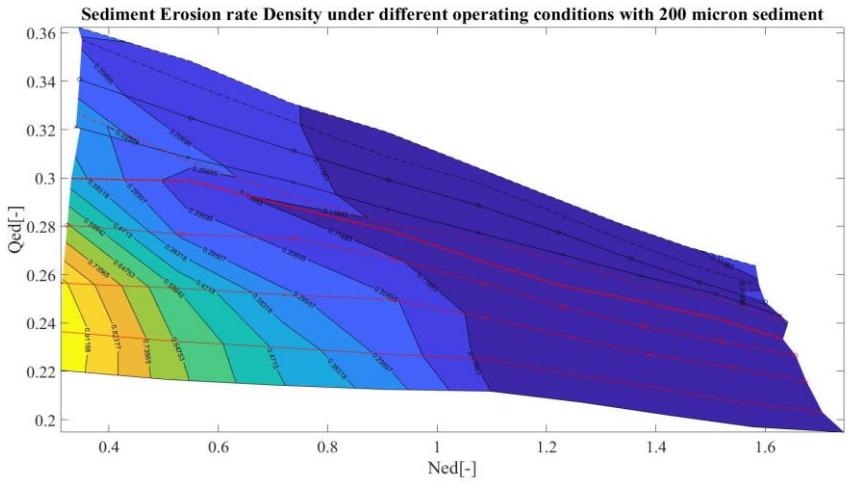

Beta Angle 16°

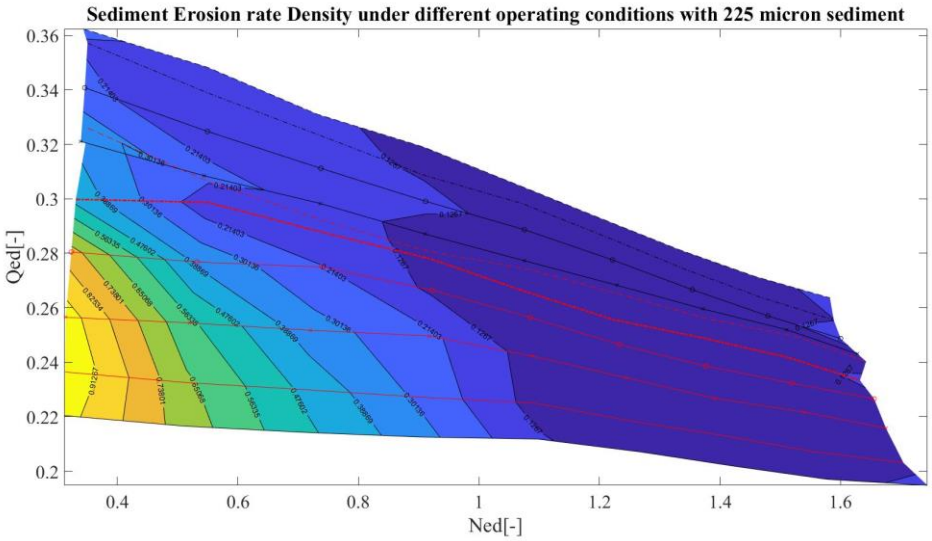

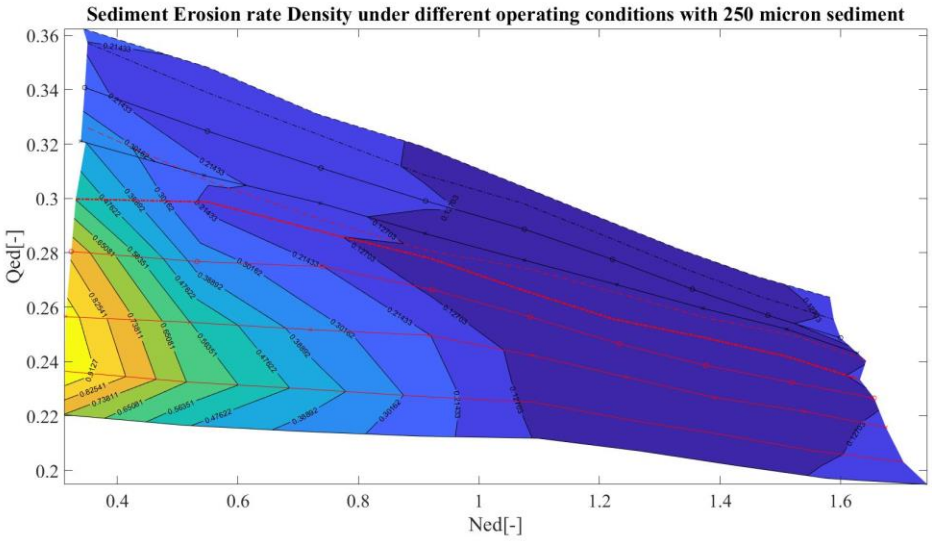

Beta Angle 18°

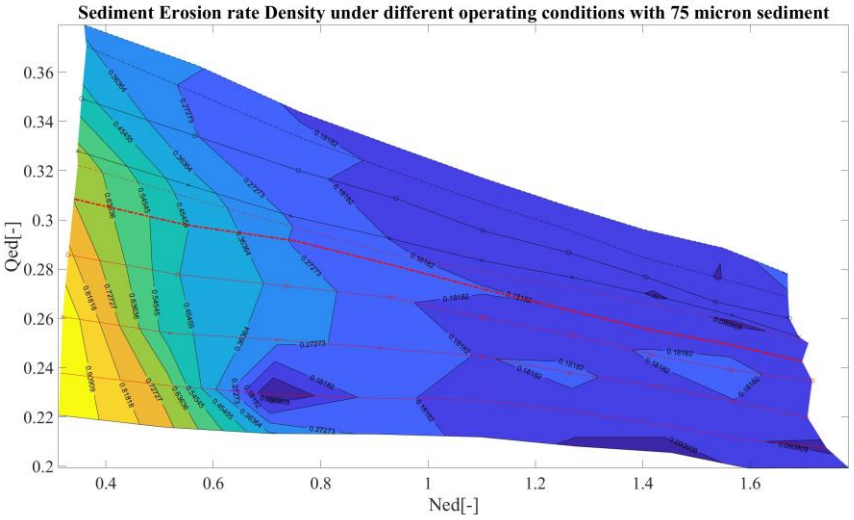

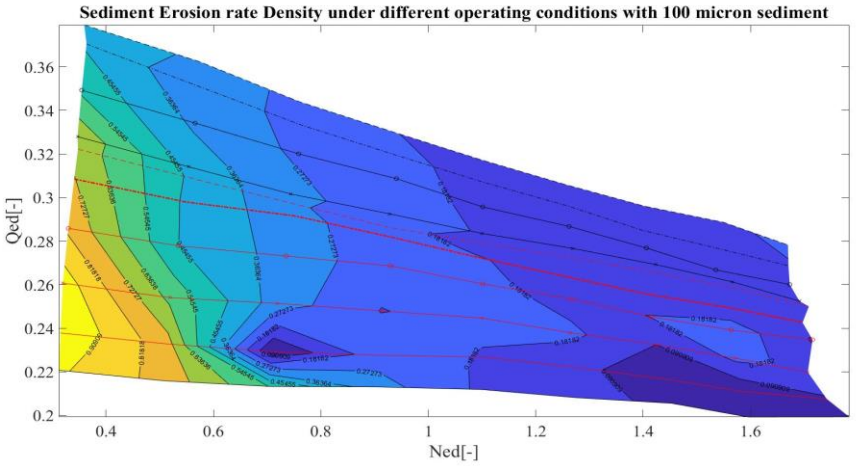

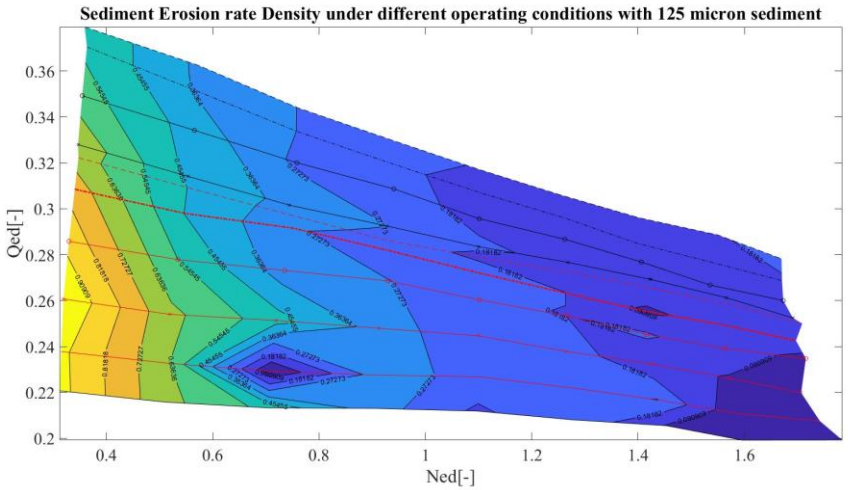

Beta Angle 18°

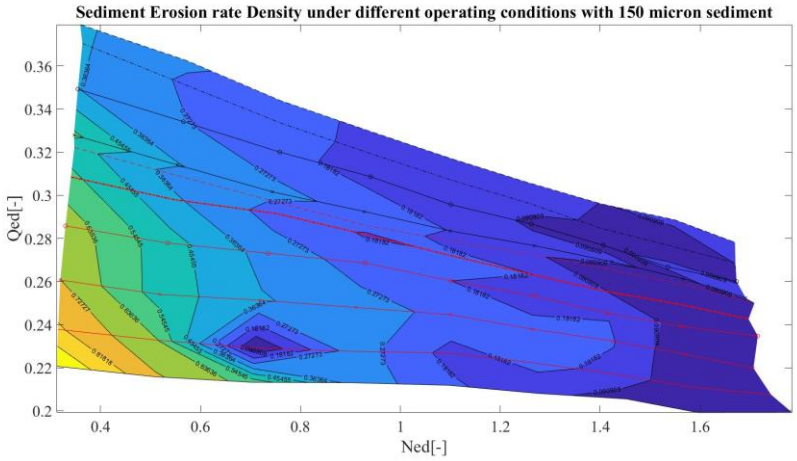

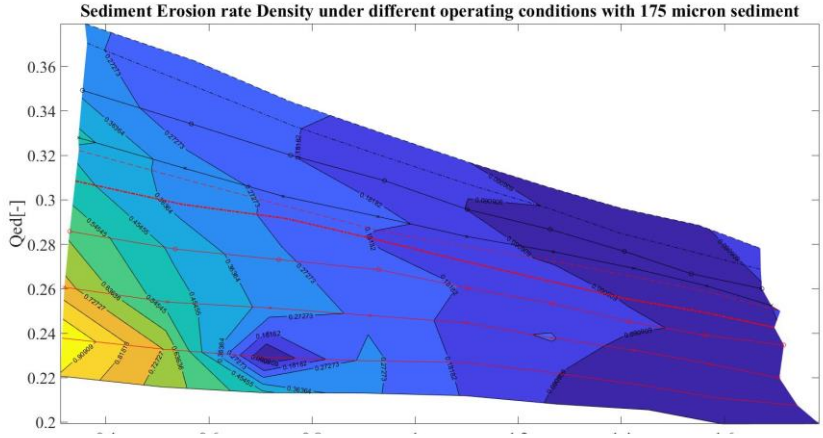

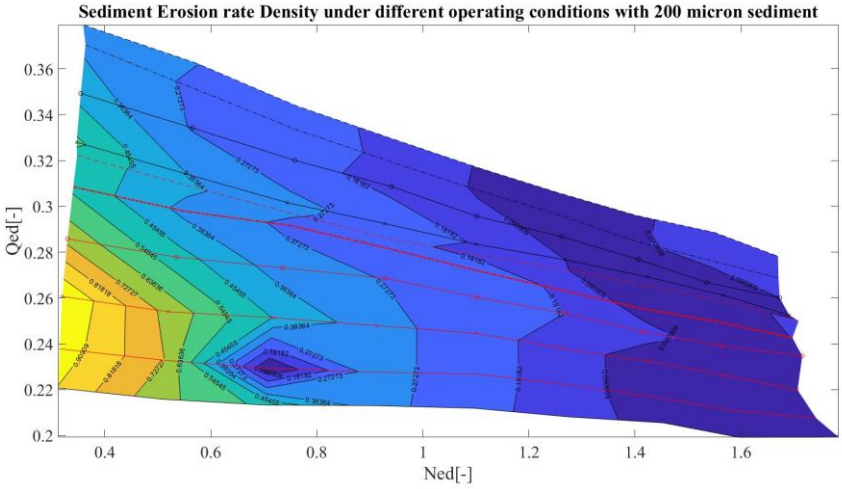

Beta Angle 18°

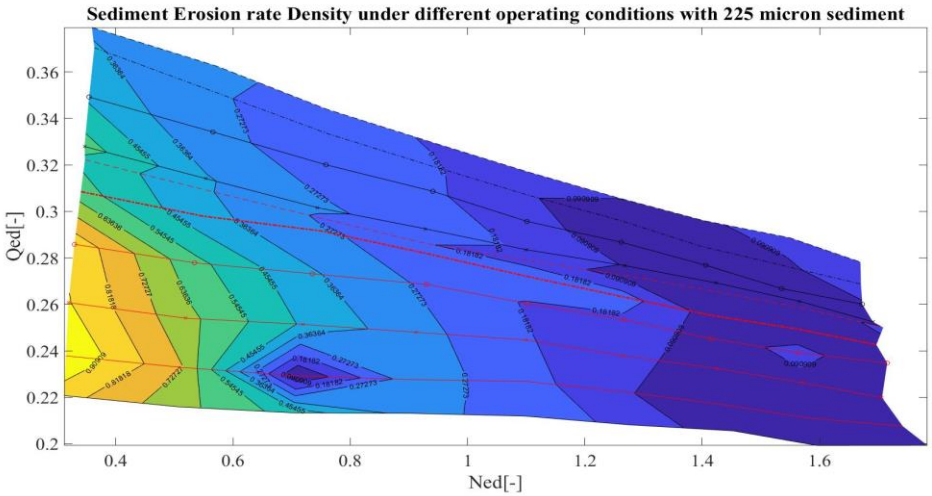

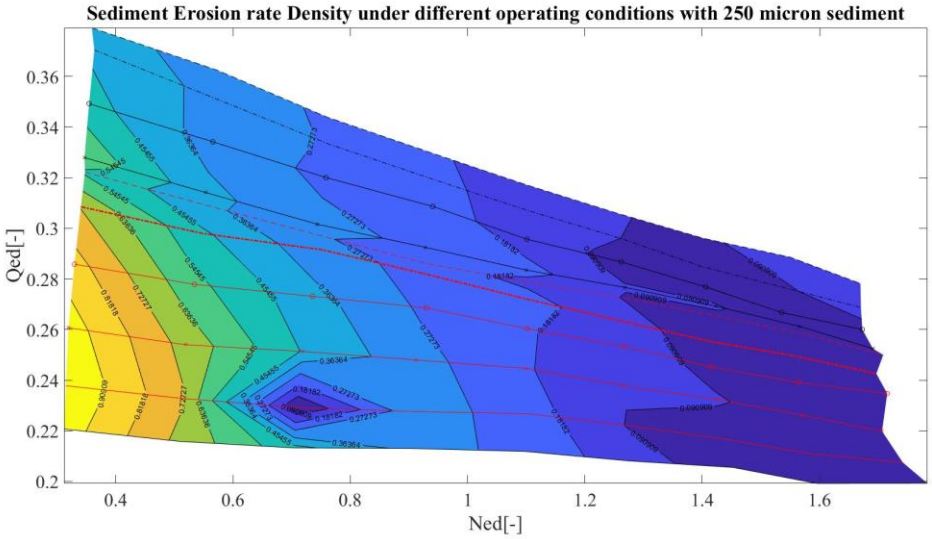

Beta Angle 24°

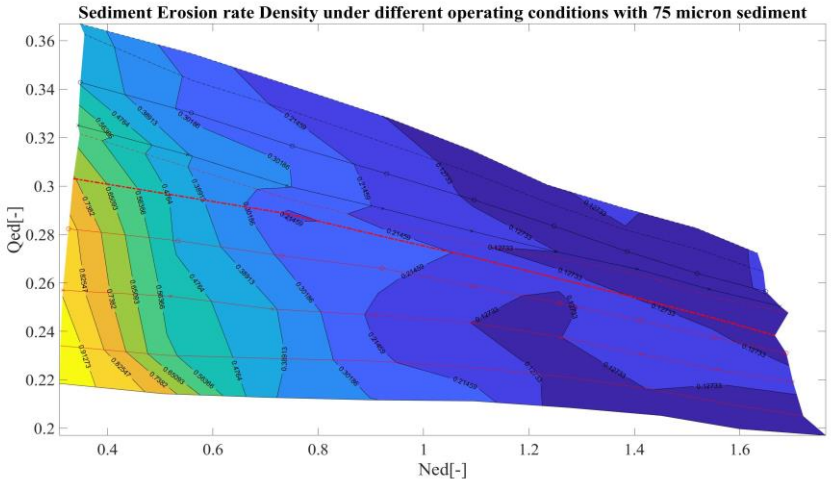

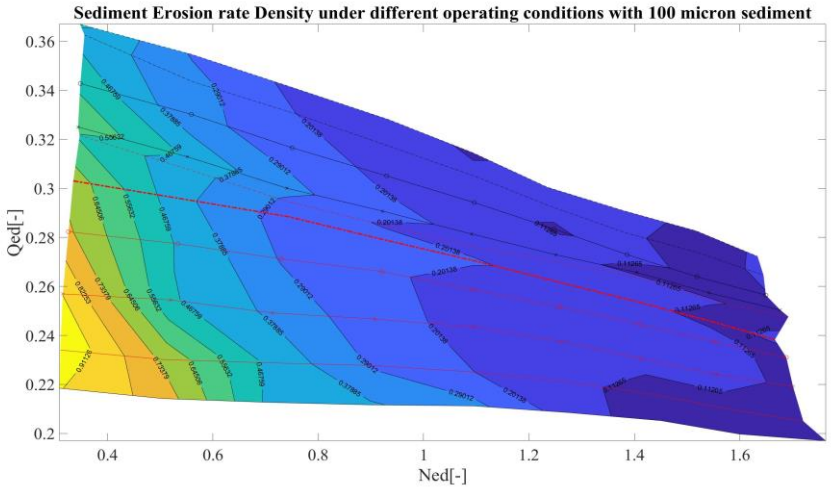

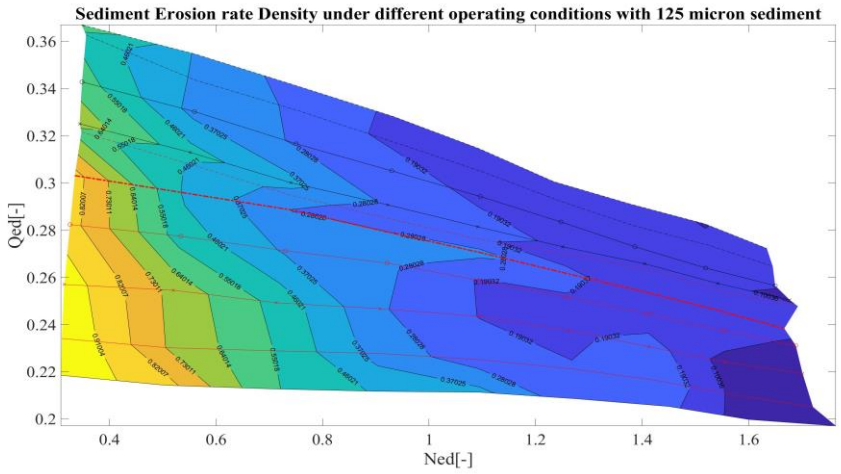

Beta Angle 24°

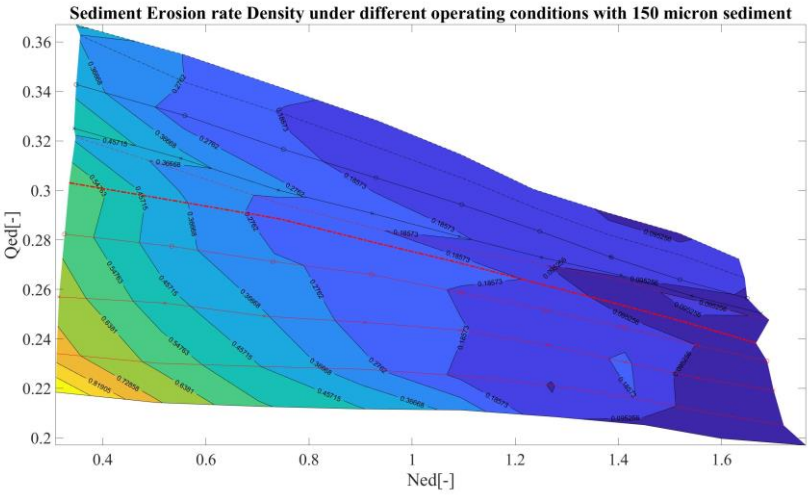

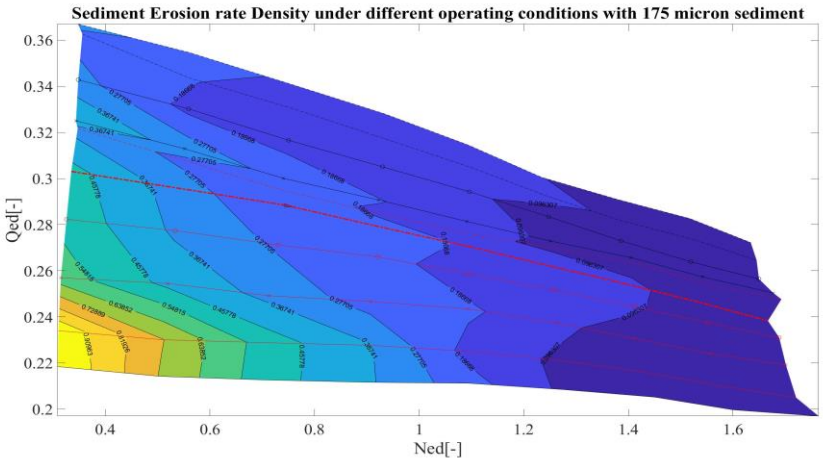

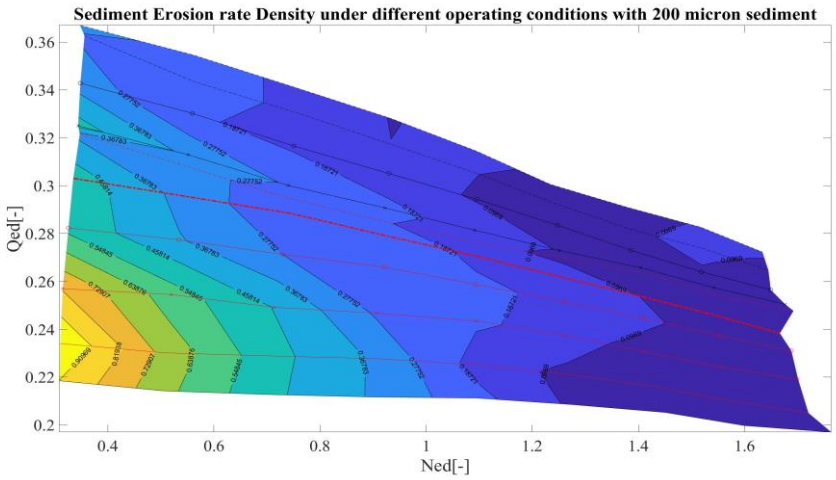

Beta Angle 24°

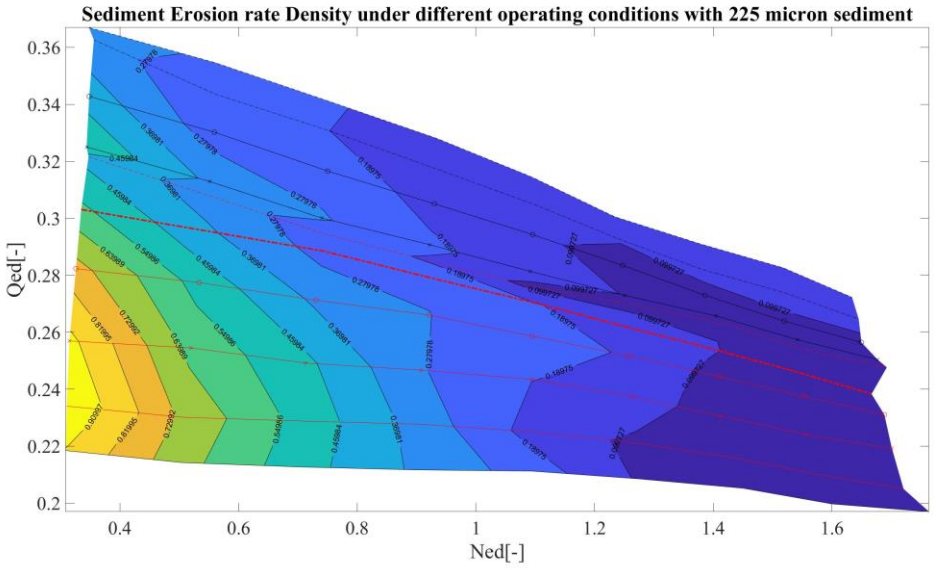

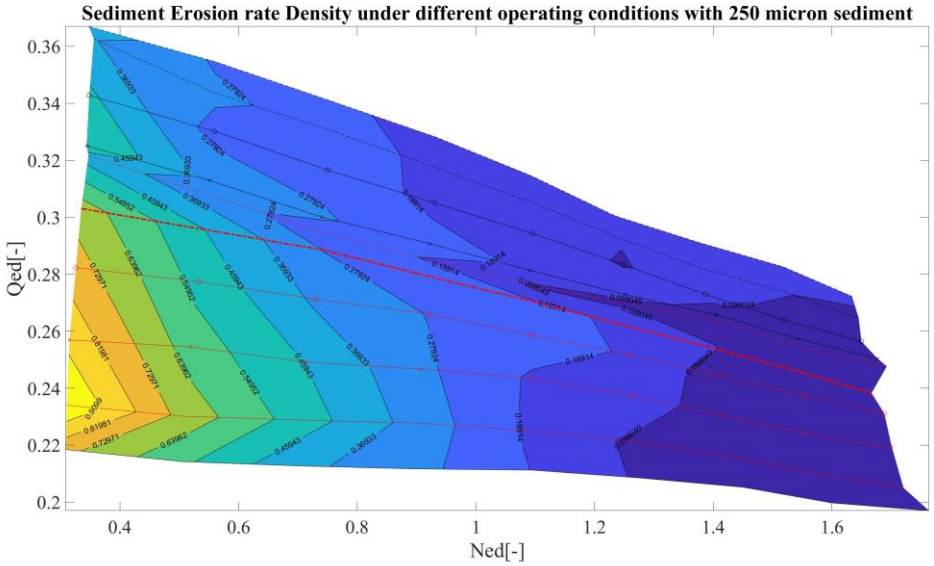

Beta Angle 30°

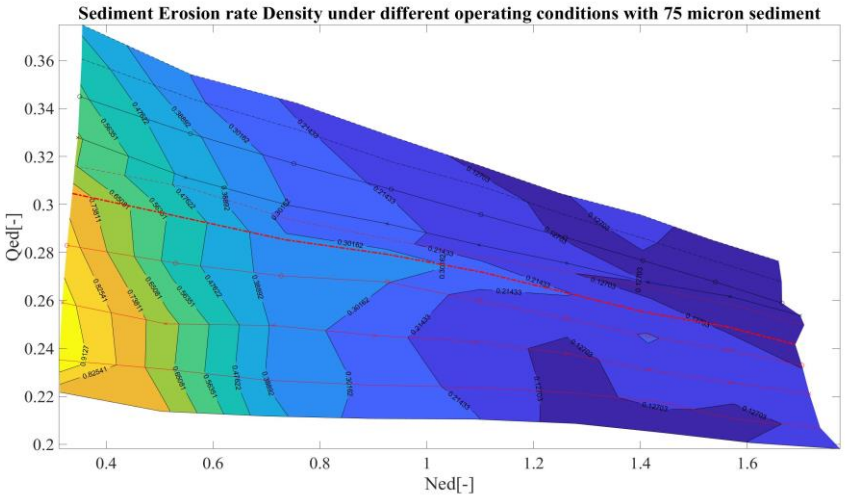

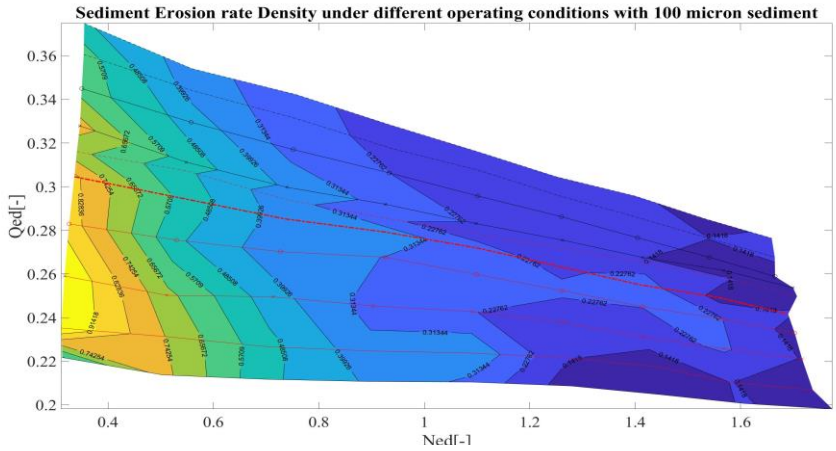

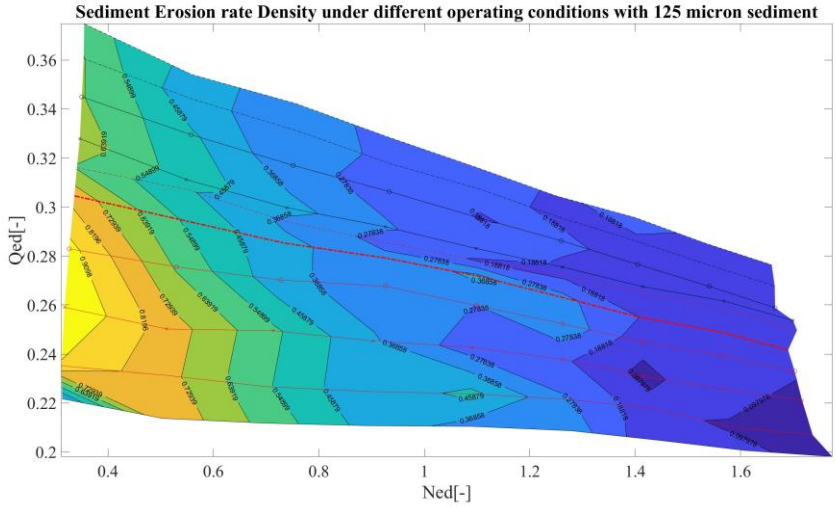

Beta Angle 30°

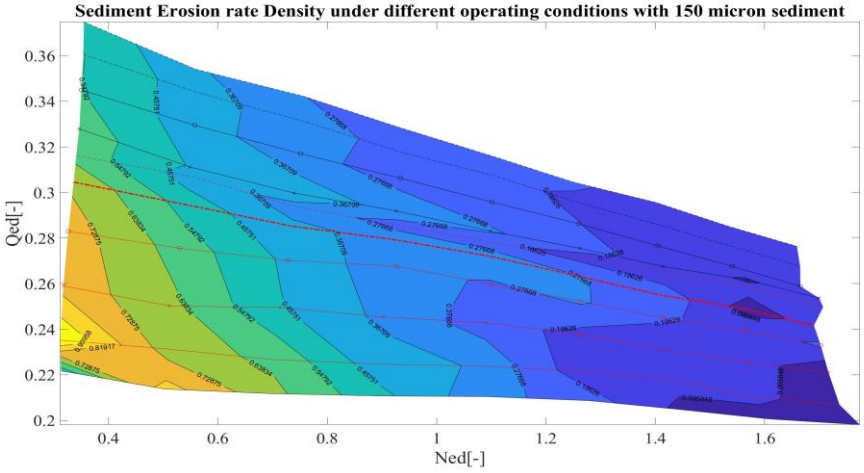

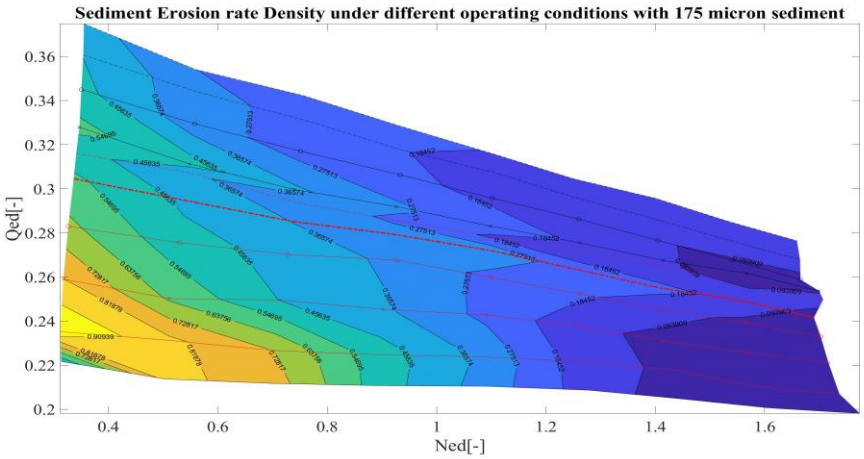

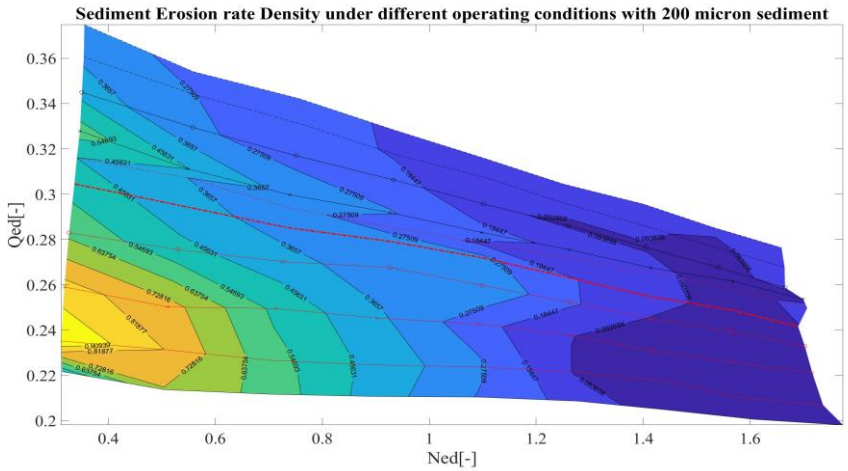

Beta Angle 30°

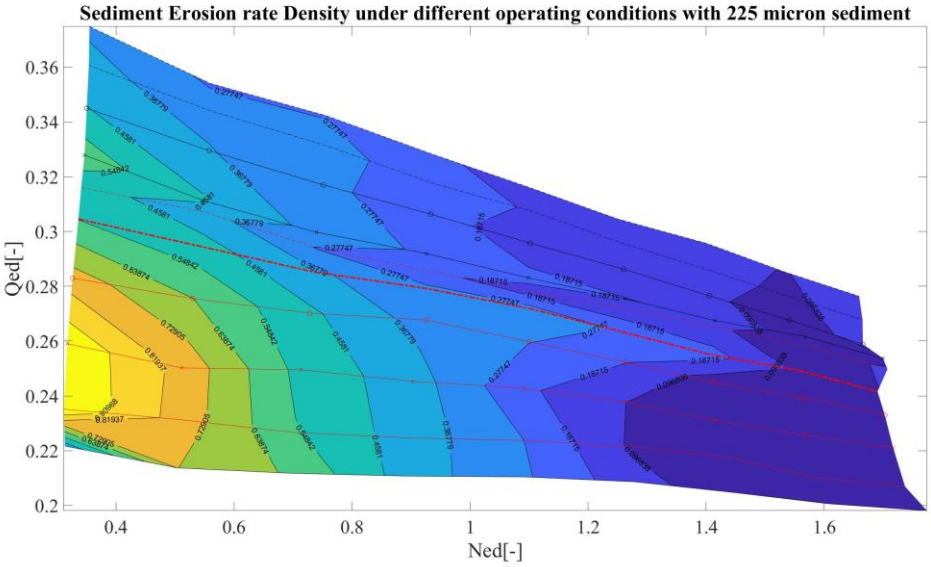

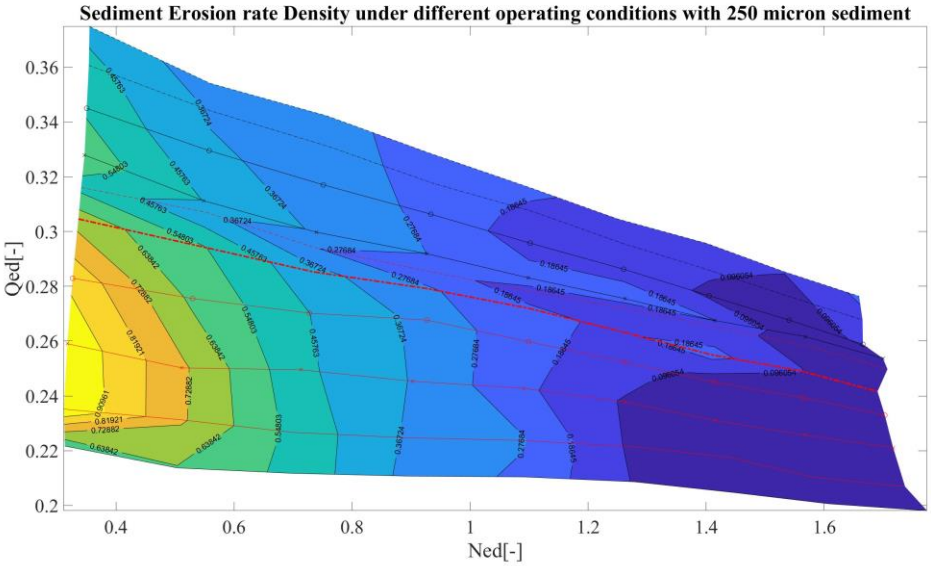

Beta Angle 36°

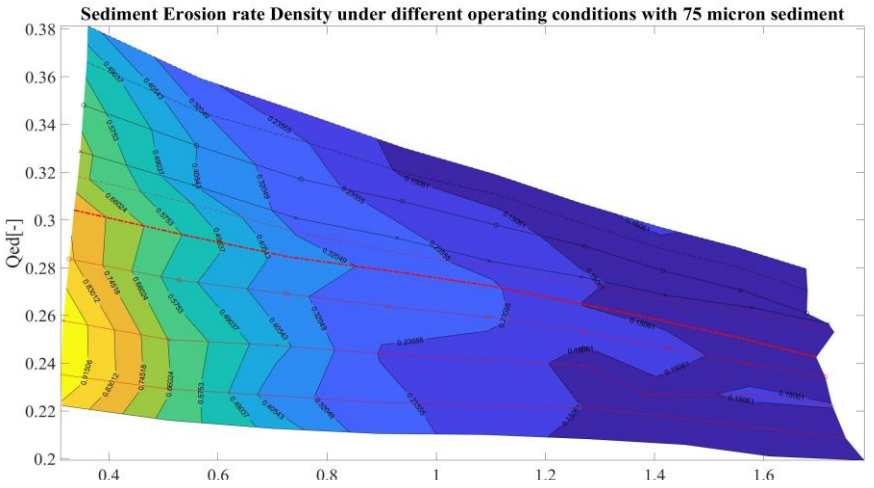

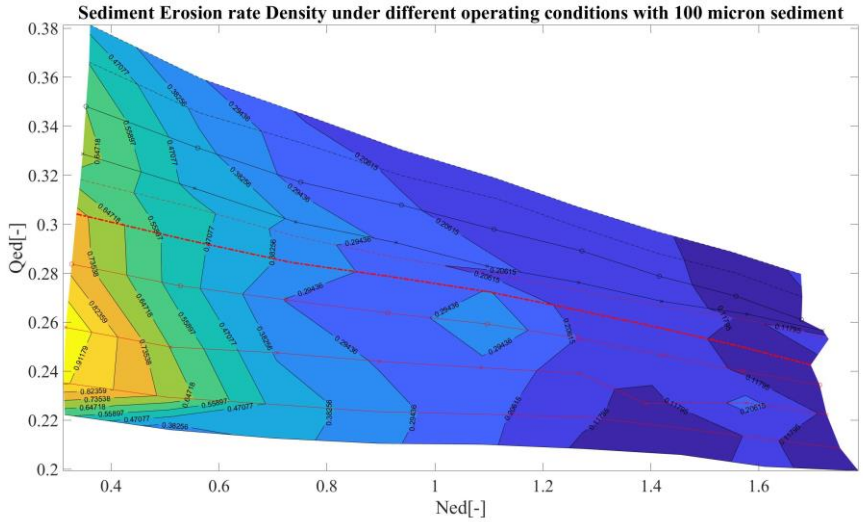

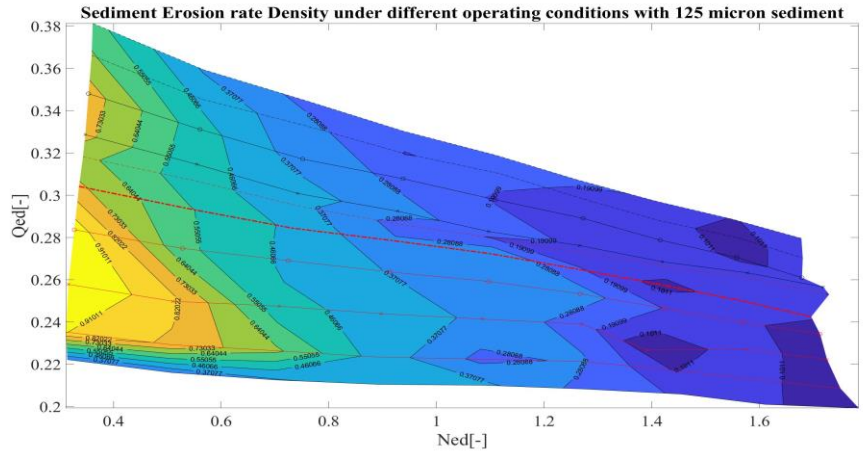

Beta Angle 36°

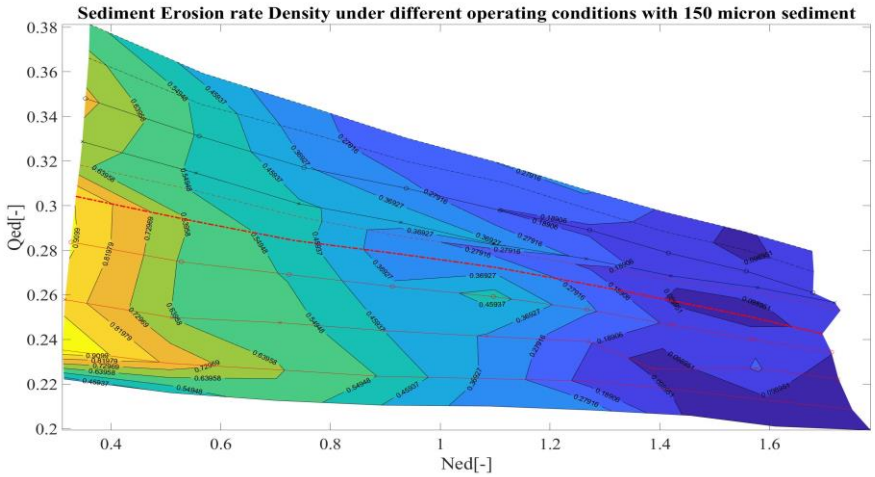

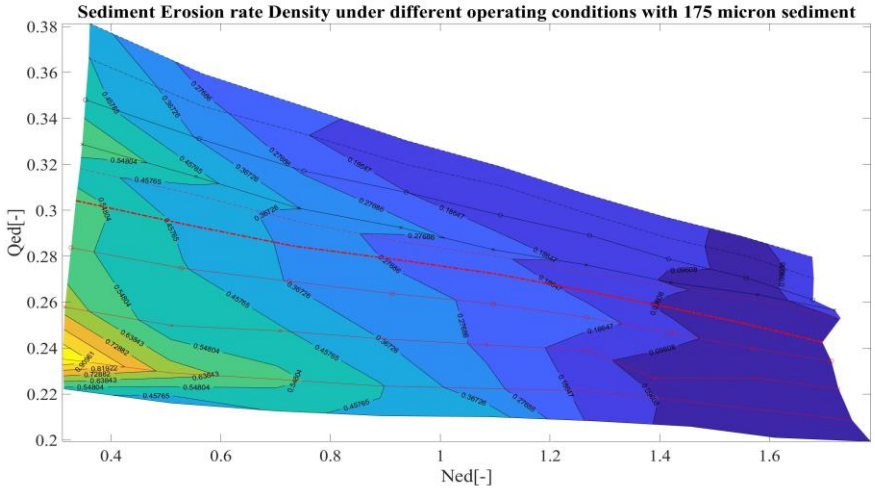

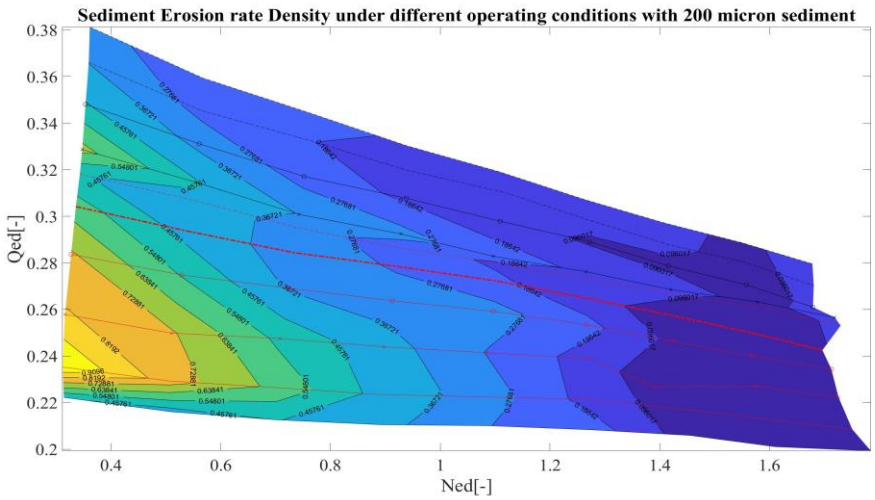

Beta Angle 36°